



THE UNIVERSITY OF QUEENSLAND  
A U S T R A L I A

# Non-equilibrium Radiation in Simulated Giant Planet Entries

Yu Liu

Bachelor of Engineering

*A thesis submitted for the degree of Doctor of Philosophy at  
The University of Queensland in 2021  
School of Mechanical & Mining Engineering*

# Abstract

A major challenge in the design of heat shields for atmospheric entry probes for Saturn, Uranus, and Neptune lies in the modeling of the thermochemical non-equilibrium shock layer. With proposed entry velocities into these H<sub>2</sub>/He atmospheres of above 20 km/s, the high temperatures in the shock layer will lead to the dissociation of H<sub>2</sub>, followed by H atom ionization, as well as associated radiation which results from internal energy excitation and the subsequent relaxation. These non-equilibrium processes can greatly affect the heating environment, as chemical reactions can alter the flow density and temperature which can influence convective heating, whereas radiation can act as another form of heating and energy loss from the flow. Despite much progress in the past, there are still significant uncertainties in numerical modeling of these non-equilibrium shock layers, especially regarding chemical reaction mechanisms. Due to the entry velocity and density being beyond the performance envelopes of most ground testing facilities, and the time and cost for a flight test being excessively high, there is a lack of data needed for a better understanding of this non-equilibrium shock layer.

The X2 facility at the University of Queensland is a super-orbital expansion tube which can enable a wide range of measurements to be conducted for planetary entry conditions. However, freestream flows can only be generated with the speeds up to 21 km/s, which is not enough to simulate Saturn, Neptune, and Jupiter entry conditions directly. In 1998, a test gas substitution was proposed to simulate the non-equilibrium shock layer during these entries with a shock speed achievable in expansion tubes. Test gases with a higher fraction of helium than in these planets' atmospheres or using neon to substitute for helium as the inert diluent of hydrogen were used to simulate the entry atmosphere. Such heavier test gases will have a lower specific heat, and thus the facility performance and energy required to recreate the appropriate post-shock temperatures will be decreased. The primary ionized content in these flow is H<sup>+</sup>, with small amounts of ionization of the third body noble gas constituents, which act primarily as chemically inert body collision partners for dissociation and ionization, and to determine the overall post-shock temperatures encountered. Thus, the test gas substitution will not greatly alter the reaction mechanisms. The use of neon at the higher enthalpies corresponding to Jupiter entries does invoke some neon ionization, which has to be considered in evaluating the experimental data. This makes it possible for impulse facilities to simulate giant planet entries within their performance envelopes. Such a substitution method has been used to generate heavily ionizing flows as described in the literature, but has never previously been experimentally validated by radiation measurements.

The purpose of this project was thus to use X2 to experimentally validate the substitution at a condition that was achievable using both helium and neon diluents and then to investigate the non-equilibrium shock phenomena that are expected during giant planet entries. Firstly, spectroscopic data were obtained by using an existing X2 condition that was designed to recreate the post-shock temperature of Saturn entry by increasing the mole fraction of helium in the H<sub>2</sub>/He test gas. The data obtained showed that a non-equilibrium shock layer with a slow ionization rate was generated. These phenomena are consistent with Saturn entry test data in the literature, thus qualitatively validating the helium enhancement substitution method. Compared to H<sub>2</sub>/He test gases, the substitution with

neon can achieve a lower specific heat of the test gas and can be used to generate hotter shock layers with the same facility performance. To validate the substitution with neon, this H<sub>2</sub>/He condition was used as a reference, and a condition with H<sub>2</sub>/Ne test gas was designed to recreate the non-equilibrium shock layer generated by the H<sub>2</sub>/He condition. The controlling factors of chemical reaction rates in H<sub>2</sub>/inert mixtures including dissociation and ionization rates of hydrogen were investigated, and an H<sub>2</sub>/Ne condition was designed by duplicating the major controlling factors in the H<sub>2</sub>/He condition. The stream-wise development of the relaxation dependent parameters gave similarity when defined in terms of an appropriate binary scaled unit. Both conditions were tested in X2 and spectroscopic data were obtained. The experimental data showed that the designed H<sub>2</sub>/Ne condition successfully recreated the non-equilibrium processes generated by the H<sub>2</sub>/He condition, and quantitative agreement was obtained in the binary scaled radiation data. This experimentally validated the substitution of using neon to substitute helium in the test gas in terms of simulating shock layer relaxation and the associated radiation.

A final series of experiments were conducted to obtain the electron number density generated by the H<sub>2</sub>/He condition based on Stark broadening. The calculated electron number density was compared with computational fluid dynamic calculations using two sets of reaction rate from the literature. Qualitative agreement was found between experimental data and numerical simulations using one of the selected rate sets. This indicates that one existing reaction kinetic model can be used to describe the shock layer chemistry well within the limits of the data that were measured. Whilst acknowledging that the full reaction mechanism is much more complex than the simple single temperature model would imply, it is seen to give a useful representation of the macroscopic phenomena at the conditions studied. Furthermore, it was found that, after adjusting one of these two rate sets by maintaining the dissociation rates and increasing the ionization rate coefficients by a factor of 25, the measured electron number density profile can be quantitatively simulated. This adjusted rate set was also cross-validated with similar measurements for Saturn entry from the literature, and good agreement was observed between experimental data and numerical predictions.

This project is the first time that the test gas substitution theory has been validated in the context of radiation measurements. Previous work studied the effects of ionization through blunt body shock standoff distances on simulated ionizing flows using this substitution. This study extended the work by means of quantitative radiation measurements, and experimentally validated the substitution by a direct comparison of radiation data in a region where the facility simulation capabilities by using H<sub>2</sub>/He and H<sub>2</sub>/Ne test gas overlap. The combined conclusions of this and the preceding work implies that giant planet shock layers can be robustly scaled and simulated in expansion tubes using the test gas substitution for both the macroscopic shock layer details and the contained radiating flow fields. The outcome of this project will lay the groundwork for future giant planet entry studies, which enables a broader range of blunt body measurements to be performed for better numerical modeling. Additionally, this project provides unique new benchmark test data and an updated reaction rate set for further numerical model improvements in simulating giant planet entry phenomena.

## **Declaration by author**

This thesis is composed of my original work, and contains no material previously published or written by another person except where due reference has been made in the text. I have clearly stated the contribution by others to jointly-authored works that I have included in my thesis.

I have clearly stated the contribution of others to my thesis as a whole, including statistical assistance, survey design, data analysis, significant technical procedures, professional editorial advice, financial support and any other original research work used or reported in my thesis. The content of my thesis is the result of work I have carried out since the commencement of my higher degree by research candidature and does not include a substantial part of work that has been submitted to qualify for the award of any other degree or diploma in any university or other tertiary institution. I have clearly stated which parts of my thesis, if any, have been submitted to qualify for another award.

I acknowledge that an electronic copy of my thesis must be lodged with the University Library and, subject to the policy and procedures of The University of Queensland, the thesis be made available for research and study in accordance with the Copyright Act 1968 unless a period of embargo has been approved by the Dean of the Graduate School.

I acknowledge that copyright of all material contained in my thesis resides with the copyright holder(s) of that material. Where appropriate I have obtained copyright permission from the copyright holder to reproduce material in this thesis and have sought permission from co-authors for any jointly authored works included in the thesis.

# Publications included in this thesis

## Incorporated as Chapter 3:

[1] **Yu Liu**, and Christopher M. James, and Richard G. Morgan, and Timothy J. McIntyre, Using Aerothermodynamic Similarity to Experimentally Study Nonequilibrium Giant Planet Entry, *Journal of Spacecraft and Rockets*, 57(5):1008-1020, 2020.

Contributor	Statement of contribution	%
<b>Yu Liu</b>	writing of text	70
	Conducted experiments	70
	numerical calculations	90
	Analysis and interpretation of data	70
Christopher M. James	writing of text	10
	Conducted experiments	30
	numerical calculations	10
	Analysis and interpretation of data	10
Richard G. Morgan	writing of text	10
	supervision, guidance	50
	Analysis and interpretation of data	10
Timothy J. McIntyre	writing of text	10
	supervision, guidance	50
	Analysis and interpretation of data	10

## Incorporated as Chapter 4:

[2] **Yu Liu**, and Christopher M. James, and Richard G. Morgan, and Timothy J. McIntyre, Experimental Validation of a Test Gas Substitution for Simulating Scaled Giant Planet Entry Conditions in Impulse Facilities, *Experiments in Fluids*, 61(9):198, 2020.

Contributor	Statement of contribution	%
<b>Yu Liu</b>	writing of text	70
	Conducted experiments	70
	numerical calculations	100
	Analysis and interpretation of data	70
	theoretical derivations	60
Christopher M. James	writing of text	10
	Conducted experiments	30
	Analysis and interpretation of data	10
Richard G. Morgan	writing of text	10
	supervision, guidance	50
	Analysis and interpretation of data	10
	theoretical derivations	40
Timothy J. McIntyre	writing of text	10
	supervision, guidance	50
	Analysis and interpretation of data	10

# Submitted manuscripts included in this thesis

## Incorporated as Chapter5:

**Yu Liu**, and Christopher M. James, and Richard G. Morgan, and Peter A. Jacobs, and Rowan Gollan, and Timothy J. McIntyre, Electron Number Density Measurements in a Saturn Entry Condition, *Submitted to AIAA Journal*.

Contributor	Statement of contribution	%
<b>Yu Liu</b>	writing of text	75
	Conducted experiments	80
	numerical calculations	70
	Analysis and interpretation of data	60
Christopher M. James	writing of text	5
	Conducted experiments	20
	Analysis and interpretation of data	10
Richard G. Morgan	writing of text	5
	supervision, guidance	50
	Analysis and interpretation of data	10
Peter A. Jacobs	writing of text	5
	numerical calculations	15
	Analysis and interpretation of data	5
Rowan Gollan	writing of text	5
	numerical calculations	15
	Analysis and interpretation of data	5
Timothy J. McIntyre	writing of text	5
	supervision, guidance	50
	Analysis and interpretation of data	10

# Other publications during candidature

## Journal Articles

1. [3] Daniel R. Smith, and David E. Gildfind, and Peter A. Jacobs, and Timothy G. Cullen, and Christopher M. James, and **Yu Liu**, and Rowan Gollan, and Timothy J. McIntyre, Magnetohydrodynamic Drag Measurements in an Expansion Tunnel with Argon Test Gas, *AIAA Journal*, 58(10):4495-4504, 2020.
2. [4] Christopher M. James, and Steven W. Lewis, and Richard G. Morgan, and **Yu Liu**, and Alexis Lefevre, Generating High Speed Earth Re-entry Test Conditions in an Expansion Tube, *Journal of Spacecraft and Rockets*, 0(0):1-18, 2020, Article in Advance.

## Conference Papers

1. [5] **Yu Liu**, and Christopher M. James, and Richard G. Morgan, and Peter A. Jacobs, and Rowan Gollan, and Timothy J. McIntyre, Electron Number Density Measurements in a Saturn Entry Condition, *AIAA Scitech 2021 Forum*, 11-15 & 19-21 January 2021, VIRTUAL EVENT.
2. [6] **Yu Liu**, and Pierpaolo Toniato, and Christopher M. James, and Richard G. Morgan, and Timothy J. McIntyre, Multidimensional Effects and Self-absorption on Spectroscopic Observations of Saturn Entry Radiation, *Asia Pacific International Symposium on Aerospace Technology*, 4-6 December 2019, Gold Coast, Queensland.
3. [7] **Yu Liu**, and Richard G. Morgan, and Christopher M. James, and Timothy J. McIntyre, Theoretical and Experimental Study of Helium-Neon Substitution for Saturn Entry Radiation, *AIAA Aviation 2019 Forum*, 17-21 June 2019, Dallas, Texas.
4. [8] **Yu Liu**, and Christopher M. James, and Richard G. Morgan, and Timothy J. McIntyre, Experimental Study of Saturn Entry Radiation with Higher Amount of Diluent in an Expansion Tube, *2018 Joint Thermophysics and Heat Transfer Conference*, 25-29 June 2018, Atlanta, Georgia.
5. [9] Christopher M. James, and **Yu Liu**, and Richard G. Morgan, Simulating Uranus Entry in an Expansion Tube, *AIAA AVIATION 2020 FORUM*, 15-19 June, 2020, VIRTUAL EVENT.
6. [10] Christopher M. James, and Steven W. Lewis, and David E. Gildfind, and Richard G. Morgan, and Timothy J. McIntyre, and **Yu Liu**, Generating High Speed Earth Re-entry Test Conditions in an Expansion Tube for Interplanetary Return Missions, *32nd International Symposium on Shock Waves*, 14-19 July 2019, Singapore.
7. [11] Christopher M. James, and Byrenn Birch, and Daniel R. Smith, and Timothy G. Cullen, and Theodore Millard, and Samuel Vella, and **Yu Liu**, and Richard G. Morgan, and Nathan Stern, and David Buttsworth, Testing of Ultra Fast Response, Durable Co-axial Thermocouples for High Enthalpy Impulse Facilities, *AIAA Aviation 2019 Forum*, 17-21 June 2019, Dallas, Texas.

## Contributions by others to the thesis

The emission spectroscopy data was calibrated using the code kindly provided by Dr. Steven Lewis. The code for Abel inversion in Chapter 3 was modified from an original version found in the Group drive. (which is believed to be provided by the University of Stuttgart) .

## **Statement of parts of the thesis submitted to qualify for the award of another degree**

No works submitted towards another degree have been included in this thesis.

## **Research involving human or animal subjects**

No animal or human subjects were involved in this research.

## Acknowledgements

It was found by researchers that people can have different personalities in different languages. The four-years PhD experience at UQ shaped my personality on the English side. During this journey, many amazing people supported and helped me to accomplish this project, and most importantly, shaped me to be who I am.

Richard Morgan: for offering me the opportunity to join this wonderful group and to start this project. You have had the greatest impact on my life. I am grateful to your trust, encouragement, and all the shining ideas during your supervision. Thanks for providing enough freedom to me to explore different avenues while always being supportive and available for a question. I am very lucky to sit next to you for the past three years – you showed me what a good researcher and a decent person is like.

Timothy McIntyre: for bringing me into the world of spectroscopy. Thanks for always being enthusiastic to read my papers and giving enlightening comments, also for questioning me whenever I made conclusions too hastily. You taught me how to think and write like a scientist, although I might be still an engineer to you. The weekly meeting with you is also very appreciated – it ensures I am still on the right track.

Chris James: I would prefer to call you a sponsor instead of a mentor. Thank you for always believing in me and supporting me. I very appreciate all the insightful discussions with you. The help in the use of the analysis code collections and new instrumentations is also appreciated. It is an honor to have a friend after debating with him on almost everything – it really improved my English. Last but not least, thank you for encouraging me to be tough and for being the first target.

All X-lab fellows: for all the moments working hard together and make the expansion tube to work. None of the experiments can take place without the help of my colleagues in X-lab. A big thanks must be given to Neil Duncan for the model manufacturing, Barry Allsop for the help in the use of thermocouple, and all the operators in X2 (Ranjith Ravichandran, Rory Kelly, Tim Cullen, Daniel Smith, Nils Temme, Ranjini Ramesh, Matt Thompson, Alexis Lefevre, and Steven Apirana) for keeping the facility running well. Also, thanks to Steven Lewis for teaching me to use spectral analysis code and NEQAIR, Pierpaolo for showing me how to massage the setting when the simulation did not want to work, Andreas for solving my SolidEdge problems, and Sam for the sweets. A special thanks to Han Wei for helping me settle down in Brisbane.

Dr. Peter Jacobs and Dr. Rowan Gollan: for your generous help in solving all the CFD problems and for trusting me to implement the giant planet models. None of the numerical work in this thesis can be done without your help. I hope my CFD skill is getting better.

Also, I would like to acknowledge the assistance from many other researchers from centre for hypersonics. I am very lucky to work with these smart people, and I feel like the acknowledgment part is not enough for me to list all the help and inspiration received from these wonderful people. The accomplishment of this project and this thesis cannot be possible without you.

My family and friends: for always believing that I can achieve everything while accepting that I am

just a normal person. A special thanks to my parents for supporting and encouraging me to explore the world even I am their only child. To Ying for your care, concern, and dry fruits! Thanks for backing me up and giving me the wisest advices. I wish I can be as wise and brave as you one day. To Qinxue for accompanying and inspiring me through this journey. You are the one who can always make me calm and rational. I hope we can all become the person we aspire to be and eventually live in the same city. To Jiawei for making everything possible and bringing support and encouragement to my everyday life. You give me the courage to pursue my dream, and I can not wait to embrace the world with you. To all the friends in Brisbane to share this journey with me. This is the golden time of our lives. All the joys and tears we shared together will be kept on the bottom of my heart and never fade.

## **Financial support**

No financial support was provided to fund this research.

## **Keywords**

hypersonics, ground testing, expansion tube, non-equilibrium, radiation, aerothermodynamics, giant planet entry

## **Australian and New Zealand Standard Research Classifications (ANZSRC)**

ANZSRC code: 020503 Non-linear Optics and Spectroscopy 25%

ANZSRC code: 090107 Hypersonic Propulsion and Hypersonic Aerodynamics 75%

## **Fields of Research (FoR) Classification**

FoR code: 0901, Aerospace Engineering, 75%

FoR code: 0205, Optical Physics, 25%



---

# Contents

---

Abstract . . . . .	ii
<b>Contents</b>	xiii
<b>List of figures</b>	xvi
<b>List of tables</b>	xix
<b>List of abbreviations and symbols</b>	xxi
<b>1 Introduction</b>	1
1.1 Missions to Giant Planets . . . . .	1
1.2 Aeroheating during Giant Planet Entries . . . . .	2
1.3 Objectives . . . . .	5
1.4 Thesis Structure . . . . .	6
<b>2 Literature Review</b>	9
2.1 Non-equilibrium Flow . . . . .	9
2.1.1 Dissociation . . . . .	11
2.1.2 Ionization . . . . .	12
2.2 Modeling for Non-equilibrium Giant Planet Entry Conditions . . . . .	13
2.3 Test Gas Substitution in an Impulse Facility . . . . .	19
2.4 Summary . . . . .	23
<b>3 Experimental Validation of Helium Enhancement Substitution</b>	25
3.1 Introduction . . . . .	26
3.2 Facility and Test Condition . . . . .	28
3.2.1 X2 Expansion Tube and Test Condition . . . . .	28
3.2.2 Numerical Comparisons . . . . .	30
3.2.3 Optical Measurements and Test Model . . . . .	32
3.3 Condition Characterization Experiments . . . . .	34
3.4 Blunt Body Experiments . . . . .	36
3.4.1 High Speed Images . . . . .	36

3.4.2	Spectroscopic Results . . . . .	38
3.4.3	Contamination . . . . .	42
3.5	Abel Inversion of Experimental Data . . . . .	45
3.5.1	Effect of Aluminium Contamination on Radial Distributed Radiation . . . . .	47
3.6	Conclusions . . . . .	48
<b>4</b>	<b>Experimental Validation of Helium-neon Substitution</b>	<b>51</b>
4.1	Introduction . . . . .	52
4.2	Test Gas Modeling . . . . .	54
4.3	Condition Design and Numerical Validation . . . . .	56
4.4	Experimental Results . . . . .	58
4.4.1	Facility . . . . .	58
4.4.2	Test Model and Instrumentation . . . . .	59
4.4.3	Spectroscopic Data . . . . .	61
4.4.4	High Speed Imaging . . . . .	68
4.5	Conclusions . . . . .	70
<b>5</b>	<b>Electron Number Density Measurements</b>	<b>73</b>
5.1	Introduction . . . . .	74
5.2	New Experimental Measurements in X2 . . . . .	76
5.2.1	Test Models and Optical Configuration . . . . .	77
5.2.2	Flow Condition . . . . .	78
5.2.3	Self-absorption Investigation . . . . .	80
5.2.4	Electron Number Density Calculation . . . . .	83
5.3	Computational Fluid Dynamics Modeling and Comparison . . . . .	88
5.4	Conclusion . . . . .	93
<b>6</b>	<b>Conclusion</b>	<b>95</b>
6.1	Major Findings . . . . .	95
6.2	Future Work . . . . .	96
<b>Bibliography</b>		<b>99</b>
<b>A</b>	<b>Modifications to Reproduced Publications</b>	<b>109</b>
A.1	Chapter3: Using Aerothermodynamic Similarity to Experimentally Study Non-equilibrium Gas Giant Entry . . . . .	109
A.2	Chapter4: Experimental Validation of a Test Gas Substitution for Simulating Scaled Giant Planet Entry Conditions in Impulse Facilities . . . . .	110
<b>B</b>	<b>Characterisation Experiments for the H<sub>2</sub>/Ne Condition</b>	<b>113</b>
B.1	Condition Design Requirements . . . . .	113

B.2	Experimental Set-up . . . . .	114
B.3	Results . . . . .	114
B.3.1	Time-resolved Pressure and Emission Measurements . . . . .	114
B.3.2	Condition Detail . . . . .	118
<b>C</b>	<b>Technical Drawings for Test Models and Alignment Tools</b>	<b>119</b>
C.1	Spherical Test Model . . . . .	120
C.2	Cylindrical Test Model: 33.3 diameter, 100 mm long . . . . .	121
C.3	Alignment Tool for Cylindrical Test Models . . . . .	122

---

# List of figures

---

1.1	Non-equilibrium shock layer during blunt body giant planet entry.(Adapted from Jacobs [12])	3
1.2	Ablation of heat shield of Galileo probe during entry into Jupiter (Adapted from NASA Ames photo ACD96-0313-13)	3
2.1	Temperature behind a normal shock wave as a function of freestream velocity at a standard altitude of 52 km. (Anderson, 2003) [13]	10
2.2	Comparisons between relaxation downstream of oblique shock measured in Stalker's experiments and predicted using ionization rates from Leibowitz [14] (rate set A) and Leibowitz and Kuo [15] (rate set B). (Stalker, 1979) [16]	14
2.3	Locations of 10 ablation sensors ( $A_1-A_{10}$ ) in heat shield and four resistance thermometers ( $T_1-T_4$ ) inside structure; sensors are not coplanar. (Milos et al., 1999) [17]	15
2.4	Comparison of final shape with pre-flight predictions. (Milos, 1997) [18]	16
2.5	Comparison of obtained final forebody recession profile in Matsuyama's work with flight data and preflight prediction. (Matsuyama, 2005) [19]	17
2.6	Comparison of UV range radiance between EAST measurements (shot 17) [20] and DSMC/NEQAIR prediction [21]. (Higdon et al., 2018) [21]	19
2.7	Ionizing relaxation: effect of diluent type and concentration. (Stalker and Edwards, 1998) [22]	21
2.8	Ionizing relaxation: effect of temperature and pressure. (Stalker and Edwards, 1998) [22]	21
2.9	Effects of helium or neon fraction on post-shock temperature. (James et al., 2018) [23]	23
3.1	Schematic representation of X2. (James et al., 2018) [24]	29
3.2	Post-shock temperature profiles generated by X2 condition and at the proposed Saturn entry trajectory point.	31
3.3	Post-shock H and $H_2$ mole fraction profiles generated by X2 condition and at the proposed Saturn entry trajectory point.	32
3.4	Post-shock electron mole fraction profiles generated by X2 condition and at the proposed Saturn entry trajectory point.	32
3.5	A schematic of the test model. Axial and radial object plane locations, and their overlap point are also shown.	33

3.6	Schematic of the optical arrangement for axial and radial experiments (not to scale) . . . . .	34
3.7	H- $\alpha$ filtered radiation from shock layer over pitot probes, labels show the actual probe heights relative to the centerline. . . . .	35
3.8	Time-resolved pitot pressure and integrated emission over each pitot probe (pt4 data not shown due to connection failure). . . . .	36
3.9	Radiative shock layers filtered by a H-alpha narrow bandpass filter in the test time, with different camera focal lengths chosen. . . . .	37
3.10	Time-resolved shock standoff distances with the uncertainty. . . . .	37
3.11	Regions chosen in H- $\alpha$ filtered radiative field and the time-resolved spatially integrated intensities in these regions. . . . .	38
3.12	Spectra from axial experiments, (a): with coarse (150 gpmm) grating, (b): with fine (600 gpmm) grating. . . . .	39
3.13	H- $\alpha$ and H- $\beta$ radiance profiles from axial experiments. . . . .	40
3.14	Linewidths of H- $\alpha$ along the axial plane for the experiment with the fine grating. . . . .	41
3.15	Spectrum data from the radial experiment (with fine (600 gpmm) grating). . . . .	42
3.16	H- $\alpha$ radiance profile from the radial experiment, along the radial plane 3.2 mm upstream of the model edge. . . . .	43
3.17	Comparison of H- $\alpha$ spectral lines at the overlap point (3.2 mm upstream of the model edge) from axial and radial experiments. . . . .	44
3.18	Radiance profiles of Al <sup>+</sup> and H- $\alpha$ lines from axial experiments, with Al <sup>+</sup> radiance profiles being scaled by 10. . . . .	44
3.19	(a): Measured H- $\alpha$ and Al <sup>+</sup> radiance profiles, (b): Abel inverted results, from the radial experiment. . . . .	46
3.20	Linewidths for Abel inverted spectral radiances of H- $\alpha$ along the radial direction for the radial experiment. . . . .	47
3.21	(a): Measured H- $\alpha$ and Al <sup>+</sup> radiance profiles. (b): Abel inverted results from radial experiments and its repeat. . . . .	48
4.1	Selected flow properties predicted along the $(1 - r)\chi$ coordinate in the target helium condition, designed neon condition, and Saturn entry trajectory point [25] from Poshax. .	59
4.2	Schematic of a typical arrangement of the high speed imaging system and optical emission spectroscopy system for stagnation region radiation studies (not to scale). . . . .	60
4.3	Example calibrated spectral data from the experiments with the helium and the neon condition. . . . .	62
4.4	Sample spectra behind the shock from the helium condition and the neon condition. . . .	63
4.5	Integrated radiance along the stagnation streamline. . . . .	64
4.6	Scaled radiance along the scaled stream-wise axis in helium and neon condition. Radiance for helium and neon condition was scaled by $P_f$ . . . . .	65

4.7	Radiance profiles along stagnation streamline using different radii models for the helium condition. . . . .	67
4.8	H- $\alpha$ filtered high speed images in the test time. . . . .	69
4.9	H- $\beta$ filtered high speed images in the test time. . . . .	69
5.1	Line-of-sight through shock layer and the 2D projected plane of cylindrical model (ignoring circle of confusion). . . . .	77
5.2	Schematic of the optical arrangement with the spectrometer looking along the axis of the model (not to scale). . . . .	78
5.3	Two orientations of the measurements on the model. . . . .	79
5.4	High speed imaging in the test time for the experiments with aspect ratios of 3, 4 and 5, with the camera looking perpendicular to the axis of the cylinder. . . . .	81
5.5	(a) Canny edge detected shock shape. (b) Optical path lengths normalized by the model length. . . . .	81
5.6	An example of calibrated spectral data. Flow from top to bottom, and the estimated shock location is marked as 0. . . . .	82
5.7	Integrated radiance profiles along the stagnation streamline normalized by model lengths. . . . .	82
5.8	Fitted Lorentzian profile for the data measured at 1.49 mm behind the shock. . . . .	85
5.9	Lorentzian fitted FWHM profile along the stagnation streamline. . . . .	85
5.10	Comparison among various broadening effects for H- $\beta$ line broadening. . . . .	86
5.11	Electron number density profile along the stagnation streamline. . . . .	87
5.12	An example of a grid convergence study. . . . .	89
5.13	Electron number density comparison among experimental results and CFD predictions using two sets of rates. . . . .	89
5.14	Species mole fractions predicted by using L&K's rates and the adjusted rates. . . . .	90
5.15	Comparison between EAST data and Eilmer simulation results in 0.1 torr conditions. . . . .	91
5.16	Comparison between EAST data and Eilmer simulation results in 0.2 torr conditions. . . . .	92
5.17	Comparison between EAST data and Eilmer simulation results in 0.5 torr conditions. . . . .	92
6.1	Comparison between estimated shock layer radiation viewing normal to the shock and blackbody radiation at 2500 K and 2800 K. . . . .	98
B.1	Flowchart of the neon condition design procedure. . . . .	115
B.2	Set-up of pitot probes on the rake . . . . .	116
B.3	Scale of the rake with the nozzle and its axial location. . . . .	116
B.4	H- $\alpha$ filtered radiation from shock layer over pitot probes and the area for intensity integration, with pt5 aligned with the nozzle centreline. . . . .	117
B.5	Time-resolved pitot pressure and integrated emission over each pitot probe. . . . .	117

---

# List of tables

---

3.1	Detailed information of the test condition. . . . .	29
3.2	Freestream and post-shock conditions predicted by PITOT and the values measured and calculated in experiments. . . . .	30
3.3	Spectroscopic setting in each experiment. . . . .	38
4.1	Details of the test conditions. . . . .	57
4.2	Grating settings and the measured shock speeds for each experiment. . . . .	61
5.1	Details of the test condition. . . . .	79
5.2	Details of flow properties. . . . .	80
5.3	Adjusted forward reaction rates for H <sub>2</sub> /He mixtures. . . . .	90
B.1	Details of the designed H <sub>2</sub> /Ne condition. . . . .	118
B.2	Comparison between PITOT prediction and experimental measurements. . . . .	118



---

# List of abbreviations and symbols

---

---

## Abbreviations

---

TPS	Thermal protection system
ARAD	Analog resistance ablation detector
EAST	Electric arc shock tube
UQ	University of Queensland
CFD	Computational fluid dynamics
ANAA	Annular arc accelerator
VUV	Vacuum ultraviolet
UV	Ultraviolet
NIR	Near-infrared
DSMC	Direct simulation Monte Carlo
OES	Optical emission spectroscopy
FWHM	Full width at half maximum
CEA	Chemical Equilibrium with Applications
CCD	Charge-coupled device
3D	Three-dimensional
2D	Two-dimensional
CV	Coefficient of variation
VdW	Van der Waals

---

---

## Symbols

---

$\gamma$	Specific heat ratio
$C_p$	Constant pressure specific heat, $\text{J}\cdot\text{kg}^{-1}\cdot\text{K}^{-1}$
$C_v$	Constant volume specific heat, $\text{J}\cdot\text{kg}^{-1}\cdot\text{K}^{-1}$
$K_{fd}$	Forward dissociation rate coefficient, $\text{m}^3\cdot\text{s}^{-1}\cdot\text{mol}^{-1}$
$K_{rd}$	Backward dissociation rate coefficient, $\text{m}^6\cdot\text{s}^{-1}\cdot\text{mol}^{-2}$
$[M]$	Molar concentration of species M, $\text{mol}/\text{m}^3$
$k$	Boltzmann constant, $8.62\times 10^5 \text{ eV}\cdot\text{K}^{-1}$
$E_a$	Threshold energy for reaction, eV

$K_p$	Equilibrium constant,
$\chi$	Binary scaling variable, $\int \frac{P}{V} dx$ , Pa· s
$r$	Mole fraction of H <sub>2</sub>
$P$	Pressure, Pa
$V$	Velocity, m/s
$s$	Stream-wise distance, m
$f$	Full width at half maximum, nm
$\lambda_0$	Centre wavelength, nm
$T$	Temperature, K
$M$	Molecular weight, kg·mol <sup>-1</sup>
$\alpha$	Mole fraction of dissociated H <sub>2</sub>
$K_{fi}$	Forward ionization rate coefficient, m <sup>3</sup> ·s <sup>-1</sup> · mol <sup>-1</sup>
$\beta$	Mole fraction of ionized H
$A$	Absorbency
$c$	Molar concentration of the attenuating species, mol/m <sup>3</sup>
$\varepsilon$	Molar absorption coefficient, m <sup>2</sup> ·mol <sup>-1</sup>
$l$	Path length, m
$N_e$	Electron number density, m <sup>-3</sup>
$\lambda$	Mean free path, m
$N_A$	Avogadro's number, $6.022 \times 10^{23}$
$\rho$	Density, kg/m <sup>3</sup>
$D$	Hard sphere particle diameter, m

---

Subscript

---

$Tra$	Translational state
$f$	Post-shock frozen state
$i$	Initial ionizing (fully dissociated) state
$e$	Electronic state
$V$	Voigt profile
$L$	Lorentzian profile
$G$	Gaussian profile
$eq$	Equilibrium state

---

# Chapter 1

---

## Introduction

---

Giant planets – Jupiter, Saturn, Uranus, and Neptune, are the four outermost planets in our solar system. These giant planets are composed mainly of hydrogen and helium, with a small amount of other trace elements such as methane. These four planets take up over 99% of the planetary mass and total angular momentum of the solar system outside of the sun and also contain the major mass of the gaseous nebula that evolved into the solar system. Thus, “the giant planet story is the story of the solar system” [26].

### 1.1 Missions to Giant Planets

Missions to the giant planets were identified as priorities for future planetary exploration since 2012 with three overarching goals [26].

1. The research and observations of the exoplanets indicate that giant planets, especially ice giants like Neptune and Uranus, are very common beyond the solar system [27, 28]. These giant planets are either mainly composed of helium and hydrogen, or retain a deep hydrogen/helium core derived from the sun’s early nebulae. Knowledge of the giant planets in our solar system will enhance the study of exoplanets through high resolution observations or in situ measurements by planetary probes.

2. The Sun in our solar system has a magnetic field that varies in time and location across the surface of the Sun. The release of the stored magnetic energy in the Sun’s atmosphere causes solar storms, which not only lead to natural aurora spectacles, but also have an impact on human activities such as destabilizing power grid’s operation and disrupting spacecraft hardware. Earth is not the only planet in our solar system that is significantly affected by solar storms. Aurora was also observed on the four giant planets and Jupiter’s moon Ganymede. Thus, studying the aurora occurring in giant planets will help understand how solar storms propagate in the solar system, and how these processes play out on earth.

3. The dynamic atmospheric processes of giant planets are simpler than those of earth, as they can be understood without considering the interaction with the lithosphere, cryosphere, hydrosphere, or biosphere. For this reason, giant planets can serve as an ideal laboratory to investigate fundamental

physical processes such as the limitations of Kepler's laws, and to help understand the evolution of atmospheric processes such as a jet stream.

To answer all these questions, simply observing these giant planets on earth is not enough, and in situ measurements during space missions are required. Galileo was the first probe that conducted atmospheric entry into these planets. This entry provided us with critical data about Jupiter such as its internal temperature profile, gas composition, and deep wind. Then, the following Cassini-Huygens mission filled the gap in understanding the structure of Saturn system, and enabled us to have a close look at Saturn's ring. This mission also laid the groundwork for future Saturn atmospheric probes. Apart from these missions, Juno probe, which successfully entered the orbit of Jupiter in July 2016, is the second probe to orbiter Jupiter. Since then, it has been collecting data on this gas giant's interior [29]. Before deorbiting into Jupiter in July 2021, it will study Jupiters deep interior structure, abundance, distribution of water, and polar magnetic environment [26]. However, the knowledge of Saturn, Uranus, and Neptune, especially for the ice giants (Uranus and Neptune) which are believed to have oceans beneath their atmospheres, is still insufficient. Thus, further explorations for these planets are considered as high priorities [30]. Due to the long lead times and high costs of such missions, there is great value laid in laboratory studies of the associated hypervelocity atmospheric entries.

## 1.2 Aeroheating during Giant Planet Entries

The multiple proposed entry trajectories for giant planets encompass a range of entry velocities and create various heating environments for the thermal protection system (TPS). The entry speed for Jupiter and the proposed entry velocities for Saturn, Uranus and Neptune are around 47 km/s, 26 km/s, 22 km/s, and 29 km/s respectively [18, 25, 31, 32]. These entry speeds will lead to immediate post-shock temperatures of over 20000 K. In this high temperature environment, there will be hydrogen dissociation occurring behind the shock, followed by H atom ionization which is initiated by heavy particle collisions and then accelerated by H-e<sup>-</sup> collisions when the electron number density is sufficient. These chemical relaxation processes are generally associated with emitted radiation due to internal energy excitations. Such a non-equilibrium shock layer and the relaxation processes are shown in Fig. 1.1. Chemical reactions can greatly influence macroscopic flow properties such as density and temperature, thus affecting convective heating, whereas the radiation can be another major heating source. Hence, knowledge of these non-equilibrium processes is essential for the design of heat shields which are used to protect the entry probes from the harsh heating environment.

Jupiter entry was performed by the Galileo probe in 1995, with the entry velocity relative to its atmosphere of 47.5 km/s [33]. The mission to Jupiter has the highest entry velocity among those for giant planets, and the Galileo probe experienced the highest heat load ever recorded. In this harsh heating environment, the hydrogen dissociation processes finished almost immediately after the shock, before ionization was fully initiated. Radiation was the major heating source for the thermal protection system and contributed up to 99% of the total heat load during the entry [33]. The heat shield of the Galileo probe accounted for nearly 50% of the spacecraft mass, but only 50% of the heat

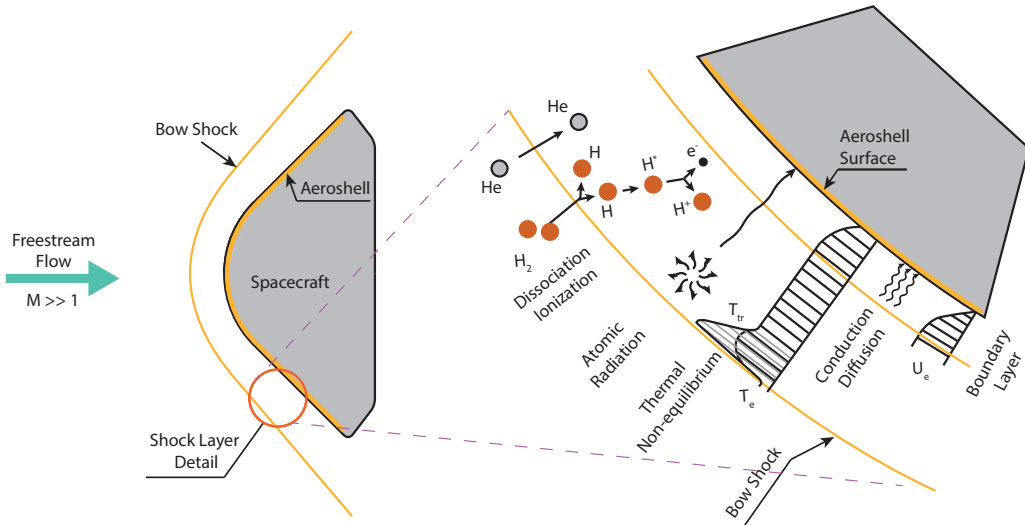


Figure 1.1: Non-equilibrium shock layer during blunt body giant planet entry.(Adapted from Jacobs [12])

shield ablated during the entry [18] (shown in Fig.1.2). This is because a conservative design with a factor of safety of 2 was employed over prediction of the final heat shield thickness. Comparing the recession recorded by the analog resistance ablation detector (ARAD) sensors on the heat shield to the pre-flight prediction [34], it can be found that the numerical prediction over-estimated the ablation on the stagnation region, while the ablation on the frustum region was under-estimated [17, 18].

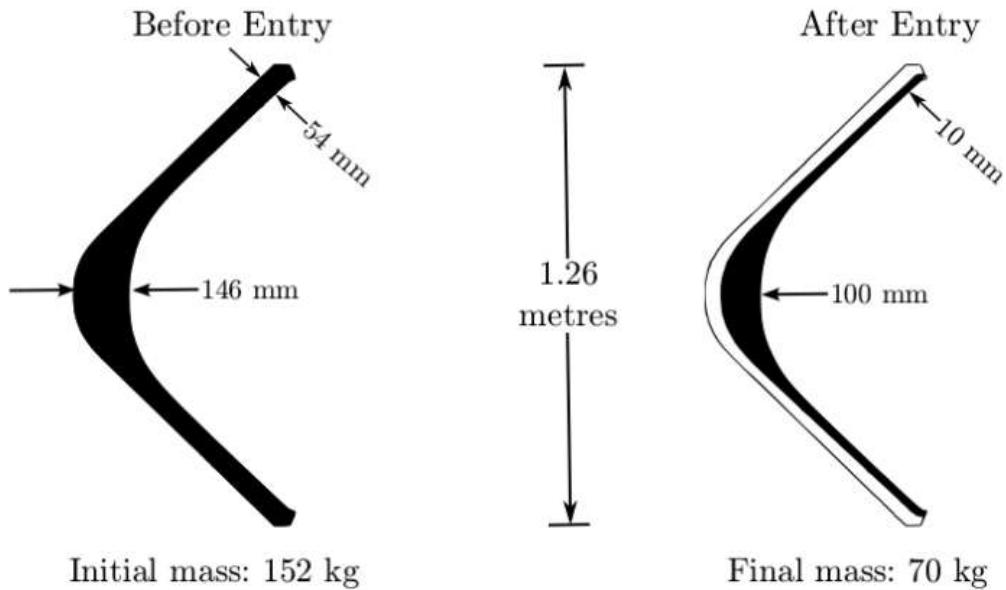


Figure 1.2: Ablation of heat shield of Galileo probe during entry into Jupiter (Adapted from NASA Ames photo ACD96-0313-13)

The data collected in the Galileo mission allowed further development on the numerical modeling [19, 35–38]. It is worth noting that the work of Erb et al. [38] provides the most accurate recession prediction for the Galileo probe TPS material to date, with some improvements in the modeling based on the advances made in the past studies. However, as the time and cost of flight tests are excessively high, and the entry condition is beyond most of the ground testing facilities, these improved models

were validated mainly against macroscopic measurements such as recession data from the Galileo mission. Hence, more ground testing data such as spectroscopic data or wall heat flux data are required to further validate these numerical models for a more confident heating prediction.

For proposed Saturn and Uranus entry trajectories, aeroheating in the shock layer was simulated by Palmer et al. [25] using NASA's simulation tool DPLR. It was found that the shock layers in both entry conditions are in highly thermochemical non-equilibrium states. For the conditions where both convective heating and radiative heating are dominant, the uncertainty in predicting the radiative heating is significantly larger than that in convective heating. The uncertainty in the prediction of convective heating was mainly driven by the transport properties and hydrogen recombination near the wall, while thermochemical non-equilibrium processes including translational-vibrational relaxation and chemical reactions are the main uncertainty sources for radiative heating prediction. Thus, for a better prediction of the radiative heating during these entries, improvements in modeling the thermochemical non-equilibrium processes are required.

There are several reaction schemes to describe the chemical reactions for H<sub>2</sub>/He mixtures in the literature [14, 15, 39, 40], while the reaction schemes from the shock tube tests by Leibowitz [14] and Leibowitz and Kuo [15] are most commonly used [16, 21] for H<sub>2</sub>/He mixtures. These rates have been experimentally validated by Stalker [16]. He found that the rates from Leibowitz and Kuo [15] had a better agreement with the experimental measurements. However, these two rate sets may have issues due to the driver gas radiation [40].

Due to the performance limitations for most ground testing facilities, there is little relaxation data available for these conditions. Radiation measurements at Saturn and Uranus entry conditions were studied in NASA's Electric Arc Shock Tube (EAST), which is able to recreate the proposed entry densities and velocities [20]. It was found that for Uranus entry conditions, the radiation signal was lower than background noise and thus could not be accurately measured, while the Saturn entry tests exhibited a highly non-equilibrium radiating shock layer with a delayed ionization, and the flow is in a non-Boltzmann state. These phenomena are consistent with the numerical result shown in the work of Palmer et al. [25]. The electron number density and temperature measurements from the work of Cruden et al. [20] were also used to validate a state-to-state chemical kinetics of the H<sub>2</sub>/He mixture proposed by Colonna et al. [41]. This shows an alternative path to ionization which leads to higher values of the electron density may exist in these conditions.

However, due to its short shock test time, EAST is not designed for experiments with test models as it cannot establish a steady flow for such conditions. An expansion tube such as X2 at the University of Queensland (UQ) [42] can establish test flow on a model for up to 300  $\mu$ s, so that it is possible to conduct a wider range of test model associated measurements. However, test flows with velocities of only up to 21 km/s can be generated, which is around the entry velocity of Uranus [9]. For faster entries, such as for Saturn, Jupiter, and Neptune, it is not possible to directly recreate suitable entry conditions in X2.

To simulate the non-equilibrium shock layers during giant planet entries in ground testing facilities, apart from directly recreating the entry speeds and densities, one option is to only simulate the

post-shock flow condition. In 1998, a substitution using a heavier test gas than in the actual H<sub>2</sub>/He atmosphere was proposed [22]. Specifically, a higher fraction of helium or using neon instead of helium as the third body collision partner could be used. By using this substitution, the specific heat of the test gas would be lower than in the atmosphere, so that a lower shock speed would be required to recreate the post-shock temperature experienced during giant planet entries. As in the entry conditions of Saturn, Uranus, and Neptune, helium and neon mainly act as third body collision partners, the test gas substitution will not greatly change the reaction mechanism. This substitution makes it possible for ground testing facilities like X2 to recreate the post-shock temperature of the proposed giant planet entries within their performance envelopes. The detail of the substitution theory and its application will be discussed in section 2.3.

This substitution has been analytically demonstrated and used to generate ionizing flows in prior works [16, 43–45], but has never been experimentally validated and used to simulate the radiating non-equilibrium shock layers in giant planet entries. In previous work, James et al. [23] investigated the feasibility of using the substitution to recreate post-shock temperatures for Saturn and Uranus entry in X2, and a condition targeting a Saturn entry trajectory point [25] was designed with a higher mole fraction of helium (80%) than in the actual atmosphere ( $\approx 15\%$ ). This condition is able to duplicate the post-shock frozen temperature in the selected entry condition with an achievable shock speed in X2. However, it has not previously been experimentally validated whether it can generate a representative radiating non-equilibrium shock layer during the proposed Saturn entry.

## 1.3 Objectives

The purpose of this project is to employ a test gas substitution method in the UQ’s X2 expansion tube to study the non-equilibrium phenomena and the associated radiation during the entries into selected giant planets. The specific objectives to accomplish this goal are:

**1. Generate shock layer radiation data representative of Saturn entry by using an enhanced fraction of helium in the test gas in X2:** Obtain calibrated emission spectroscopy data to study the non-equilibrium shock layer generated by the existing H<sub>2</sub>/He condition. The enhanced helium substitution needs to be experimentally validated by comparing the obtained radiation data with previous EAST Saturn entry experiments. After that, this H<sub>2</sub>/He condition can be used as the reference to design a H<sub>2</sub>/Ne condition for the helium-neon substitution validation.

**2. Investigate the controlling factors for the chemical reaction rates in the hydrogen/inert gas mixtures:** Chemical reaction rates including dissociation and ionization rates are used to evaluate the similarity of the non-equilibrium processes. The factors that control these relaxation rates in the hydrogen/inert gas mixtures need to be identified for the subsequent H<sub>2</sub>/Ne condition design. The effects that these controlling factors have on the relaxation rates need to be understood to interpret the relaxation data and perform a quantitative comparison between the two conditions.

**3. Experimentally validate the test gas substitution by using H<sub>2</sub>/Ne instead of H<sub>2</sub>/He to simulate the non-equilibrium processes:** An X2 condition using H<sub>2</sub>/Ne test gas needs to be designed

to recreate the non-equilibrium shock layer by recreating the major controlling factors, while the factors that cannot be recreated can be considered in a binary scaling parameter. The helium-neon substitution needs to be validated by a direct comparison between spectroscopic data measured using the existing H<sub>2</sub>/He condition and the designed H<sub>2</sub>/Ne condition. As the designed H<sub>2</sub>/Ne condition is a scaled condition with a higher density and a lower freestream velocity, the relaxation data need to be properly scaled to obtain a quantitative validation.

**4. Obtain electron number density data to assess the suitability of the existing chemical reaction models:** Compared to the radiation, electron number density would provide a more direct comparison with the computational fluid dynamics (CFD) predictions of the chemically reacting shock layer. Due to the lack of such data from representative giant planet entries, this would provide a new test case to validate the reaction schemes from the literature.

## 1.4 Thesis Structure

This thesis is presented as a combination of journal publications and traditional thesis chapters. Chapters that have been reproduced from journal papers will provide details of the original publication on their first page. An outline of the thesis is given below:

**Chapter 2 - Literature Review:** Surveys of the literature of the non-equilibrium phenomena occurring in the giant planet entry shock layers will be provided. The test gas substitution method as well as its applications will also be presented.

**Chapter 3 - Using Aerothermodynamic Similarity to Experimentally Study Non-equilibrium Gas Giant Entry (published in Journal of Spacecraft and Rockets):** The results of an investigation into the non-equilibrium shock layer in a representative Saturn entry condition will be presented. A condition using a higher fraction of helium in the H<sub>2</sub>/He test gas than in Saturn's atmosphere was tested over a test model, and the emission spectra of atomic hydrogen in the shock layer were measured. The results showed that a non-equilibrium shock layer with a slow ionization rate, which was observed in other Saturn entry tests, was generated. Thus, the substitution using a higher fraction of helium than in the atmosphere was qualitatively validated to be able to simulate non-equilibrium giant planet entry conditions.

**Chapter 4 - Experimental Validation of a Test Gas Substitution for Simulating Scaled Giant Planet Entry Conditions in Impulse Facilities (published in Experiments in Fluids):** The experimental validation of using neon as a substitute for helium in the H<sub>2</sub>/He test gas to simulate non-equilibrium shock layer will be reported. Firstly, the controlling factors for the hydrogen dissociation and ionization rates along a streamline were investigated. The H<sub>2</sub>/He condition, that has been tested in Chapter 3, was used as a reference here. A condition using H<sub>2</sub>/Ne test gas was designed by recreating the controlling factors in this existing H<sub>2</sub>/He condition. These two conditions were tested with cylindrical test models and the radiation measurements along the stagnation streamline were obtained. It was found that the designed H<sub>2</sub>/Ne condition successfully recreated the relaxation processes generated by the target condition. Thus, the helium-neon substitution was experimentally

validated.

**Chapter 5 - Electron Number Density Measurements in a Saturn Entry Condition (submitted to AIAA Journal):** The electron number density profile along the stagnation streamline generated by the H<sub>2</sub>/He condition was calculated using Stark broadening. This experimental data were compared with CFD predictions of electron number density using varying chemical reaction rate sets from the literature. It was concluded that the existing reaction scheme can be used to describe the post-shock chemistry, while adjustment of ionization rate coefficients was required to quantitatively rebuilt the experimental data.

**Chapter 6 - Conclusions and Recommendations:** A summary of this work is given and the outcomes will be described within the context of the objectives and original contributions of this thesis. Recommendations for future work will also be provided.



# Chapter 2

---

## Literature Review

---

### 2.1 Non-equilibrium Flow

For atmospheric entry conditions, a bow shock is generated around the blunt nose of entry vehicles, generating a surrounding shock layer in which aerodynamic heating including convective and radiative components occurs. In the shock layer, the kinetic energy from the pre-shock flow will be transferred to thermal and chemical enthalpy, so that the post-shock temperature can be very high. Figure 2.1 shows an example of the temperature behind a normal shock with varying earth entry velocities when the entry vehicle is at a standard altitude of 52 km. It can be seen that the post-shock temperature increases dramatically when the entry velocity gets higher. Under the calorically perfect gas assumption, where the specific heat ratio  $\gamma = 1.4$ , the post-shock temperature can be excessively high in a hypersonic scenario. However, in this high temperature environment, the energy of the gas is sufficient to cause significant chemical reactions and internal energy excitations in the shock layer, causing the specific heat  $C_p$  and  $C_v$  to vary along streamlines. As dissociation, ionization, and internal energy excitations will convert thermal energy to internal or chemical energy, the actual shock layer will equilibrate to a lower kinetic temperature than in the calorically perfect gas prediction.

For giant planet entry conditions, the chemical reactions are dominated by hydrogen dissociation and the ionization of H atoms. These reactions are a result of intermolecular collisions and require a characteristic time and multiple collisions to proceed and reach the equilibrium state. In the atmospheric entry shock layer, the time for the chemical reactions to equilibrate can be similar or longer than the time for the flow particles to travel through the shock layer. In this case, the shock layer is in a chemical non-equilibrium state.

Intermolecular collisions will also alter the internal energy distributions of species. Polyatomic elements can store energy in translational, rotational, vibrational, and electronic modes, while monotonic elements only have translational and internal electronic energy modes. One of the limiting cases is the thermal equilibrium scenario, in which sufficient collisions occur as the gas travels across a very short distance of the flowfield. In this case, all the microscopic processes that affect the species' energy exchange have reached a balanced state, and energy distributions in translational, rotational, vibrational,

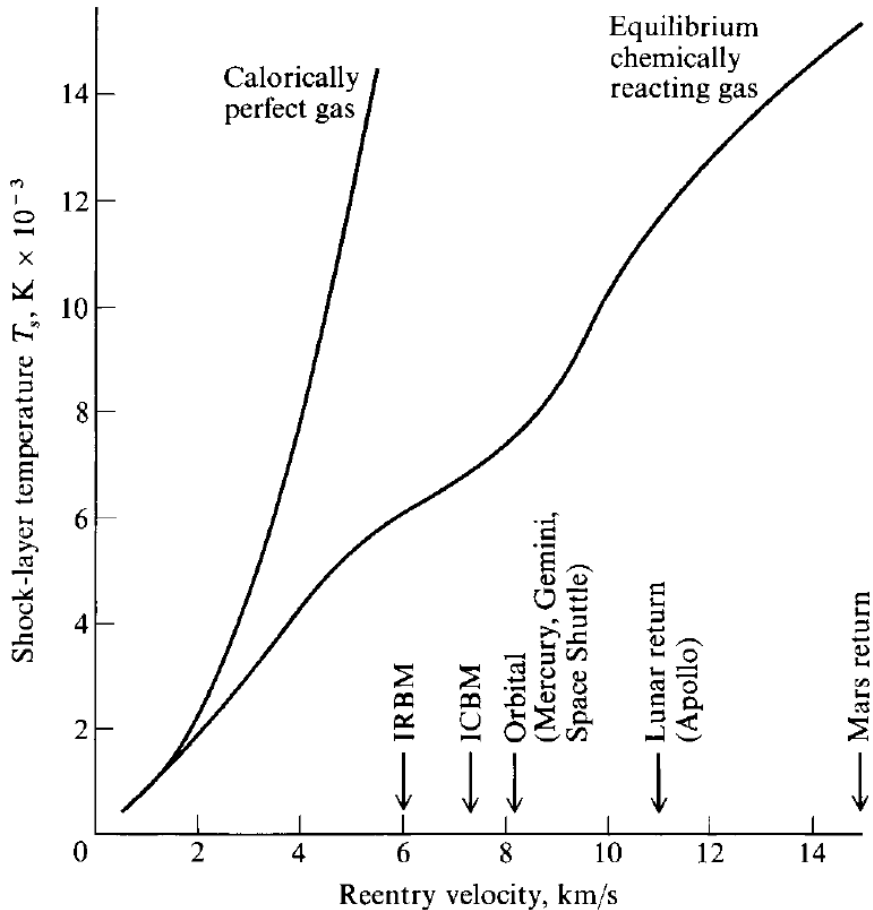


Figure 2.1: Temperature behind a normal shock wave as a function of freestream velocity at a standard altitude of 52 km. (Anderson, 2003) [13]

and electronic modes can be described by functions of a single temperature. The other limiting case is when the collisions are so rare that the internal energy states stay as in their original state. Generally, the internal energy state distributions are in between the two limiting cases, and multiple-temperature modes are required to adequately model all the processes involved. Here, temperatures represent distributions of species among allowed energy states, so that their use avoids having to model the energy levels as separate entities. A two-temperature model is commonly used to describe the energy distributions in the gas. As energy exchange between translational and rotational levels of heavy particles is usually very efficient, the rotational energy mode is assumed to be in equilibrium with the translational mode and can be defined by a single temperature. However, the vibrational-translational energy exchange is usually hindered, and electronic-vibrational energy exchange is much more efficient. Therefore, the electronic mode is commonly regarded as in equilibrium with the vibrational energy mode, and the vibrational temperature should be very close to electronic temperature [46].

Specifically, the internal energy distributions in bound electronic levels are controlled by excitation/de-excitation, ionization/recombination, and radiation. All these processes will compete with each other and have different relative effects on different states. The excitations due to collisions with heavy particles or electrons will bring the electronic states to Boltzmann distributions described by translational temperature or temperature of free electrons, respectively. Radiative transitions will deplete the

high-lying states until the transition becomes optically thick, at which point it will tend toward the electronic temperature. However, in ionizing and recombining flows the distribution will be more complicated. In these flows, the collisions will cause ionization or recombination of electrons especially in the high-lying states. This will make the high-lying bound electronic states to be in equilibrium with that for free electrons, but not necessarily in equilibrium with the low-lying ground states due to the communications between high-lying and low-lying states being inefficient. This will drive the distributions to Saha distributions [47, 48]. In ionizing flow, the ionization of high-lying electrons will cause a defect of electron number densities in the high-lying energy states, while recombination will lead to the over-population of high-lying electronic levels [46, 49].

A further consideration is radiation. It is a result of internal energy excitations, is a major form of shock layer heating during the entry, as it helps to bring the energy from outside of the boundary layer to the heat shield. Radiative heating can be comparable to convective heating in some entry conditions, such as in Galileo entry which has an extremely high post-shock temperature. In the design of the heat shields, the combination of radiative heating and convective heating is usually sufficient to predict the heating environments.

### 2.1.1 Dissociation

The dissociation of H<sub>2</sub> can be described by the ideal dissociating gas model which describes dissociation and recombination rates in chemically non-equilibrium conditions. This method was developed through a series of publications by Lighthill [50, 51] and Freeman [52], and this type of dissociating gas is often referred to as a Lighthill-Freeman gas. In the giant planet entry conditions, the dominated dissociation reaction scheme for H<sub>2</sub> can be described as: [45]



This is a reversible reaction, where M is the colliding partners including H<sub>2</sub>, H, H<sup>+</sup>, e<sup>-</sup>, and He. Defining the forward reaction rate coefficient dissociation as K<sub>fd</sub>, and the reverse reaction (recombination) rate coefficient as K<sub>rd</sub>. The species production rate of H (time rate change of the produced H molar concentration) with [] representing the molar concentration can be expressed as [45]

$$\frac{d[H]}{dt} = K_{fd}[H_2][M] - K_{rd}[H]^2[M] \quad (2.2)$$

In the literature, the forward reaction rates were usually measured via widely varying shock tube experiments or by theory. The experimental data are usually fitted empirically using the Arrhenius equation of the form:

$$K_{fd} = AT^n \exp(-E_a/kT) \quad (2.3)$$

where A and n are the constants for the model, k is the Boltzmann constant, and E<sub>a</sub> represents the threshold energy for the reaction. Backward reaction rates are usually either directly measured by experiments and fitted using the Arrhenius equation or simply derived as the ratio of forward rates and the equilibrium constant K<sub>p</sub>. The equilibrium constant K<sub>p</sub> for each chemical reaction is a function of

temperature only and can be calculated from curve fits based on experimental data or derived from thermodynamic theory.

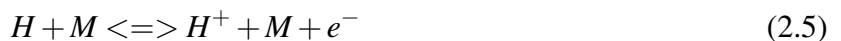
At chemical equilibrium state, forward and reverse reaction processes will reach a balanced state, where:

$$\frac{d[H]}{dt} = 0 \quad (2.4)$$

From equation 2.2, the ratio of recombination rate and dissociation rate has the unit of molar concentration, which is a function of density. In the atmospheric entry scenario, density is often very low at high altitudes, and [H] is low in the post-shock region. Thus, recombination rates are often very small and can be neglected until the flow gets close to equilibrium.

## 2.1.2 Ionization

Ionization occurs when the collisions between the H atoms and other colliding partners are energetic enough to free an electron inside the H atoms. Behind an incident shock wave, the hydrogen ionization is firstly initiated by the collision between H atoms and the heavy particles, then when the electron number density builds up, the collisions between H atoms and the electrons will be the main mechanism for ionization [25]. This mechanism was also observed in argon study [53]. The ionization by atom-electron collisions is a much faster process compared to atom-heavy particle collisions. This is because the energy transfer between the particles with equal masses is the most efficient so that the energy transfer between the bound electrons in the H atoms and the free electrons are much faster than that between the bound electrons in the H atoms and the heavy particles. Thus, the ionization mechanisms due to these two types of collisions need to be treated separately [54]. Here, M represents heavy particles or electrons.



The ionization process of H can be expressed by two steps. The electrons inside the H atoms will be firstly excited to higher energy levels, and then the subsequent collisions between excited particles H\* and other particles will lead to ionization [45]. The first step is relatively slower thus dominating the overall ionization rate [54]:



The immediate post-shock region is dominated by inelastic collisions, by which the energy is transferred from the colliding partners to electronically excite H atoms. Then, when the electron number density reaches a certain value, the elastic collisions, by which the energy is given to the free electrons from the colliding atoms and ions, will be dominant. At this stage, the electronic temperature will equilibrate to the translational temperature of the heavy particles [53]. Both the delay of the

electronic temperature rise and the delay for the electron number density increase will lead to a slow ionization rate for H atoms.

## 2.2 Modeling for Non-equilibrium Giant Planet Entry Conditions

The investigation of kinetic modeling on H<sub>2</sub>/He mixtures started in the 1970s. Before that, the knowledge of ionization processes of monatomic species was mostly gained from argon studies [54]. Leibowitz firstly proposed the kinetic model of chemically reacting H<sub>2</sub>/He gas by radiative relaxation measurements in an electric arc driven shock tube with the shock speeds ranging from 13 to 20 km/s in a 20.8% H<sub>2</sub>-79.2% He mixture (by volume) [14]. In this model, mechanisms of hydrogen dissociation, as well as two-step ionization due to atom-heavy particle and atom-electron collisions were described. A two-temperature model was used, with electronic temperature controlling the electron-impact ionization specifically. Shortly after this work, the facility was updated to an annular arc accelerator (ANAA) shock tube with a modified annular arc driver which was believed to cause less irradiation from the driver gas [40, 55] than in the previous experiments [14]. Experiments with higher shock speeds were performed by Leibowitz and Kuo in the ANAA shock tube [15]. The data obtained in the updated facility led to lower dissociation and ionization rate coefficients than in the previous study [14]. Good agreement between numerical simulations and experimental data can be found in both studies, showing that the proposed kinetic model can describe the chemical relaxation well.

Similar experiments were also performed using 84.17% H<sub>2</sub>-15.83% He test gas (by volume) in the ANAA shock tube with the shock speeds of 26-46 km/s [56]. Relaxation distance and electron density were measured from H- $\beta$  Stark broadening and holographic interferometry. These data, as well as the data from the work of Leibowitz and Kuo [15], were re-examined by a study of Park [40] to propose a theoretical model to describe the non-equilibrium processes.

To evaluate two sets of reaction rate [14, 15], Stalker [16] generated H<sub>2</sub>/Ne ionizing flows in a free piston driven non-reflected shock tunnel. Interferometry was used to measure the fringe shift to obtain the species number density variations downstream of the shock on an inclined flat plate. The data obtained were compared with the numerical predictions using the ionization rate sets from Leibowitz [14] (rate set A) and Leibowitz and Kuo [15] (rate set B) for H<sub>2</sub>/He mixtures. The results shown in Fig. 2.2 indicated that the ionization rates in the work of Leibowitz and Kuo [15] (rate set B) gave a better agreement with the measured relaxation data. This study also showed that the ionization rates of H<sub>2</sub> was not greatly affected by either using helium or neon as the inert diluent, as the measured shock layer chemistry in H<sub>2</sub>/Ne mixture had a good agreement with H<sub>2</sub>/He ionization model prediction. However, the ionization rate coefficients for H-He in Stalker's work have been interpreted the same as for H-H, which contradicts the source data [14, 15]. It could be due to Stalker using the same reduced mass when interpreting the ionization rate model for H-He and H-H collisions.

The chemical reaction model from Leibowitz and Kuo [15] was then used in Jupiter entry studies. This reaction scheme was used by Tiwari and Szema [57, 58] to compare the aerodynamic heating for the proposed Jupiter entry under equilibrium and non-equilibrium states. Also, chemical non-

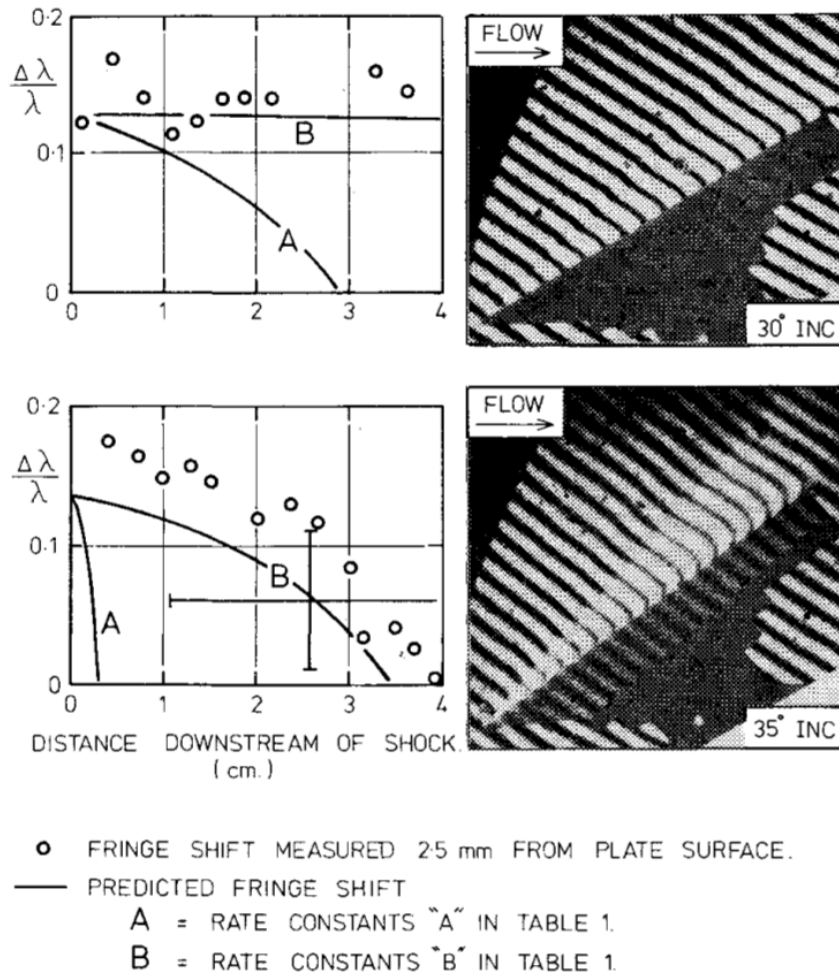


Figure 2.2: Comparisons between relaxation downstream of oblique shock measured in Stalker's experiments and predicted using ionization rates from Leibowitz [14] (rate set A) and Leibowitz and Kuo [15] (rate set B). (Stalker, 1979) [16]

equilibrium simulations were performed with or without ablation injection. It was found that the radiative heating was substantially higher when non-equilibrium processes were included. The effect of the non-equilibrium tended to be more significant at higher entry altitudes in which the density was lower, and it was much weaker in the peak heating point. The presence of ablative produces was also found to significantly increase the convective and radiative heating.

In 1995, the Galileo probe entered the atmosphere of Jupiter at a relative velocity of 47.4 km/s. During the deceleration from Mach 50, the peak heating rate and heat load on the forebody were around  $30 \text{ kW/cm}^2$  and  $300 \text{ kJ/cm}^2$ , respectively. This makes the Galileo entry the most severe entry that mankind has ever performed in terms of the heating load.

During the design of Galileo's heat shields, numerical predictions of the shock layer recession were performed using the latest numerical models in the 1970s and 1980s [34, 59]. Final predictions of the heat shield's recession were conducted using two separate codes: COLTS (Coupled Laminar and Turbulent Solutions), a viscous shock layer code developed at the NASA Langley Research Centre [60]; and TOPIC (Thermodynamic Outer Planets Insulation Code), an engineering code which combined computations and correlations of CFD and experimental data for a large number of flow factors [61].

In the COLTS's prediction, 10% surface reflectance and fully turbulent assumptions were used [34]; whereas in the prediction of TOPIC, a non-reflecting surface was assumed, and abrupt transition to fully turbulent flow was considered at a boundary-layer edge Reynolds number of  $10^5$  [59]. In these pre-flight predictions, as dissociation and ionization was assumed to complete immediately after the shock, the shock layer was assumed to be in chemical equilibrium.

The Galileo probe had a sphere-cone shape with a nose diameter of 22.2 cm and with 44.86 degree cone-half-angle. In the forebody of the heat shield, 10 ARAD sensors and 4 thermometers were mounted to respectively detect the heat shield ablation and temperature during the entry [17, 18]. The location of the sensors is shown in Fig. 2.3. The recession data showed that only half of the heat shield ablated during entry. It was also found that 100 mm of material was left in the nose region, while only 10 mm thick material was left in the frustum region. Comparison between in-flight recession measurements [18] and CFD predictions in the pre-flight heat shield design [34, 59] (shown in Fig. 2.4) indicates that both numerical models used over-predicted the recession on that stagnation region, while the frustum recession was under-estimated.

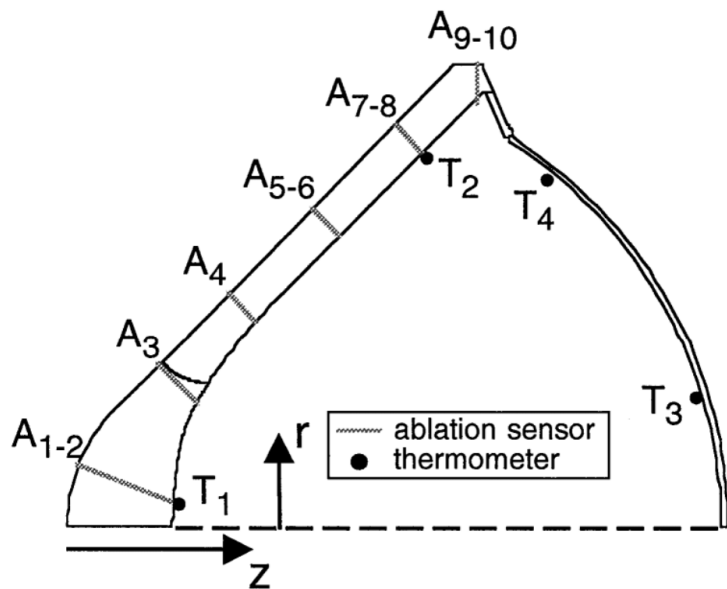


Figure 2.3: Locations of 10 ablation sensors ( $A_1$ - $A_{10}$ ) in heat shield and four resistance thermometers ( $T_1$ - $T_4$ ) inside structure; sensors are not coplanar. (Milos et al., 1999) [17]

Due to the discrepancy between the flight recession data and pre-flight simulations, there was a desire to understand where the discrepancy came from. Further analysis showed that the discrepancy between numerical prediction and flight data can be explained by several reasons:

1. The pre-flight prediction was conducted with the assumption of an equilibrium shock layer, while in flight non-equilibrium effects may exist in the immediate post-shock region. Furudate et al [62] investigated the thermochemical non-equilibrium effects on the heat flux in the stagnation region. They found that the over-estimation of the stagnation point recession could be due to the ignoring of the ionization delay in the preflight prediction [62]. Another study also showed that ignoring this non-equilibrium effect would lead to the over-estimation of radiative gas thickness, thus

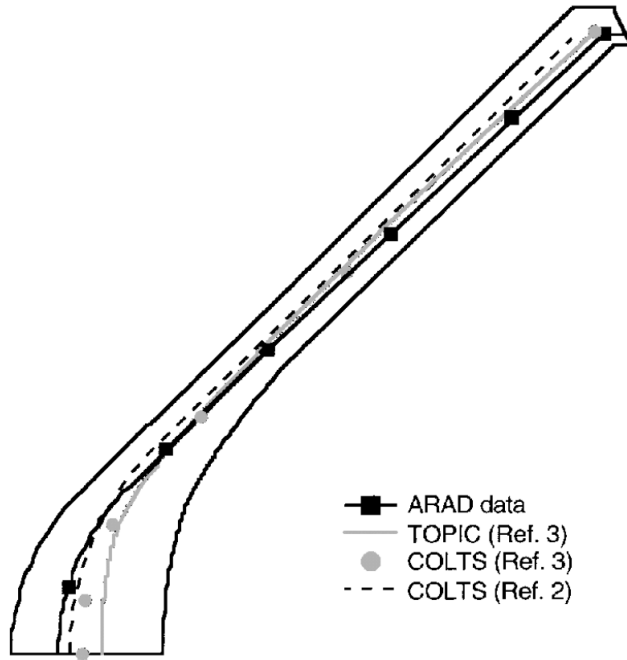


Figure 2.4: Comparison of final shape with pre-flight predictions. (Milos, 1997) [18]

the stagnation region heating would be over-predicted [63].

2. The helium mole fraction in Jupiter's atmosphere was assumed to be 11% before the mission, whereas the in-situ measurements showed that the helium mole fraction is 13.6% [64, 65]. The under-estimation of helium mole fraction will lead to the under-prediction of the post-shock temperature. Hence the actual radiative heating rate will be higher than predicted.

3. The interaction between ablation products and the boundary layer was not considered for the numerical prediction, and a fully turbulent flow with a smooth wall was assumed. However, due to injection of the flow with ablation products, the surface would have likely been rough [66], and the injection-induced turbulence was likely to have occurred [35]. This may have led to a higher heating rate than in the pre-flight prediction. Matsuyama et al [19] firstly used the updated gas component (13.6% instead of 11% helium) to investigate the Jupiter entry heating environment. In his work, additional turbulence caused by the ablation products was modeled, and was found to be the cause of the under-prediction of the frustum region recession. The comparison of Matsuyama's forebody recession profile with flight data and preflight prediction is shown in Fig. 2.5. It can be seen that with these updated models, although the equilibrium assumption was used in the study of Matsuyama et al [19] (shown as present), the recession in the frustum region during the flight was approximately rebuilt, whereas the stagnation point recession was still not matched.

In 2004, Park [67] investigated the effect that precursor radiation might have on the chemical relaxation in the shock layer during Galileo entry. In the kinetic model from Leibowitz [14] and Leibowitz and Kuo [15], the initial electrons are produced by ionization caused by heavy particle collisions and then the electron-impact ionization (or the so-called ionization avalanche) would be initiated when the electron number density becomes sufficient. However, using this kinetic model, the un-ionized region in the shock layer at the peak heating point of the Galileo probe was surprisingly

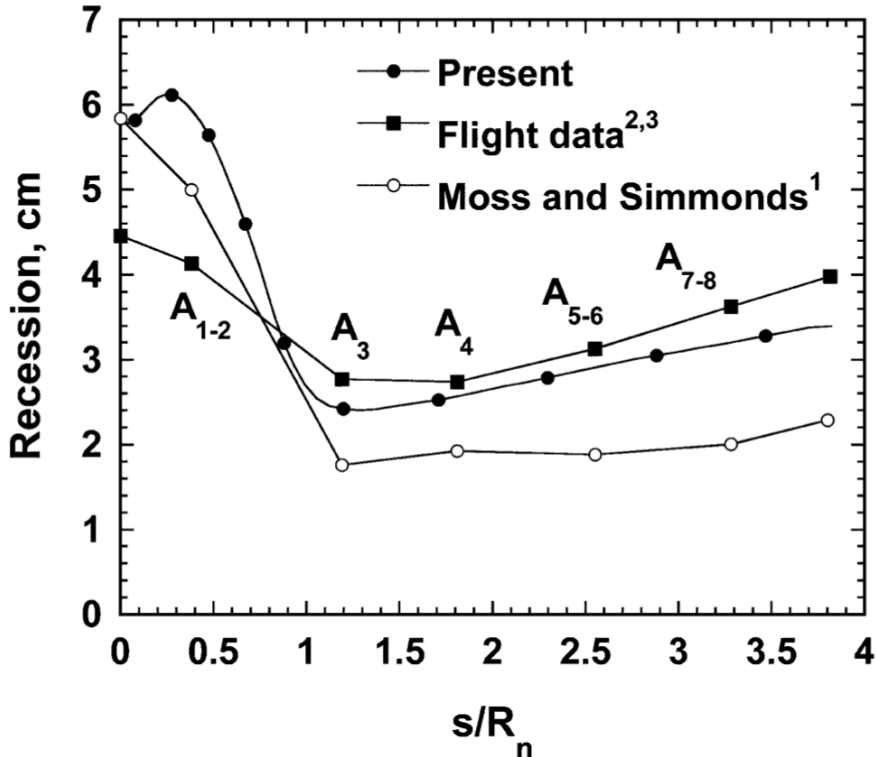


Figure 2.5: Comparison of obtained final forebody recession profile in Matsuyama's work with flight data and preflight prediction. (Matsuyama, 2005) [19]

thick. Hence, for this strongly radiating shock layer, Park [67] proposed an initial electron generation mechanism by considering photo-ionization. The vacuum ultraviolet (VUV) radiation from a highly ionized area travels upstream to in front of the shock and causes the photo-ionization of molecular hydrogen and H atoms to produce electrons. Then, when the electron number density is sufficient and electrons are heated to a certain value of the threshold, electron-impact ionization will become dominant. This ionization kinetic model which takes into account the photo-ionization in the precursor region was then used by Furudate [68]. In this work, the dissociation model from Leibowitz [14] and the ionization model from Park [67] were implemented. Numerical investigations were performed with shock tube experimental conditions in Leibowitz [14]. It was found that the photo-ionization was only significant in very high speed entry conditions like Jupiter entry, and the degree of photo-ionization was very low in these conditions and only raised up to 0.9% when the shock speed increased to 38 km/s. Furthermore, for the high speed conditions, the numerical prediction of ionization time agreed with experimental data better when photo-ionization was modeled.

Recently, sensitive studies for Galileo entry heating prediction were performed by Santos Fernandes et al. [37] to understand the discrepancy between recession flight data and numerical prediction. The impact of phenomena that have been either neglected or inadequately modeled in the past has been conducted. In this study, the transport property model, internal excitation of H<sub>2</sub> due to radiation absorption, and thermal non-equilibrium were found to play important roles in the radiative heating prediction. The chemical reaction model from Leibowitz and Kuo [15] was employed in this work. However, the ionization rates used in the work of Santos Fernandes et al. [37] were two orders of

magnitude lower than in the original source [15] as they used SI units instead of cgs units in the original work without converting the rates. Further, Santos Fernandes et al. [37] has omitted the rate with lowered activation energy that is assigned to the two-step ionization process. In 2020, Erb et al. [38] made some improvements in the modeling based on the advances made in the past studies. For example, the shape change of the probe and multicomponent diffusion of species were modeled in this work. With these additional modeling features that are not in the previous studies, the work of Erb et al. [38] provides the most accurate recession prediction for the Galileo probe TPS material to date.

For the entries into Saturn and Uranus, Palmer et al. [25] selected three proposed entry trajectory points for each entry from the literature and evaluated the uncertainties in numerically predicting the aerodynamic heating. It was found that, for all the selected trajectory points, the shock layers were in non-equilibrium states. A slow ionization was also observed before the electron number density builds up to a sufficient value. Aerodynamic heating in the proposed Uranus entry trajectories was dominated by convective heating, while radiative heating contributed up to 20% of the total heat load at the highest velocity point examined for Saturn entry. The uncertainty for predicting convective heating was mainly from the modeling of the catalytic wall and boundary layer in which recombination and transport processes occur. For the conditions where radiative heating is important, the thermochemical non-equilibrium process was the major uncertainty driver. Generally, uncertainty in convective heating prediction was less than a few percent, whereas the uncertainty for radiative heating was substantial.

Following this, shock layer radiation measurements were performed in EAST to study the representative Saturn and Uranus entry shock layers [20]. It is worth noting that this facility was previously reported to have radiation from the electric arc driver and thus test gas could be pre-heated [69]. After adding aluminized polyester buffer diaphragm, the test gas could be protected from driver gas radiation and pre-heating had been successfully mitigated in these tests. Radiation measurements were conducted at freestream pressures between 13 and 66 Pa (0.1 and 0.5 torr) and velocities from 20 to 30 kms, with a 89% hydrogen-11% helium test gas. Spectroscopic measurements were conducted in VUV, ultraviolet (UV), visible, and near-infrared (NIR) spectral ranges. The data showed that the radiation in conditions with shock speeds below 25 km/s could not be detected by the optical instrumentation due to the relatively low temperature. The majority of Uranus entries would fall into this category. For the Saturn entry conditions between 25-30 km/s, the shocks did not equilibrate until several centimeters behind the shock front, and a slow ionization rate was observed. The radiation data were then compared with numerical predictions using NASA's line-by-line radiation solver NEQAIR [70] in which Boltzmann distributed state populations were used. It was found that a numerical rebuilding of the radiation measurements was still difficult, as NEQAIR over-predicted these conditions by as much as a factor of 10. A Boltzmann distribution was also found to be not adequate to describe the internal states distributions well. In this study, electron number density and electronic temperature were calculated based on Stark broadening of Balmer transitions. Consistent with radiation observation, the electron number density and temperature results display a delayed rise behind the shock front. In most cases, the electron number density did not reach equilibrium during the measured test time. The electron number density and temperature measurements from the work of Cruden et al. [20] were

also employed in the work of Colonna et al. [41] to validate a state-to-state chemical kinetics of the H<sub>2</sub>/He mixture. It was found that the newly proposed kinetics with an alternative path to ionization had satisfactory agreement with both electron number density and temperature measurements.

The experimental data from EAST were then numerically simulated using Direct Simulation Monte Carlo (DSMC) method [21], with the reaction model from Leibowitz and Kuo [15] implemented, and the radiation based on the predicted shock layer properties was calculated by NEQAIR. Radiance in VUV, UV, visible, NIR spectral ranges were simulated and compared with EAST measurements [70], and the radiance comparison in UV spectral range is shown in Fig. 2.6. It was found that the radiation measurements in these wavelength ranges can only be qualitatively simulated, but the measured radiation data were over-predicted, and the induction time of radiation was not shown in numerical results. The comparison of the electron number density showed that the magnitude of the predicted value was close to experimental data, but the trend was different. The discrepancies could be due to many reasons: incorrect backward reaction rates; a non-Boltzmann distribution was used in DSMC while the Boltzmann distribution was used in NEQAIR; and electronic excitation of H atoms not included in electronic temperature definition.

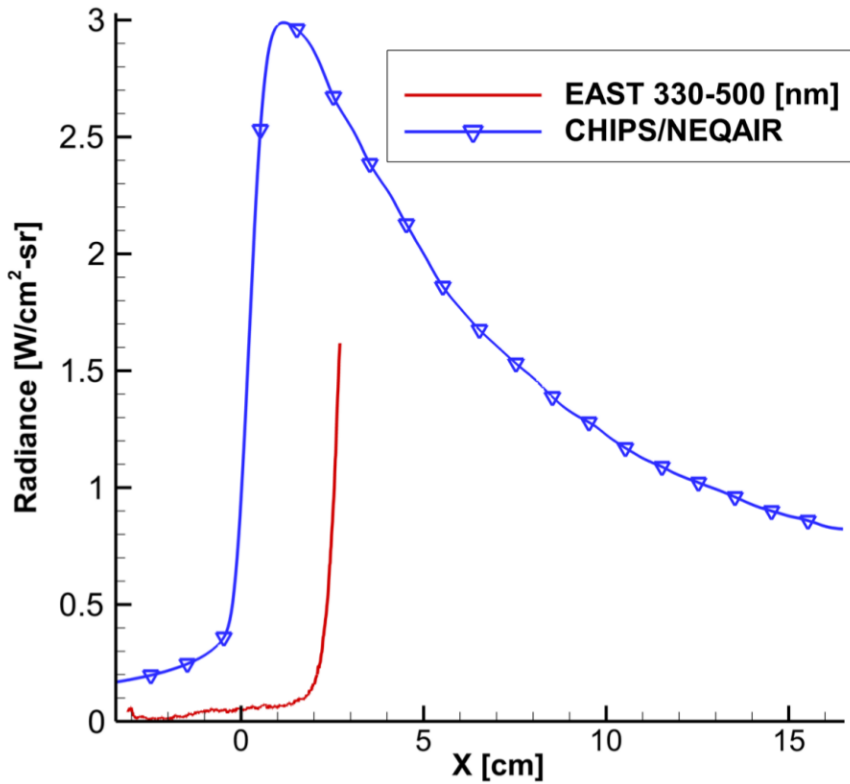


Figure 2.6: Comparison of UV range radiance between EAST measurements (shot 17) [20] and DSMC/NEQAIR prediction [21]. (Higdon et al., 2018) [21]

## 2.3 Test Gas Substitution in an Impulse Facility

Due to the entry speeds of over 20 km/s, the shock layer in the giant planet entries cannot be directly simulated by most of the impulse facilities using the test gas with their atmospheric compositions. In

1998, Stalker and Edwards [22] proposed a substitution using a heavier test gas (increased fraction of helium in the H<sub>2</sub>/He or using neon to substitute helium as the inert gas) to simulate giant planet entry conditions. In the entry conditions of Saturn, Uranus, and Neptune, helium or neon can be considered mainly as inert collision partners and only participate in heavy particle collisions, as their ionization potential (helium: 24.6 eV, neon: 21.6 eV) are sufficiently higher than that for hydrogen (13.6 eV), and their ionization is negligible in most of these conditions. Thus, the substitution will not greatly affect the chemical reaction mechanisms.

Theoretical validation of the substitution method was performed in the work of Stalker and Edwards [22] to investigate if the substitution method can enable non-equilibrium processes in the shock layer to be simulated. In this study, the similarity was defined as the distribution of flow properties (such as velocity, pressure, and density) in the shock layer of one condition can be reproduced using another condition. They found that, for a given post-shock temperature and pressure, the fraction of helium or even the type of diluent (helium or neon), did not greatly affect the relaxation process. Four requirements were essential to evaluate the similarity [71]. The first three requirements were mainly about the geometry of the blunt body and the shock, as well as the angle of incidence, which can be easily satisfied if only the relaxation along the stagnation streamline was considered. The fourth requirement, which required the density ratio across the shock (freestream density/immediately post-shock density) to match in the two conditions, was more difficult to satisfy.

Hydrogen dissociation and ionization are dominated by binary collisions, so that a binary reaction variable was introduced to present the relaxation rate in the shock layer:

$$\chi = \int \frac{rP}{V} ds \quad (2.8)$$

Here  $r$  is the mole fraction of hydrogen,  $V$  is streamline velocity and  $s$  is the stream-wise distance.

To investigate the effect of diluent concentrations and types, post-shock density ratios along  $\chi$  were numerically calculated in H<sub>2</sub>/He and H<sub>2</sub>/Ne mixtures with varying diluent fractions. In this study, dissociation was assumed to be essentially complete close to the shock. The results in Fig 2.7 showed that, when frozen post-shock temperature and pressure were reproduced, there was no noticeable difference using helium or neon as the diluent. Also, changing the fraction of the diluent (helium or neon) did not significantly change the relaxation processes. The density ratio profiles with varying post-shock temperature and pressure were calculated and shown in Fig. 2.8. It can be found that the substitution method stayed valid except approaching equilibrium. When the flow approached equilibrium, the variation of the post-shock pressure led to the variation of the equilibrium density ratio. This was due to stronger recombination in higher post-shock pressure cases. As recombination is not a binary process, the binary reaction variable was no longer effective in correlating the rise in density when approaching equilibrium. Also, at the highest temperature case in this figure, neon began to ionize so that there was divergence in the scaled density ratio profiles by using neon or helium as the diluent.

To summarize, by maintaining the post-shock temperature and pressure, changing the mole fraction of the diluent (helium or neon) or whether using helium or neon as diluent did not greatly affect the

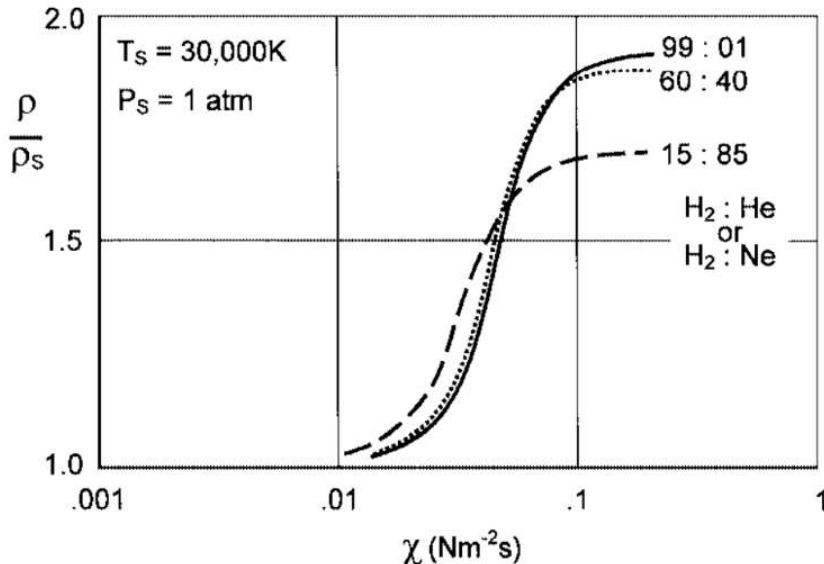


Figure 2.7: Ionizing relaxation: effect of diluent type and concentration. (Stalker and Edwards, 1998) [22]

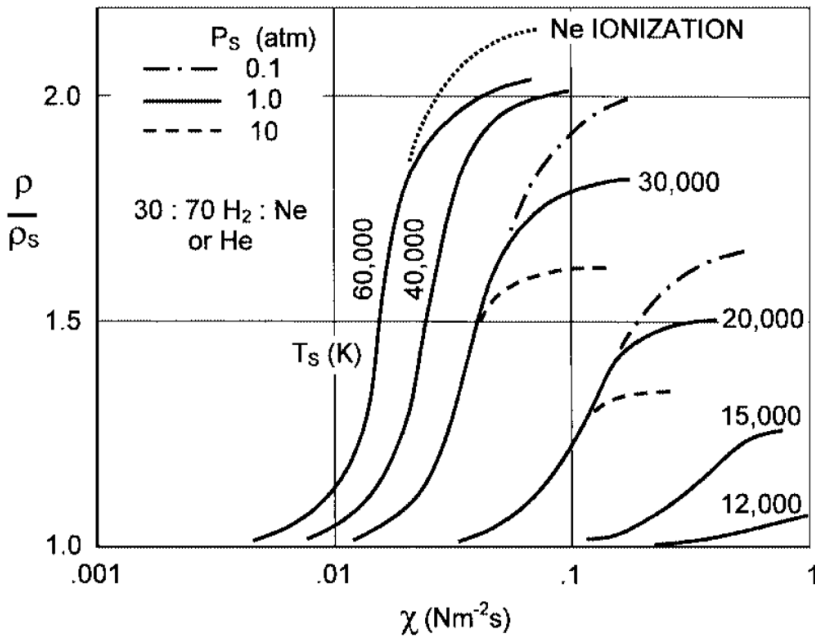


Figure 2.8: Ionizing relaxation: effect of temperature and pressure. (Stalker and Edwards, 1998) [22]

normalized post-shock density variation along the binary scaling variable  $\chi$  when the helium and neon act as only the heavy particle collision partners. Thus, the similarity in the non-equilibrium processes can be achieved by employing this substitution theory.

Helium's specific heat is lower than that of hydrogen. By increasing the fraction of helium in the test gas, the specific heat of the gas mixture will be decreased, so a higher post-shock temperature can be achieved given the same freestream enthalpy. Neon is a heavier gas with the specific heat four times lower than that for helium, so that using  $\text{H}_2/\text{Ne}$  instead of  $\text{H}_2/\text{He}$  can further decrease the specific heat, and can provide more rooms to generate a higher temperature for a given freestream enthalpy.

Hence, this method makes it possible for post-shock temperature in giant planet entries, which cannot be simulated within the facilities' performance envelope with the atmospheric composition, to be recreated in the ground testing facilities. By recreating the post-shock temperature, the post-shock relaxation processes will be able to be simulated.

The substitution using H<sub>2</sub>/Ne instead of H<sub>2</sub>/He test gas was used by Stalker [16] to generate ionizing flows in a shock tunnel to study ionization rates for H<sub>2</sub>/He mixtures. In this study, measured species number densities had a good agreement with one H<sub>2</sub>/He ionization reaction rates set within the uncertainty range, showing that H<sub>2</sub>/Ne has similar reaction mechanisms to H<sub>2</sub>/He. This numerically confirmed the similarity of chemical reaction mechanisms between the H<sub>2</sub>/He and H<sub>2</sub>/Ne mixtures, which was subsequently confirmed by experiments.

Higgins [45] then used 85%/15% H<sub>2</sub>/Ne (by volume) to simulate highly ionizing giant planet entries at the X2 expansion tube [42] at UQ. Near-resonant holographic interferometry and two-wavelength holographic interferometry were both employed to measure the electron number density and shock standoff. The experimental results were compared with the analytical results, which assumed that chemical similarity could be achieved using H<sub>2</sub>/Ne to substitute H<sub>2</sub>/He. Good agreements were found between shock standoff measurements and analytical predictions, and allowed for the estimation of shock layer Damköhler number for the ionization processes. This experimentally validated the substitution theory for the shock standoff, showing the possibility to simulate non-equilibrium giant planet entry, as shock standoff is strongly dependent on chemical reactions in the non-equilibrium shock layer. However, in this study, H<sub>2</sub> in the freestream was found to be nearly fully dissociated, leading to a large chemical enthalpy. This doesn't match the flight condition in which the gas is in a molecular state, and leads to the disagreement between the non-equilibrium electron number density measurements and numerical predictions. Also, neon was found to be partially ionized in this study, which is beyond the limit of the substitution theory [22].

Subsequently, James et al. [23] investigated the possibility of using the substitution method to simulate non-equilibrium Saturn and Uranus entry conditions in X2. A test condition using the highest performance driver condition and with a reasonable shock speed uncertainty was selected. A post-shock temperature generated by this condition with diluent fractions ranging from 10% to 90% was calculated, and the results are shown in Fig 2.9a and Fig. 2.9b. It was found that higher post-shock temperatures were generated with increased fractions of diluent. With this driver condition, both H<sub>2</sub>/Ne or H<sub>2</sub>/He test gases can be used to generate equilibrium and frozen temperatures in selected Saturn and Uranus entries. This study also showed that using neon diluent could easily generate the post-shock temperatures required to simulate the proposed Uranus and Saturn entries. This indicates that with the same diluent fraction, a less powerful driver condition can be used to simulate these entries with a H<sub>2</sub>/Ne test gas. Therefore, more facility performance can be left to generate scaled conditions with a lower velocity and a higher density, thus further relaxation can be generated. Similarly, this substitution can also be used to simulate Jupiter entry, with some confounding effects due to incipient neon ionization which have to be taken into account.

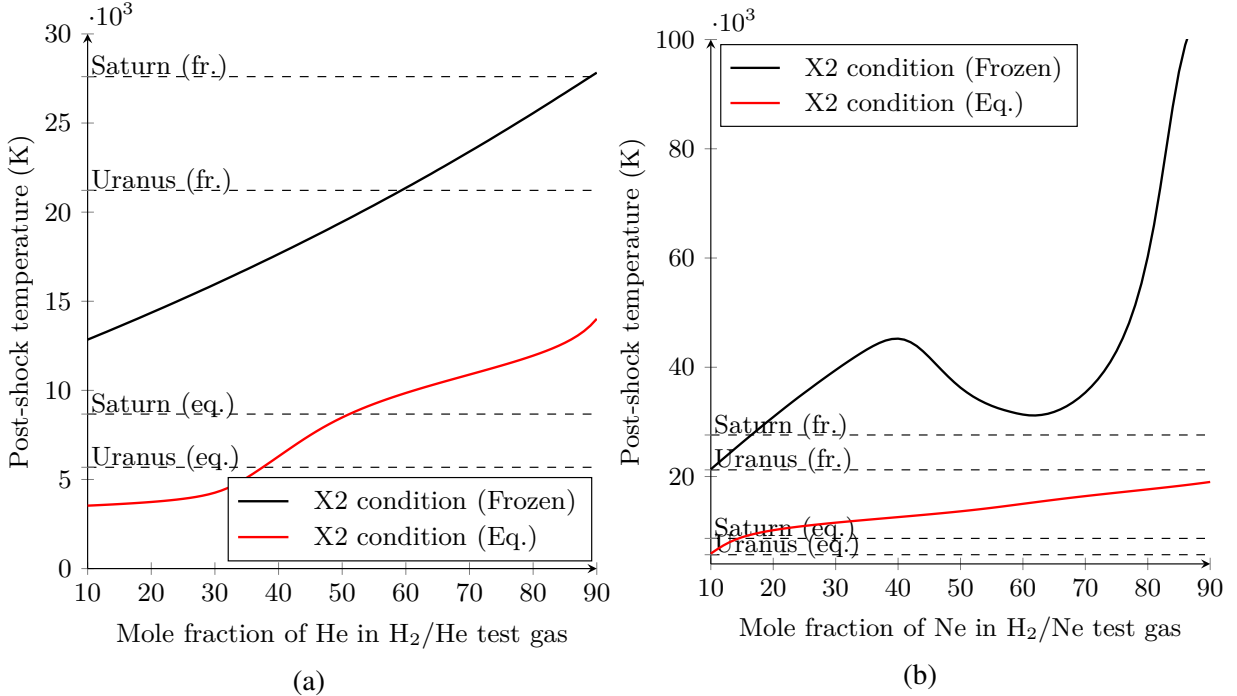


Figure 2.9: Effects of helium or neon fraction on post-shock temperature. (James et al., 2018) [23]

## 2.4 Summary

Shock layer temperatures at frozen states occurring in the proposed entries into Uranus, Saturn, and Neptune are normally over 20000 K, while that for Jupiter entry can even exceed 40000 K. This high temperature environments can lead to  $H_2/He$  non-equilibrium phenomena, thus introducing significant uncertainties in the heating environment prediction. In the literature, studies on these non-equilibrium processes are mainly on numerical modeling, and most of them are validated against the macroscopic flight data from Galileo probe's entry into Jupiter.

For the proposed Saturn, Uranus, and Neptune entries, as the entry speeds are lower than that for Jupiter, non-equilibrium region would be larger and these phenomena in the shock layer will be more dominant for aerodynamic heating. Due to the proposed giant planet entry conditions being beyond the performance envelope of most ground testing facilities, direct ground testing of Saturn and Uranus conditions have only been performed in NASA's EAST shock tunnel with measurements of radiation and electron number density. However, significant discrepancies still exist when comparing the state-of-the-art numerical calculations and experimental measurements. Numerically rebuilding the radiation and the chemical non-equilibrium processes is still difficult, and more ground testing data are essential to further develop and validate the numerical modeling of non-equilibrium shock layer and radiation.

A test gas substitution method was used and investigated to enable ground testing of the entries into Saturn, Uranus, and Neptune to be performed in our X2 expansion tube. Past studies have shown that, by using the substituted test gas, macroscopic properties like shock standoff can be simulated, and post-shock temperature in the proposed Saturn and Uranus entries can be achieved within X2's performance envelope. However, to use this method in simulating the non-equilibrium shock layer, experimental

validation against radiation measurements is still required, which is the primary contribution of this thesis.

## Chapter 3

---

# Using Helium Enhancement Substitution to Study Non-equilibrium Giant Planet Entry

---

**Reproduced entirely from a paper published in the Journal of Spacecraft and Rockets [1]:**

Yu Liu, and Christopher M. James, and Richard G. Morgan ,and Timothy J. McIntyre, “Using aerothermodynamic similarity to experimentally study non-equilibrium gas giant entry,” *Journal of Spacecraft and Rockets*, 57(5):1008-1020, 2020.

See *Publications included in this thesis* in the preamble of this thesis for a statement of the author contributions to this paper. Some minor changes were made to the as-published paper for the purposes of inclusion into this document, and are detailed in Appendix A The Introduction has also been adjusted to avoid overlapping contexts among chapters.

### Abstract

Peak heating points for the entry into Uranus, Neptune, and Saturn exhibit highly nonequilibrium shock layers, and are not well understood. This paper describes an experimental study in the X2 expansion tube at the University of Queensland, using a condition with a higher concentration of helium than exists on Saturn, with a shock speed of 18 km/s, to simulate radiation during blunt body Saturn entry at 26 km/s. High speed imaging and emission spectrometry were employed to measure shock layer radiation. Axial and radial spectroscopic measurements were performed through planes along and perpendicular to stagnation streamline, and an Abel inversion was used to quantify the radial radiation profile. Regions at different non-equilibrium stages were identified by radiation measurements. Non-equilibrium shock layers with a slow ionization rate, which were observed in other Saturn entry radiation tests, were successfully recreated. This study shows increasing the amount of helium enables expansion tubes or other facilities to simulate non-equilibrium giant planet entry, thus providing more ground testing data for future study.

### 3.1 Introduction

The giant planet–Jupiter, Saturn, Uranus, and Neptune–are four gaseous planets in our solar system that are composed mainly of hydrogen and helium. After the successful Jupiter entry performed by Galileo probe, and Cassini’s 13 years travel in the Saturnian system, NASA is currently considering a potential Uranus Orbiter and Probe mission, which is the current decades next-highest priority planetary flagship mission [30]. Thus, technology investments must be made to reduce the cost and risk of these missions [26].

At peak heating for the entries into Uranus, Neptune, and Saturn, the post-shock flow will be highly non-equilibrium. These include dissociation of the hydrogen molecules, ionization of the resultant hydrogen atoms, and the associated non-equilibrium radiation field which forms a main contributor to heating. This chemically non-equilibrium process can be characterized as three stages, with H<sub>2</sub> dissociation and subsequent ionization due to two types of collisions. Ionization is initiated by heavy particle collisions. Then when the number of electrons is high enough, e<sup>-</sup>-H collisions will be fully excited and become the main ionization mechanism [54]. For the ionizing stage dominated by e<sup>-</sup>-H collisions, initially electron number density is relatively low, collisions between electrons and atoms will lead to the electronic excitation inside atoms. These collisions are inelastic, and will decrease the energy in colliding electrons. When the electron number density reaches a certain value, elastic collisions, which lead to energy transferring from heavy particles to free electrons, will be dominant. As the elastic heat transfer rate exceeds the inelastic rate, electronic temperature will equilibrate to the translational temperature of the heavy particles [53]. The delayed increase in both electron number density and electronic temperature result in a slow ionization rate in the post-shock flow.

The non-equilibrium shock layer and the associated heating environment for the proposed Saturn and Uranus entry trajectories have been numerically investigated by Palmer et al. [25]. It was found that the radiative heating is significant in the total heating for the proposed Saturn entry at around 26 km/s, while for the Uranus entry trajectory at around 22 km/s, radiative heating is negligible. Also, hydrogen dissociation and recombination were observed to be the most important factors to numerically predict the heating rate. Neptune entry would show similar behaviour to Saturn, as the proposed velocities are around 29 km/s [32], and Neptune has a similar atmospheric composition to Saturn. The entry velocity for Galileo probe during Jupiter entry was around 47.5 km/s [18]. During Jovian entry, dissociation processes finished directly behind the shock, before significant ionization occurred. Radiation was the major heating source for the TPS, and comprised 99% of the total heat load [18].

In the design of the Galileo probe, due to the lack of knowledge about the radiative heating environment, a wide safety margin was included in the heat shield design to ensure the safety of the spacecraft. Thermal protection system of the Galileo probe occupied nearly half of the total mass, but only half of the heat shield ablated during the entry [18, 72]. This highlights the potential for improvements in modeling to allow the design of a more heat efficient probe and enable a larger scientific payload to be carried. Currently, there are a few studies about the updated recession models

for TPS of Galileo probe [19, 36, 38] and updated transport property model for shock layer flow prediction [37]. These numerical predictions were compared with flight data. Apart from that, there is very little blunt body test data for giant planet entry conditions available for numerical comparisons.

To have a better understanding of the aerothermodynamics during giant planet entries, more experimental data are needed to study the non-equilibrium processes and to develop better numerical models. However, the cost and time frame for flight experiments are prohibitive, since missions to the outer planets can take many years to arrive. Ground testing is a more efficient way to generate useful data and to help understand these entry phenomena. Nevertheless, creating the proposed entry velocity and total pressure is beyond the capability of most impulse facilities, so that no blunt body experimental test is achievable at the relevant flight conditions with the actual gas composition of Saturn's atmosphere.

Cruden and Bogdanoff [20] studied shock layer radiation for the selected Saturn and Uranus entry conditions in EAST, using a hydrogen-helium mixture representative of their atmospheres. They found that the shock layer was highly non-equilibrium and did not equilibrate over several centimeters. A slow ionization rate was also observed for the Saturn entry condition. It was also found that the electron number density and the temperature have delayed rises after the shock. They found that the electronic levels for hydrogen atoms did not follow a Boltzmann distribution, which makes the radiative field very difficult to numerically predict. Because of its design, as a non-reflected shock tube, EAST is not able to establish steady flows over a test model due to its short test time. The X2 expansion tube at the University of Queensland [42] is a useful alternative to study these planetary entries. X2 is appropriate for tests that include more complicated blunt body measurements, such as ablation tests [73, 74] or heat flux measurements [75]. However, the entry velocities and densities for the proposed giant planet entries are not achievable in X2, so a substitution is required to experimentally simulate the non-equilibrium process during these entries with achievable shock speeds.

An alternative option is to generate a flow that only simulates the shock layer. This can be performed using the substitution method proposed by Stalker and Edwards [22]. They found that, by maintaining the immediate post-shock temperature and pressure, changing the fraction of the inert gas He in the H<sub>2</sub>/He test gas did not significantly affect the density variation normalized by the immediate post-shock density on a post-shock streamline. Increasing the fraction of helium can decrease the specific heat of the test gas, and reduce the flow enthalpies required to simulate giant planet entries. Thus, for a specific ground testing facility, by increasing the fraction of helium in H<sub>2</sub>/He test gas, hotter shock layers can be achieved within the same performance envelope.

James et al. [23] studied how the amount of helium in the test gas can affect the post-shock condition. His study showed that the post-shock temperature of the proposed Saturn entry that was analyzed by Palmer et al. [25], could be simulated in X2 using an increased amount of helium diluent in the test gas. Conditions with different diluent amounts were tested in X2 and using a high speed camera it was found that higher levels of luminosity in the shock layer were observed with a higher amount of helium in the test gas. However, the images obtained were not spectrally filtered, and it was suggested that contaminant radiation from the facilities aluminum foil secondary diaphragm may have

been radiating significantly and affecting the measured total radiation. Also, the models used were small pitot pressure probes, which gave a limited shock standoff distance to study the non-equilibrium process in the shock layer.

In this study, an X2 condition with the 80%/20% helium/hydrogen (by volume) test gas was chosen to simulate Saturn entry radiation with the shock speed of around 18 km/s. This condition was theoretically validated by James et al. [23] to be able to generate a post-shock temperature representative of a Saturn entry trajectory point at around 26 km/s. In this paper, a truncated sphere was used as the test model to generate as large a bow shock as possible. The shock layer was observed by a H- $\alpha$  filtered high speed camera, and spectra from the Balmer series of atomic hydrogen lines from 400 nm to 690 nm were obtained using emission spectroscopy. The obtained data were analyzed and compared to those from EAST Saturn entry radiation tests [20], to validate that the radiative field has been simulated. This study is the first time that spectrally resolved radiation from representative giant planet condition has ever been captured with a test model, also the first time that H-alpha filtered radiative shock layer images are obtained and analyzed for giant planet conditions in X2. The objective of this study is to experimentally verify that increasing the helium fraction in the test gas can help expansion tube facilities exceed their speed limitations for direct simulation of giant planet entry radiation in the shock layer. This will enable expansion tubes such as X2 to perform a wider range of blunt body measurements, to provide unique datasets for the validation of computational codes used in future giant planet entry study. This substitution can also make it possible for other ground testing facilities to simulate non-equilibrium process that occurs in giant planet entries.

## 3.2 Facility and Test Condition

### 3.2.1 X2 Expansion Tube and Test Condition

The X2 expansion tube is a super-orbital facility that is able to produce flow velocities up to 20 km/s [9], with steady test times ranging from 10  $\mu$ s to 300  $\mu$ s. A detailed description of X2 is given in previous work [24, 42], and a schematic diagram of X2 is shown in Fig 3.1. X2 can be configured with a variety of established driver conditions which are controlled by the gas filling condition in the driver tube (100% He, 10%/90% Ar/He or 20%/80% Ar/He), and the thickness of the primary diaphragm (1.2 mm, 2.0 mm or 2.5 mm). Most of these driver conditions are described in detail by Gildfind et al. [76, 77].

X2 is powered by a lightweight piston in the driver tube, with the release of the piston leading to adiabatic compression of the driver gas. When the pressure difference between the driver tube and the shock tube reaches the rupture pressure of the steel diaphragm in between, it bursts, generating a shock wave that passes through the shock tube. The test gas filled in the shock tube will be accelerated by this shock wave. Then, when the shock arrives at the secondary diaphragm, which is a thin aluminum foil, the secondary diaphragm will burst, generating the second shock wave traveling into the acceleration tube gas. The test gas, which moves behind the second shock wave, will experience an unsteady expansion in the acceleration tube. During the expansion, the shock heated test gas will gain total

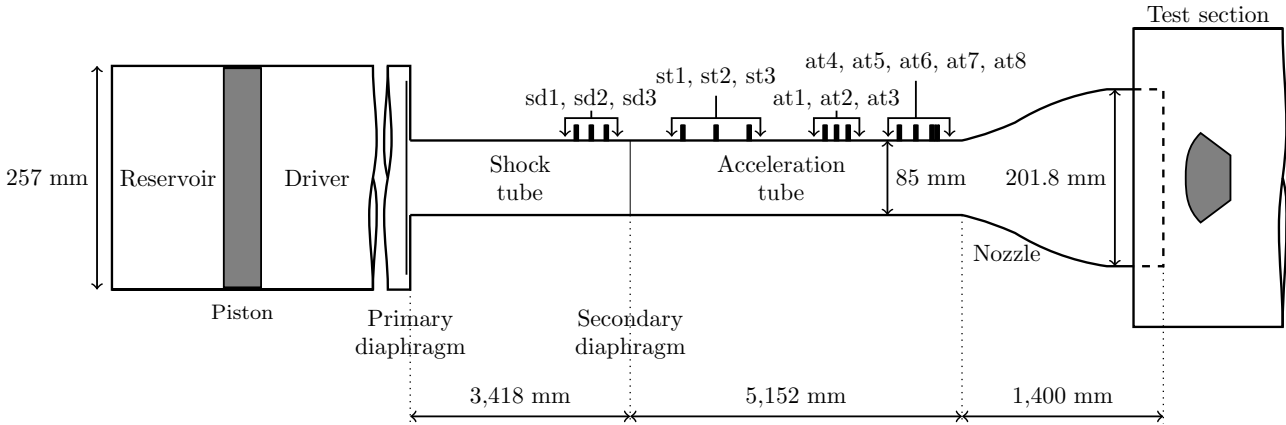


Figure 3.1: Schematic representation of X2. (James et al., 2018) [24]

pressure and temperature. The unsteadily expanded test gas will be steadily expanded in the nozzle, before flowing into the test section. This unsteady expansion feature enables expansion tubes to simulate aerodynamic flows around scaled models at very high enthalpies of up to 200 MJ/kg.

As is shown in Fig. 3.1, along the tube, there are 14 pressure sensors, three (sd1, sd2, and sd3) are mounted along the shock tube, and the rest are along the acceleration tube. In experiments, shock arrival times at the various pressure sensors are found automatically using Canny edge detection [78], and then shock speeds are calculated using the time of flight method between sensor locations [79]. The calculated shock speeds can be compared with theoretical predictions and simulations to check their validity.

The condition tested in this study [23] was designed to simulate a proposed Saturn entry trajectory at 26 km/s [25] by recreating its frozen post-shock temperature. The detailed information of this condition is shown in Table 3.1. This condition employs the most powerful driver condition for X2 (X2-LWP-2.5 mm-0) and a very low acceleration tube filling pressure (0.5 Pa) to achieve a very high enthalpy (170 MJ/kg) of the final test flow. The test gas is an 80%/20% helium/hydrogen (by volume) mixture, which has a higher amount of helium than in Saturn's atmosphere. A higher fraction of helium in the test gas leads to a higher specific heat for this helium/hydrogen mixture. This allows the post-shock temperature for the proposed Saturn entry trajectory at 26 km/s to be recreated in X2.

Table 3.1: Detailed information of the test condition.

Driver condition designation	X2-LWP-2.5 mm-0 [77]
Primary driver fill condition	77.2 kPa 100% helium (by volume)
Orifice plate diameter	65 mm
Primary diaphragm	1 x 2.5 mm thick cold rolled steel, scored diaphragm
Shock tube fill condition	2.0 kPa 80%/20% helium/hydrogen (by volume)
Secondary diaphragm	1 x $\approx 14 \mu\text{m}$ thick aluminum foil diaphragm
Acceleration tube fill condition	0.5 Pa air
Total enthalpy	170 MJ/kg

The flow properties generated by this condition were predicted by PITOT [24], an in-house flow condition simulation tool for expansion tubes based on compressible and isentropic flow relations, and are shown in Table 3.2. The PITOT prediction was performed in a fully theoretical mode where shock

speeds are found from fill pressures. This condition would generate the flow with a frozen post-shock temperature of around 25600 K, which approximately matches the frozen temperature prediction for the proposed Saturn entry (27600 K) [23]. This makes it possible to simulate the Saturn entry radiation based on the substitution theory from Stalker and Edwards [22].

PITOT can also calculate the freestream and post-shock flow properties based on the measured shock speeds. For this study, experimentally measured shock speeds and the PITOT calculation based on the experimental shock speed measurements are also listed in Table 3.2. The experimental measurements for all the experiments discussed in this paper are shown by mean and standard deviation ( $\sigma$ ) values. It can be seen that the nozzle exit pressure (freestream flow pressure) is around 100 times higher than the ambient pressure (acceleration tube fill pressure), so that the nozzle flow was under-expanded.

Table 3.2: Freestream and post-shock conditions predicted by PITOT and the values measured and calculated in experiments.

Shock Speeds	PITOT prediction	Mean measurements	$\sigma$
Shock tube, m/s	8440	8670	40
Acceleration tube, m/s	17970	18680	210
<hr/>			
Freestream flow			
Pressure, Pa	60	50	10
Temperature, K	380	400	30
Velocity, m/s	18200	18860	200
Mach number	15.5	15.6	0.7
Density, kg/m <sup>3</sup>	$6.3 \times 10^{-5}$	$5.9 \times 10^{-5}$	$0.7 \times 10^{-5}$
Species molar concentration	'H <sub>2</sub> ': 0.2, 'He': 0.8		
<hr/>			
Post-shock flow (frozen state)			
Pressure, Pa	16200	16200	1600
Density, kg/m <sup>3</sup>	$2.8 \times 10^{-4}$	$2.6 \times 10^{-4}$	$0.3 \times 10^{-4}$
Temperature, K	25600	27400	600
Velocity, m/s	4190	4340	40
<hr/>			
Post-shock flow (equilibrium state)			
Pressure, Pa	18400	18400	1800
Density, kg/m <sup>3</sup>	$5.0 \times 10^{-4}$	$4.8 \times 10^{-4}$	$0.5 \times 10^{-4}$
Temperature, K	12000	12300	100
Velocity, m/s	2310	2230	180
Species molar concentration	'e <sup>-</sup> ': 0.10, 'H': 0.20, 'He': 0.60, 'H <sup>+</sup> ': 0.10		

### 3.2.2 Numerical Comparisons

One dimensional post-shock relaxation calculations from the X2 condition predicted by PITOT and the target Saturn entry trajectory point ( $t = 206$  s) [25] were calculated using Poshax3 [80,81]. Poshax3 was developed for calculating one-dimensional, inviscid relaxation post-shock flow. The chemical reaction schemes implemented for giant planets entry include molecular hydrogen dissociation [39], ionization of hydrogen atoms, and ionization of helium [37]. Flow is assumed to be in thermal equilibrium and

with no radiative emission. Calculated post-shock properties are presented using the scaled binary reaction variable  $(1-r)\chi = (1-r) \int \frac{P}{V} ds$ , assuming that the H<sub>2</sub> mole fraction in the freestream flow is r. Here,  $\chi = \int \frac{P}{V} ds$  is the binary reaction variable derived from the Damköhler number  $D_a = Ps/V$ , which controls chemistry with respect to convective transport in the gas-phase [82]. P, V, and s represent local pressure, local velocity, and stream-wise distance respectively. (1-r) is used to compensate for the different mole fractions of H<sub>2</sub> and He in these two conditions. Detailed information of this scaling method will be discussed in Chapter 4.

The results are shown in Figs. 3.2 to 3.4 for the post-shock temperature and species mole fraction profiles generated by the X2 condition and the selected Saturn entry trajectory point. To have a better comparison of the non-equilibrium process at these two cases, 10 mm downstream of the shock, which is an approximate maximum shock standoff distance that can be generated with test models in X2, was marked in the figures. Qualitative agreement was found in the non-equilibrium processes generated by these two conditions. Dissociation occurs post-shock, and electrons produced by ionization slowly build up along the streamline within 10 mm downstream of the shock front. Dissociation will be complete within 10 mm after the shock at the proposed Saturn entry condition, while in X2 condition, dissociation will terminate earlier. Due to the difference in hydrogen mole fraction and post-shock pressure, these non-equilibrium processes do not show quantitative agreement as they do not equilibrate to the same state. As would be expected, helium mainly acts as an inert gas in these conditions, as the mole fraction of He<sup>+</sup> is negligible during relaxation and in the equilibrium state. Overall, these numerically show that non-equilibrium processes in shock layers at the selected Saturn entry trajectory point can be qualitatively simulated in X2, while temperature for Saturn entry is duplicated in this X2 condition.

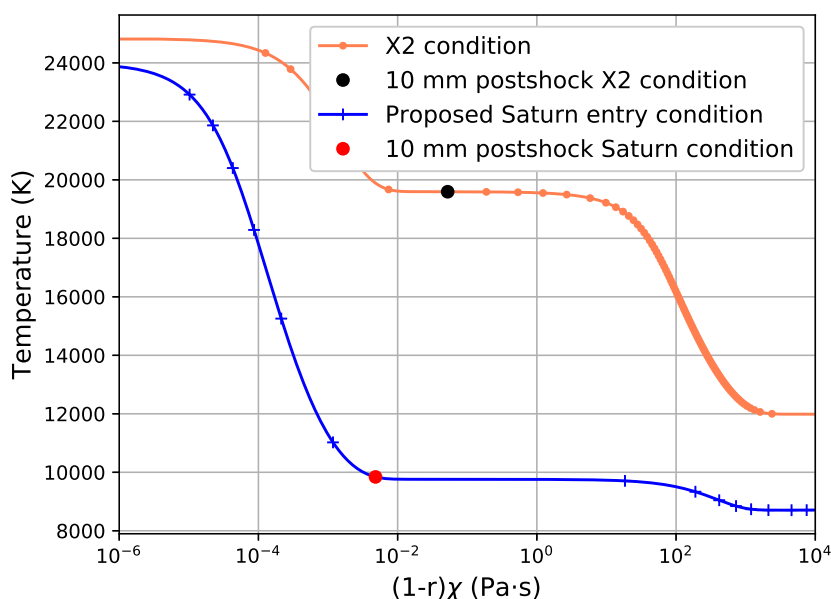


Figure 3.2: Post-shock temperature profiles generated by X2 condition and at the proposed Saturn entry trajectory point.

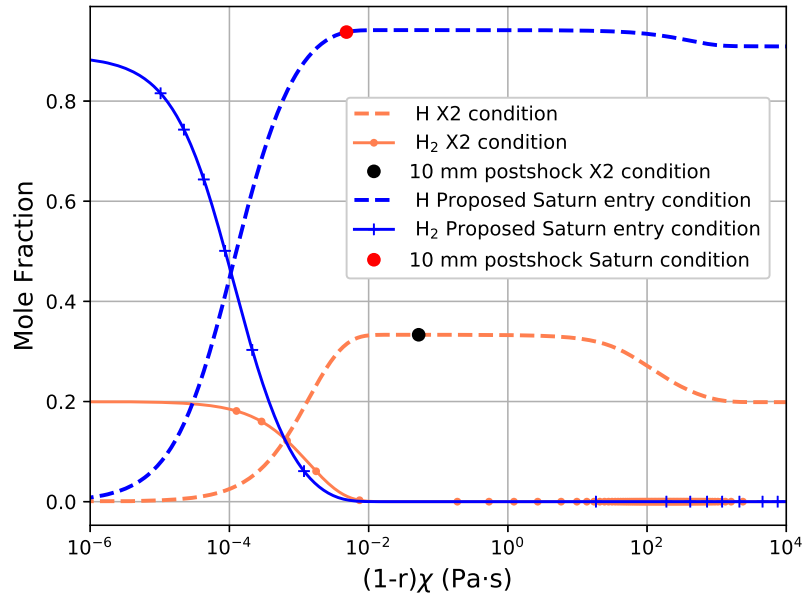


Figure 3.3: Post-shock H and  $\text{H}_2$  mole fraction profiles generated by X2 condition and at the proposed Saturn entry trajectory point.

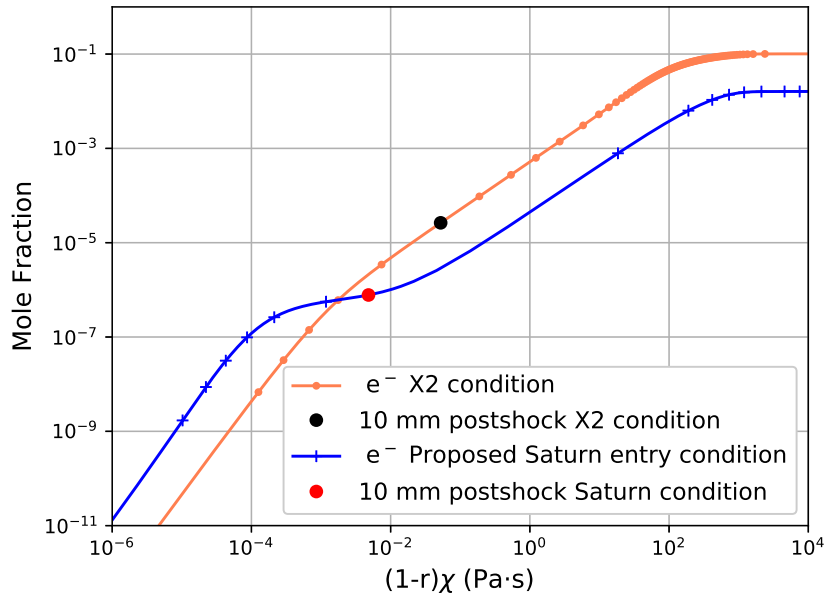


Figure 3.4: Post-shock electron mole fraction profiles generated by X2 condition and at the proposed Saturn entry trajectory point.

### 3.2.3 Optical Measurements and Test Model

The test model was a truncated sphere, the size of which was chosen to fit within the core flow while keeping the shock standoff as large as possible. The radius of curvature of the equivalent sphere is 70.7 mm, with the sphere being truncated at  $\pm 45^\circ$  from the centerline, thus giving a total model diameter of 100 mm, and decoupling the after-body flow from the shock layer as the flow becomes supersonic at the corner according to the preliminary flow simulations. A schematic of the model and its size

is shown in Fig. 3.5. This simple, axisymmetric model shape is ideal for code validation purposes, because it's easy to generate a CFD grid over this shape, and then CFD/radiation simulations can be performed over it at reasonable computational expense.

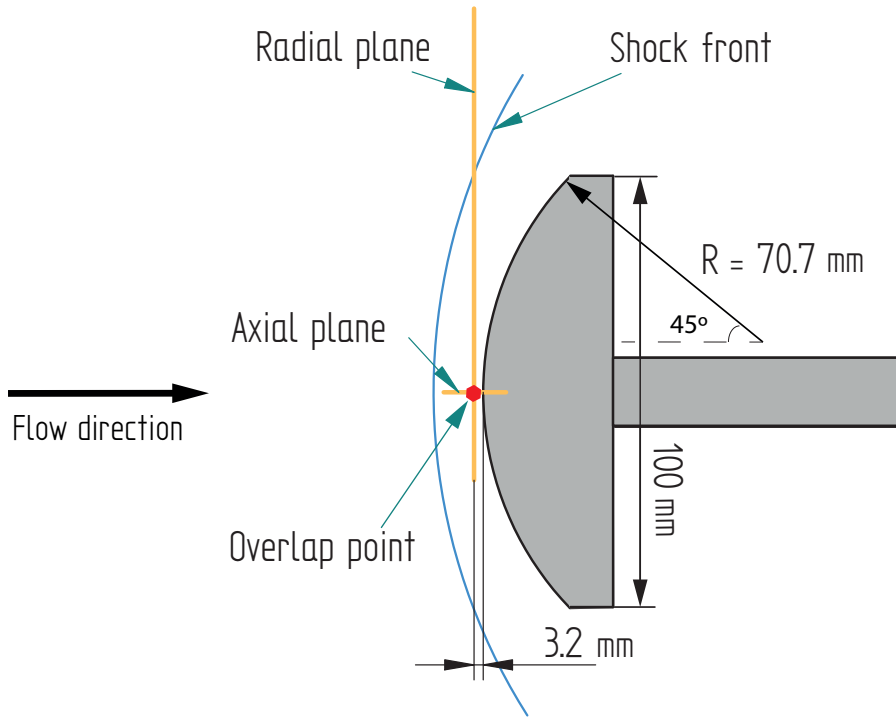


Figure 3.5: A schematic of the test model. Axial and radial object plane locations, and their overlap point are also shown.

Spectroscopic measurements were conducted in two orientations. Measurements in several experiments were conducted with the slit of the spectrometer aligned with an axial plane that includes the stagnation streamline to image the axial radiation. In other experiments, the slit of the spectrometer was aligned with a radial plane perpendicular to the stagnation line, to obtain the radiation radially. Figure 3.5 demonstrates the chosen axial and radial planes. The intersection of these two planes is noted as the overlap point, where axial and radial measurements should give the same radiance.

The spectroscopic set-up for both orientations is shown in Fig. 3.6. An optical emission spectroscopy (OES) system including an imaging spectrometer with a camera sensitive in the visible and near-infrared wavelength range, and supporting optics, are shown. In this figure, optical configurations of the spectroscopic system in each orientation are presented on each side of the test section. In the actual experiments, only the set-up in one orientation was selected for each experiment, and a Shimadzu HPV-1 high speed camera was set up on the other side of the test section to record the H- $\alpha$  filtered radiative emission.

The high speed camera can record 100 gray-scale images per trigger. The recording frequency in this study was 500 kHz, giving a  $200 \mu\text{s}$  total recording time, to observe the entire flow development in each experiment. An Andover corporation H- $\alpha$  filter 656FSX10-50 was used on this side to enable the camera to capture the radiance from the specific center wavelength (656 nm) with full width at half maximum (FWHM) ( $\pm 20 \text{ nm}$ ), so that the time-resolved H- $\alpha$  radiation can be measured.

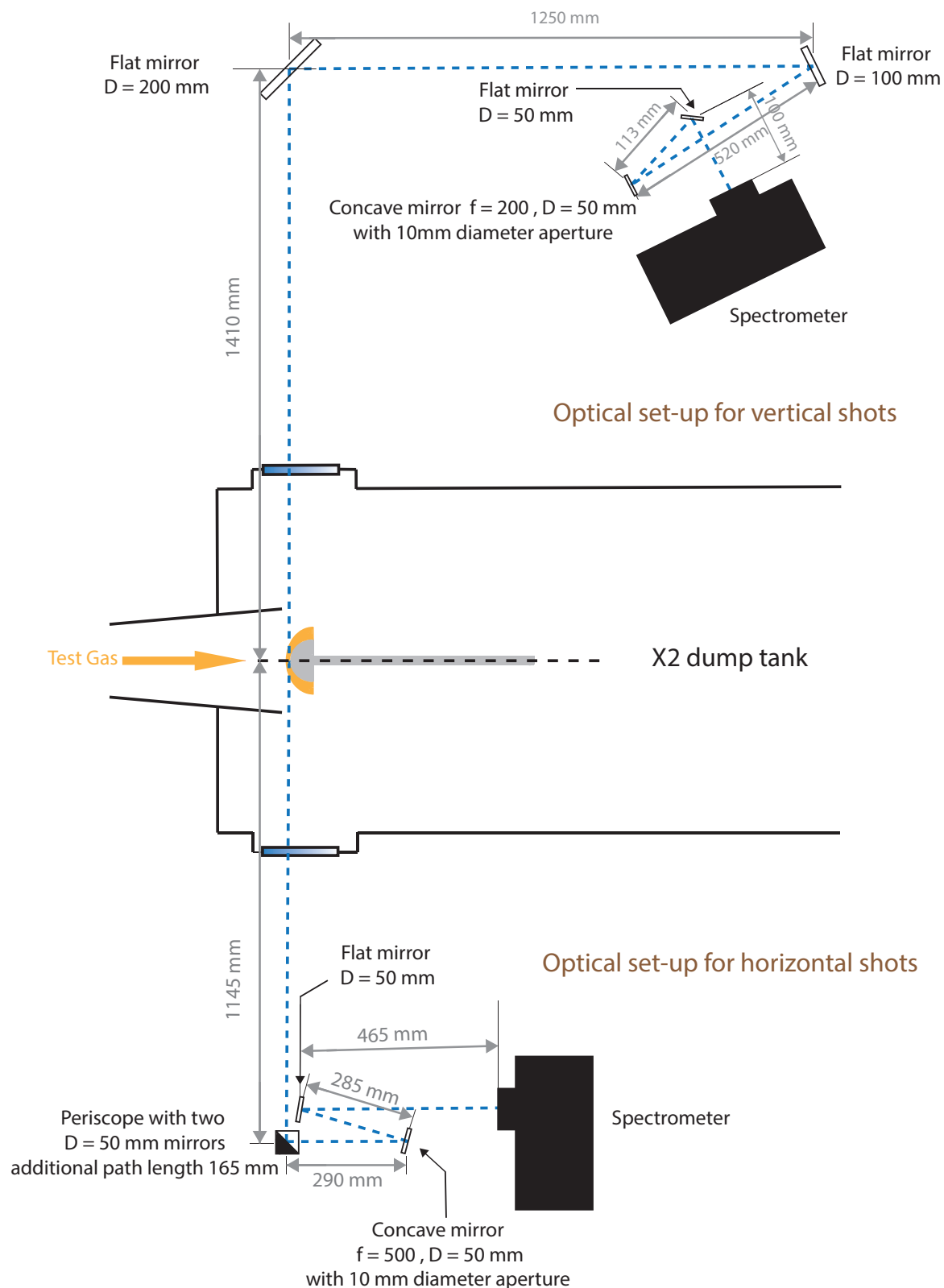


Figure 3.6: Schematic of the optical arrangement for axial and radial experiments (not to scale).

### 3.3 Condition Characterization Experiments

The condition characterization experiments were used to study the core flow size and establishment time of the test flow for the designed condition. A pitot rake was installed vertically in the test section and aligned with the centerline of the nozzle. Nine pitot pressure probes were mounted on the rake and

radially spaced at 17.5 mm intervals. The center probe (pt5) was on the centerline of the nozzle. A figure that shows the scale of the rake with the nozzle and its axial location can be found in Fig. B.3.

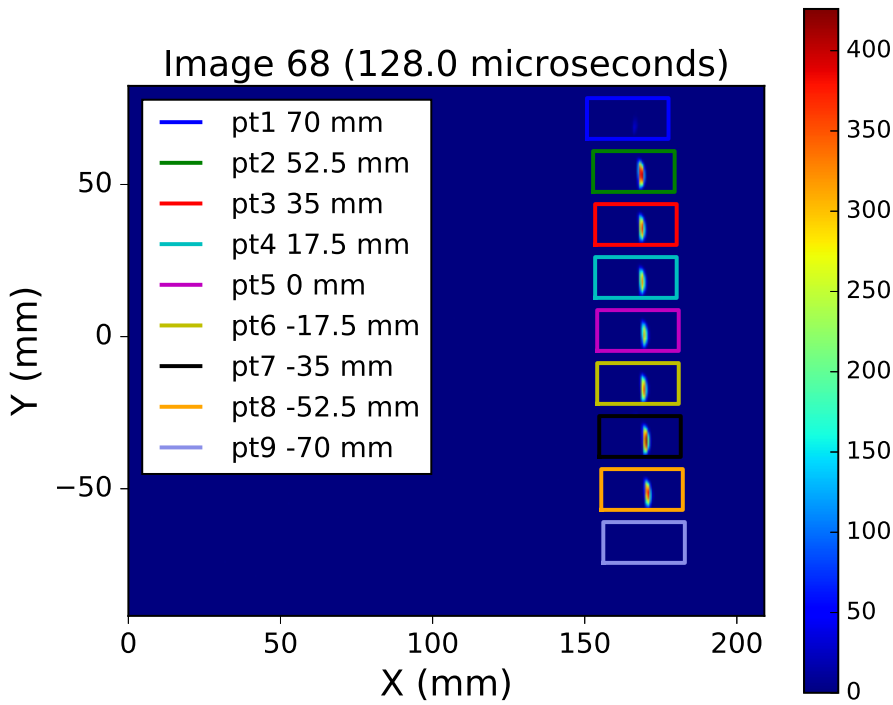


Figure 3.7: H- $\alpha$  filtered radiation from shock layer over pitot probes, labels show the actual probe heights relative to the centerline.

H- $\alpha$  filtered high speed images were obtained to observe time-resolved radiative emission in the shock layer of each probe. A sample image during the test time is shown in Fig. 3.7. A box around each probe that includes the whole shock layer region was selected as shown, and the intensity was spatially integrated to explore the time-resolved radiation at different radial locations. The time-resolved intensities, as well as the time-resolved pitot pressure measurements, are shown in Fig. 3.8. Test time was estimated from both time-resolved pressure and emission measurements. From the time-resolved pressure measured for probes from pt2 to pt8, there is an initial increase in pressure as the flow establishes. Then, the pressure is steady from 87 to 132  $\mu$ s. This refers to the period when fully processed test gas arrives test section. After 132  $\mu$ s, the pressure increases again due to the unsteady expansion arrives. Thus, the test time based on pressure measurements is around 87–132  $\mu$ s. For the time-resolved radiative emission, because large integration regions are used, the shock shape change can be detected and reflected by emission change. Before the test time begins, there will be a spike in recorded emission due to shock establishment [79]. Based on this, it was found that emission over probes from pt2 to pt8 keeps the same trend between 105 and 160  $\mu$ s, which is probably the test time. Combining the two measurements, the test time is therefore from 105 to 132  $\mu$ s. For each experiment, the OES system was set to expose within the test time, to measure the radiation when test flow has been established on the spheric model.

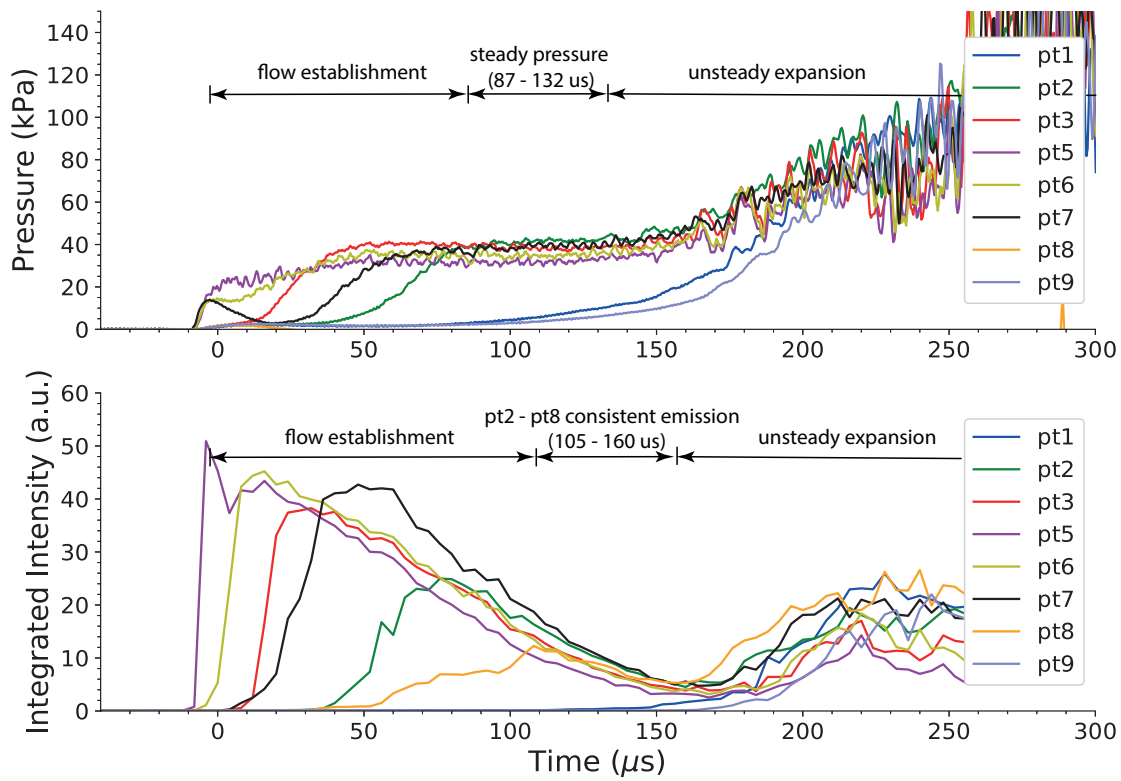


Figure 3.8: Time-resolved pitot pressure and integrated emission over each pitot probe (pt4 data not shown due to connection failure).

The pressure and radiation measured by probes pt1 and pt9 were at a much lower level than measured on other probes, showing that these two probes are beyond the core flow. The core flow generated by this condition was within a circular region between pt2 and pt8, giving the diameter to be around 105 mm, which fits the size of the model well.

## 3.4 Blunt Body Experiments

### 3.4.1 High Speed Images

Sample H- $\alpha$  high speed filtered images of the flow over the test model are shown in Fig. 3.9. Two images are shown from separate experiments, in which different focal lengths of the camera were chosen. Figure 3.9b was obtained by zooming the camera into the top half of the flow, which provides radiation data with a better spatial resolution and is more suitable for comparison with numerical calculations. The intensity has been digitally scaled in order to clearly show the bow shock. Canny edge detection [78, 79] was employed to identify the model edge and the shock front. The black curve shows the fitted model edge, and the blue curve shows the fitted shock front. Figures 3.9a and 3.9b show highly non-equilibrium radiative flows, with low luminosity in the immediate post-shock region, and a significant emission level increase near the body.

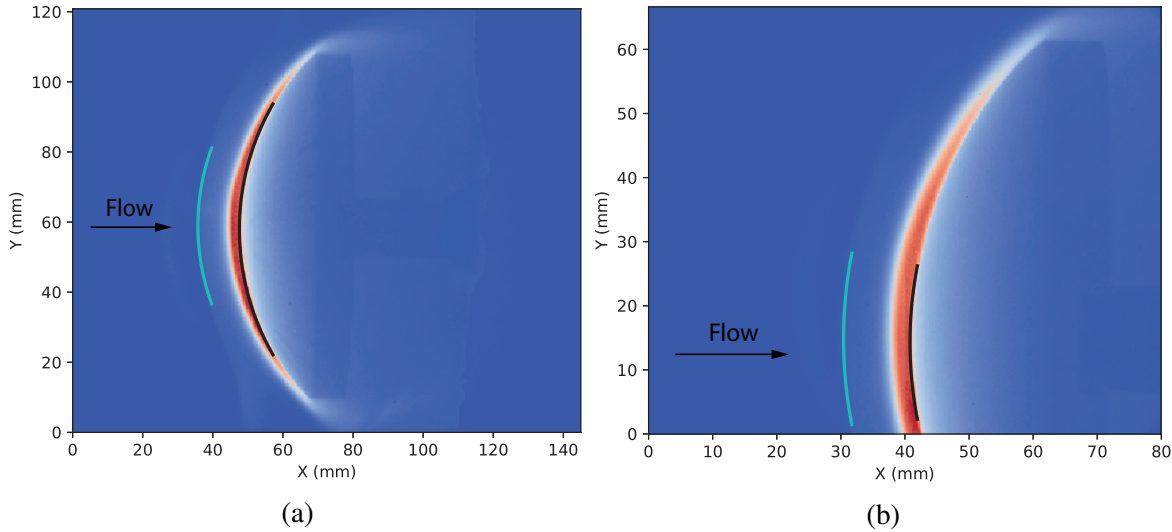


Figure 3.9: Radiative shock layers filtered by a H-alpha narrow bandpass filter in the test time, with different camera focal lengths chosen.

Time-resolved shock standoff distances with the uncertainty were obtained from all useful experiments in this study, and are shown in Fig. 3.10. In the exposure time of OES system (between  $105 \mu\text{s}$  and  $125 \mu\text{s}$ ), the shock standoff distances in all experiments agree well and remain steady at around  $11.7 \text{ mm}$ .

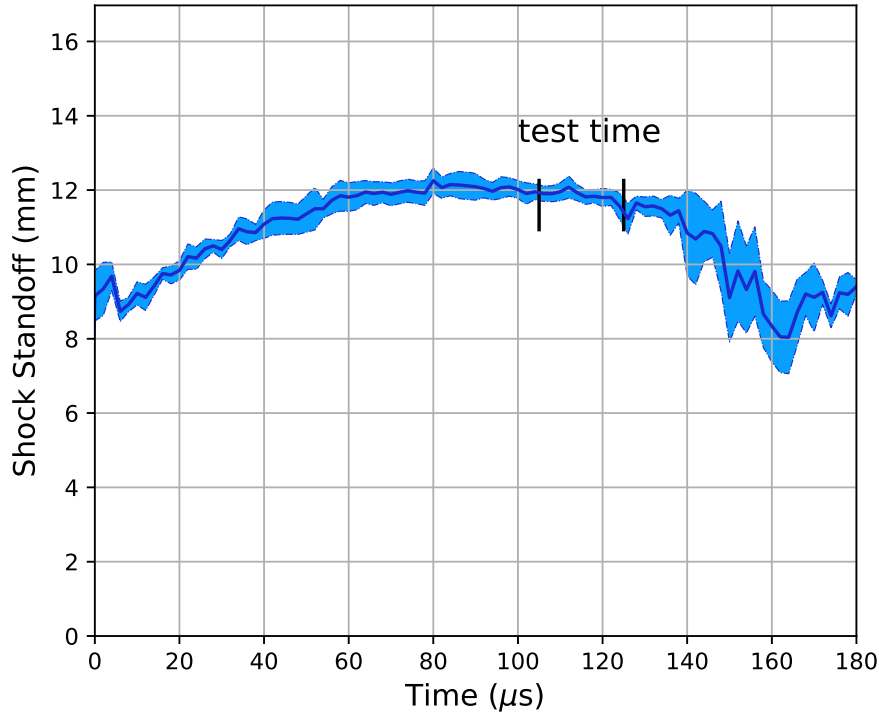


Figure 3.10: Time-resolved shock standoff distances with the uncertainty.

To study how the recorded H- $\alpha$  emission in the shock layer changes over time, various regions in the flow were selected, as shown in Fig. 3.11a, and the integrated emissions in these regions were calculated. The integrated emissions, along with the scaling factors, are shown in Fig. 3.11b. The intensities in all the selected regions drop during the test time, but the decrease is less pronounced for

the region near the stagnation streamline (region 4). This phenomenon was also observed in previous studies [79, 83] in earth re-entry conditions. One possible cause could be contaminants, such as iron, which can affect the non-equilibrium processes during the test time.

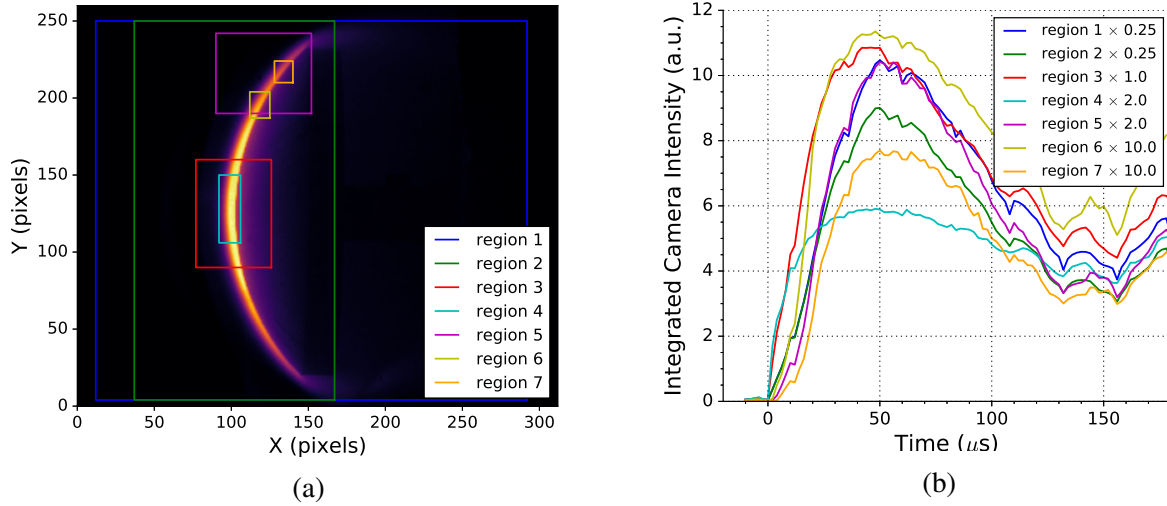


Figure 3.11: Regions chosen in H- $\alpha$  filtered radiative field and the time-resolved spatially integrated intensities in these regions.

### 3.4.2 Spectroscopic Results

Spectroscopic results from five experiments with the test model are presented in this chapter. The spectroscopic system settings for each experiment are shown in Table 3.3. Here, in three experiments the spectrometer was focused on the axial plane that includes the stagnation streamline, while in another two experiment the spectrometer was focused on the chosen radial plane, which is 3.2 mm upstream of the model edge (shown in Fig. 3.5). A coarse grating (150 gpmm) was used to obtain spectra with a wavelength range of around 400 nm - 690 nm, so that the most of the Balmer series lines can be observed. H- $\alpha$  measurements with a higher resolution were achieved by using a finer grating (600 gpmm), which allows the observation over the wavelength region from around 600 nm to 700 nm. The absolute intensity values of the spectra from both axial and radial experiments were calibrated with an integrating sphere, employing the method discussed by Lewis et al. [84].

Table 3.3: Spectroscopic setting in each experiment.

Experiment number	Grating gpmm	Center wavelength nm	Direction
x2s3691	150	525	Axial
x2s3692	600	657	Axial
x2s3693 (repeat)	600	657	Axial
x2s3695	600	657	Radial
x2s3696 (repeat)	600	657	Radial

### Axial Experiments

Figure 3.12 shows the spatially resolved spectra from the axial experiments using coarse (150 gpmm) and fine (600 gpmm) gratings, with the spatial resolution measured along the stagnation streamline. Radiance is presented spatially along the vertical axis, while the horizontal axis refers to the wavelength of diffracted radiation. The flow direction is from bottom to top, and the estimated model edge has been set to 0 mm on the vertical axis. The spectrometer was set to measure the shock layer radiation in the region within 10 mm upstream of the model edge, so that the shock front, which is around 11.7 mm away from the model edge, is beyond the measured region. Figure 3.12a shows an image with the coarser grating, containing features of H- $\alpha$  (656 nm), H- $\beta$  (486 nm), H- $\gamma$  (434 nm), and singly ionized aluminum (Al $^+$ ) (624 nm and 466 nm), while Fig. 3.12b demonstrates the H- $\alpha$  spectral line captured by the finer grating.

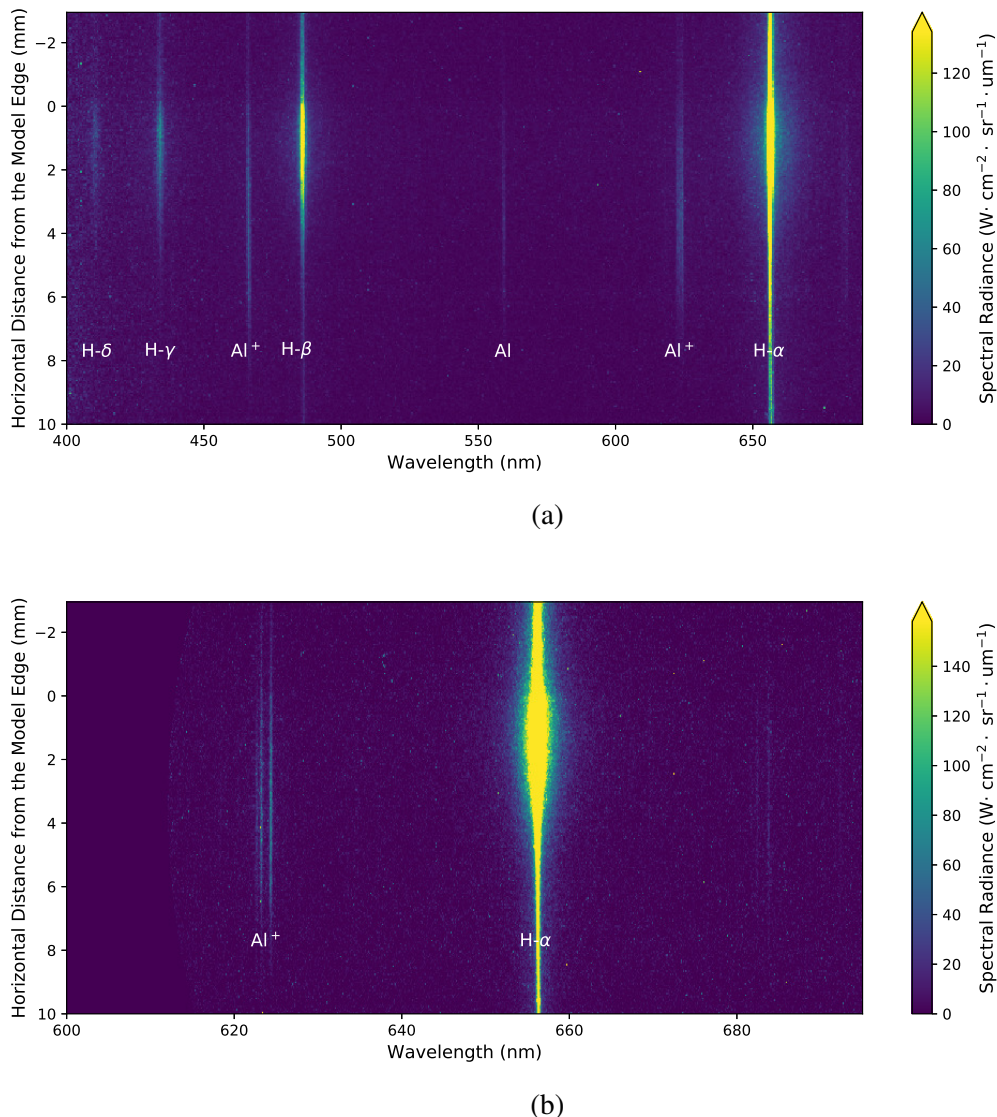


Figure 3.12: Spectra from axial experiments, (a): with coarse (150 gpmm) grating, (b): with fine (600 gpmm) grating.

By integrating the spectral radiance under the selected spectral line, the radiance emitted from a

specific transition can be obtained. Figure 3.13a shows the integrated H- $\alpha$  and H- $\beta$  radiance profiles from three axial experiments. As the measured spectral lines have finite linewidths, appropriate wavelength ranges were selected to calculate radiances. The H- $\alpha$  radiance was integrated between 640 nm and 670 nm, and H- $\beta$  radiance was integrated between 476 nm and 497 nm.

The radiation was measured by looking through optical depths along the line-of-sight. As the spectrometer was looking through a bow shock, the optical lengths for each observation point along the stagnation streamline were different. As the first order analysis, the radiance profiles were normalized by optical depths along the line-of-sight extracted from high speed images, and are shown in Fig. 3.13b. This approximation enables the compensation for the line-of-sight lengths difference, but ignores self-absorption and the non-uniformity of flow. Along the axial plane, normalized H- $\alpha$  radiance profiles match well between experiments using different gratings. In the region upstream of 6 mm, the H- $\alpha$  radiance profiles are relatively flat, then they have significant increases downstream of 6 mm, which could be due to the further development of non-equilibrium process. In the region near the stagnation point, the velocity along the stagnation streamline will get close to zero, thus allowing more time for the flow relaxation. The flat H- $\alpha$  radiance profiles before 6 mm conform with the steady H- $\alpha$  radiance following the non-equilibrium peak in EASTs Saturn tests between 25 and 27 km/s [20]. In the repeat experiment with the fine grating, the H- $\alpha$  radiance is higher than the results from the other two experiments, while the shock speeds and shock standoff distances repeat well among these three axial experiments. This is possibly due to the shot-to-shot variation driven by contamination variation, as the tunnel in this experiment may not be cleaned as well as other experiments.

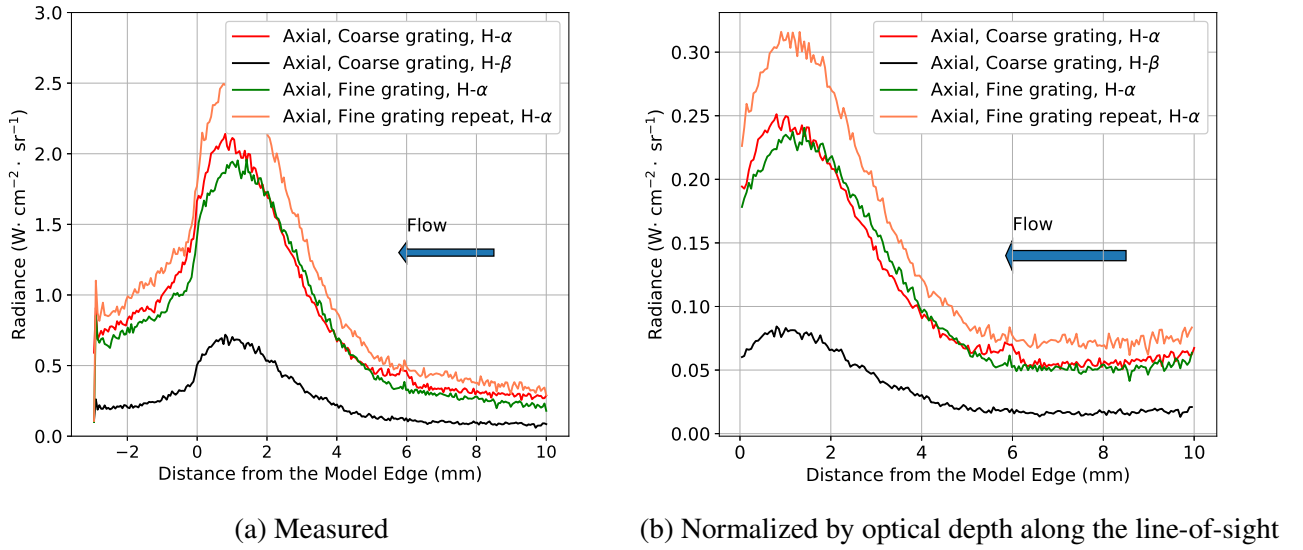


Figure 3.13: H- $\alpha$  and H- $\beta$  radiance profiles from axial experiments.

To have a better idea of the spectra at different locations. Spectral widths of H- $\alpha$  along the axial plane in the fine grating experiment were extracted by fitting the spectral lines with Voigt profiles. The obtained FWHM data are shown in Fig. 3.14. In the region 8 mm upstream of the model edge, the H- $\alpha$  line width is small, while within 8.0 mm, H- $\alpha$  line becomes much more broadened. Broadened spectral lines can be generated by various types of spectral line broadening effects, including instrument

function, Doppler broadening, natural broadening, and Stark broadening [85]. The instrument function and natural broadening effects are constants and will not account for the linewidth change. Doppler broadening, which is a function of translational temperature [85], is expected to decrease along streamlines due to chemical reactions as they absorb energy. The FWHM due to Doppler broadening can be calculated by [85]:

$$\Delta f_{Doppler} = 7.16 \times 10^{-7} \lambda_0 \sqrt{\frac{T_{Tra}}{M}} \text{ (nm)} \quad (3.1)$$

Here,  $\lambda_0$  is the center wavelength of the transition,  $T_{Tra}$  is the translational temperature, and  $M$  is the molecular weight. For H- $\alpha$ , the FWHM is:

$$\Delta f_{Doppler} = 4.7 \times 10^{-4} \sqrt{T_{Tra}} \text{ (nm)} \quad (3.2)$$

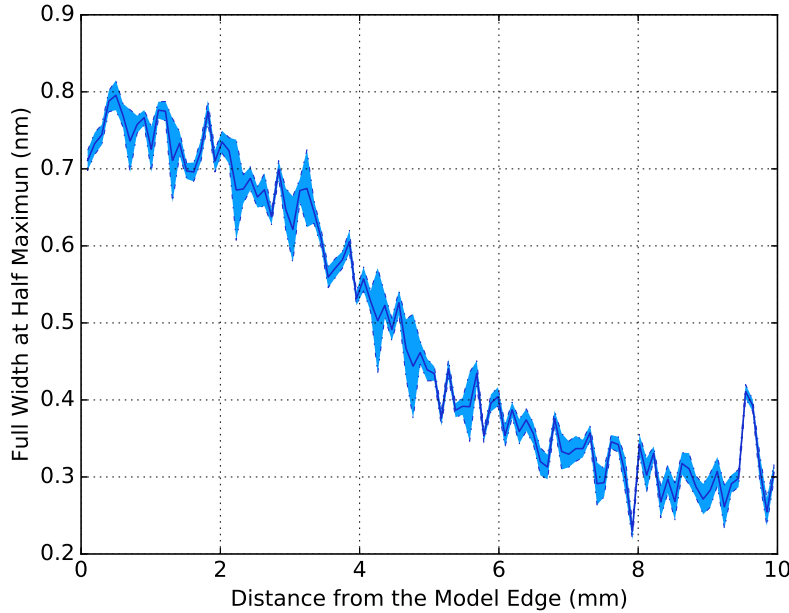


Figure 3.14: Linewidths of H- $\alpha$  along the axial plane for the experiment with the fine grating.

As the shock layer in this study is in the non-equilibrium state, temperatures in the shock layer are between frozen and equilibrium states temperatures, which are from 27400 to 12300 K. This leads to the Doppler broadening FWHM in this non-equilibrium shock layer to be between 0.078 nm and 0.052 nm, which is a small contribution compared to the measured FWHM.

Hence, this increased broadening effect within 8 mm along the axial plane is more likely to be explained by Stark broadening (which is caused by the presence of electrons [85], and implies ionization in the flow), or self-absorption.

## Radial Experiments

In the radial experiments, a radial plane perpendicular to the stagnation streamline and 3.2 mm upstream of the model edge was selected, and the radiation was measured by looking through the plane.

As the flow field is axisymmetric, only the radiation along the top half of the radial plane was captured to show the radiation distribution. Figure 3.15 shows the data collected from the radial experiment. The peak radiance occurs at the stagnation streamline, which was marked as 0 mm on the location axis. The H- $\alpha$  (656 nm) and the Al $^+$  spectral line (624 nm) are visible with this grating.

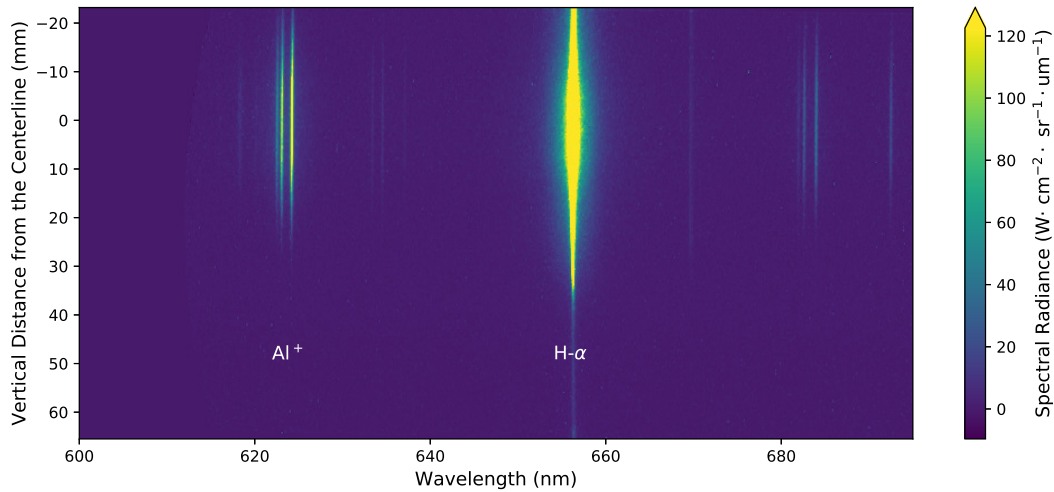


Figure 3.15: Spectrum data from the radial experiment (with fine (600 gpmm) grating).

A H- $\alpha$  radiance profile was obtained by integrating the intensity under the spectral line and is shown in Fig. 3.16. This profile is presented spatially on the vertical axis.

The spectra at the overlap point between the axial and radial experiments with the same grating were plotted together in Fig. 3.17. Matches on the spectral lines can be observed, with small discrepancies in the absolute spectral radiance values and the linewidths. Also, the radiance in the radial experiment at the overlap point is about  $1 \text{ W} \cdot \text{cm}^{-2} \cdot \text{sr}^{-1}$  (at 0 mm in Fig. 3.16), which matches the radiance at the overlap point from axial experiments (at 3.2 mm in Fig. 3.13). This indicates that the radial experimental measurements roughly match with those from axial experiments as would be expected, and confirms the intensity calibration accuracy for the two orientations experiments.

### 3.4.3 Contamination

In section 3.4.2, the H- $\alpha$  radiance in the repeat axial experiment with fine grating was found to be higher than that from the other two axial experiments (see Fig. 3.13), while the shock speeds and the shock standoff distances were statistically the same. This shot-to-shot variation could be attributed to many reasons, such as the impact of contamination from air or the aluminum diaphragm. In this part, the aluminum contaminant, which comes from the aluminum secondary diaphragm, will be discussed. With such a light test gas (molecular weight = 3.6 g/mol), heavy contaminant particles such as aluminum (molecular weight = 27 g/mol) can play an important role in collisions, thus accelerating the non-equilibrium processes. Also, aluminum itself can ionize and generate electrons, which are the main catalyst for electron impact ionization [45], and may accelerate this process.

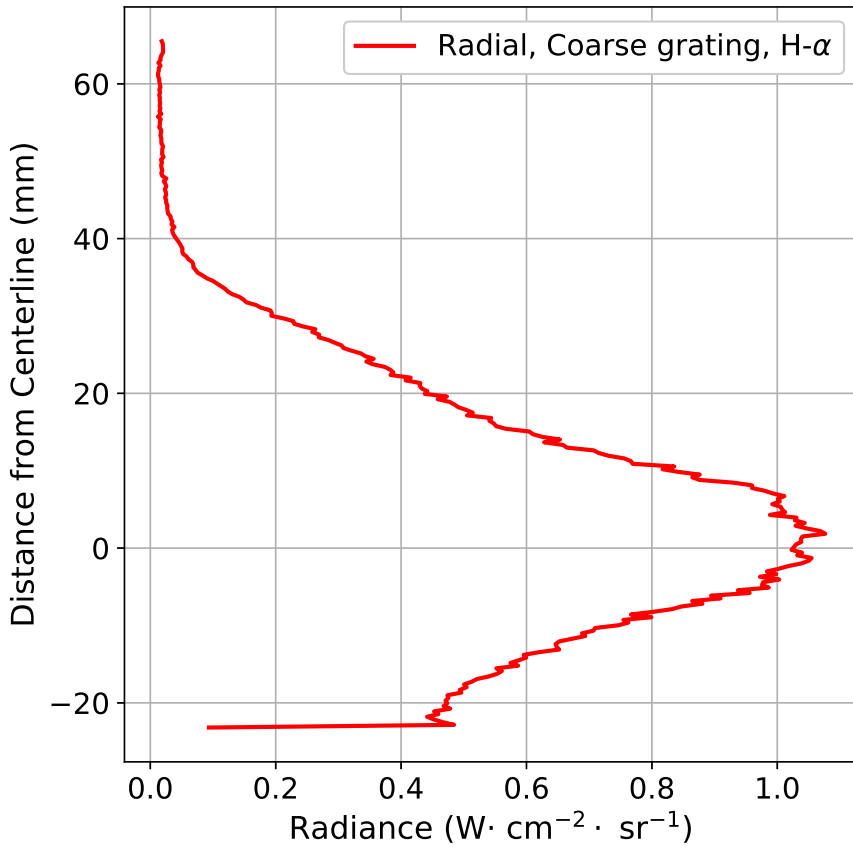


Figure 3.16: H- $\alpha$  radiance profile from the radial experiment, along the radial plane 3.2 mm upstream of the model edge.

In the thesis of Kelly [86], number density of Aluminium contaminants in his X2 Argon experiments was estimated by fitting the measured spectral lines with numerical predictions using his own code. Aluminium relative number density was estimated as  $(3.5\text{-}6.0)\times 10^{-7}$  if the relative number density of Argon was set as 1. Number density of Argon at the post-shock frozen state in Kelly's condition was around  $3.69 \text{ mol/m}^3$ , so that the Aluminium number density was around  $(1.3\text{-}2.2)\times 10^{-6} \text{ mol/m}^3$ . The Aluminium number density in the experiments of Kelly [86] and in this thesis would be similar as same Aluminium diaphragms and the same facility were used. For this helium condition in this thesis, the H<sub>2</sub> number density was around  $0.016 \text{ mol/m}^3$ , which is four orders of magnitude higher than the Aluminium contaminants.

To understand how aluminum contamination affects the radiation, H- $\alpha$  and Al<sup>+</sup> (624 nm) radiance profiles from axial experiments are plotted in Fig. 3.18. The Al<sup>+</sup> radiance was integrated from the radiation in 620 nm - 628 nm. They have been scaled by a factor of 10 for a better comparison with H- $\alpha$  radiance, and as such, appear noisier.

In Fig. 3.18, it was found that the repeat experiment, where the H- $\alpha$  radiance is higher than that from the other two experiments, has a higher level of Al<sup>+</sup> radiance. This indicates that even with repeatable pre-shock flow conditions, the level of aluminum contaminant can be different due to various tunnel cleanliness in each experiment [87]. This may be a cause of the stronger Balmer radiation in the repeat experiment.

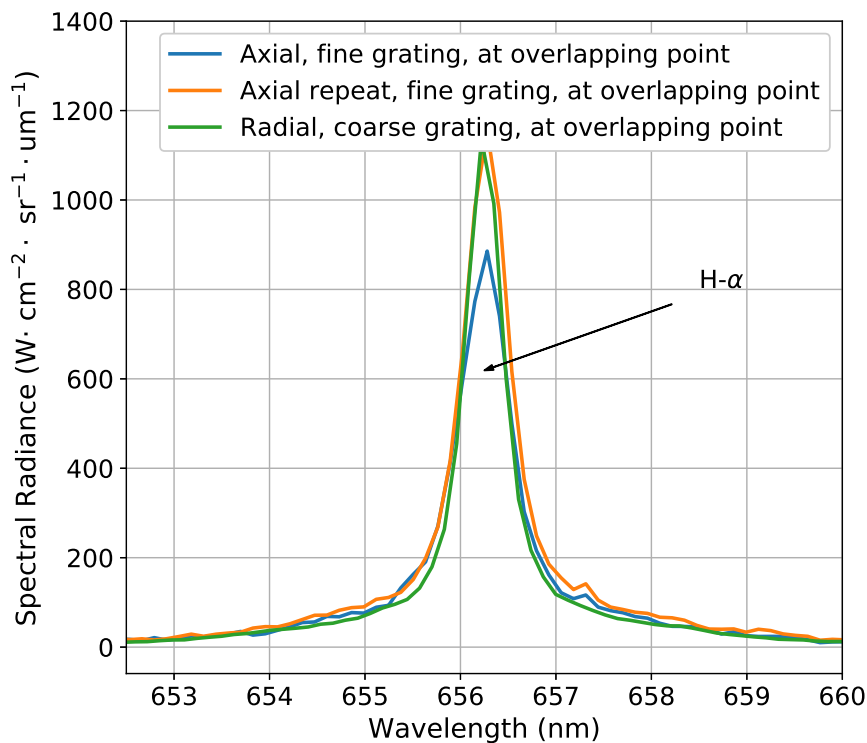


Figure 3.17: Comparison of H- $\alpha$  spectral lines at the overlap point (3.2 mm upstream of the model edge) from axial and radial experiments.

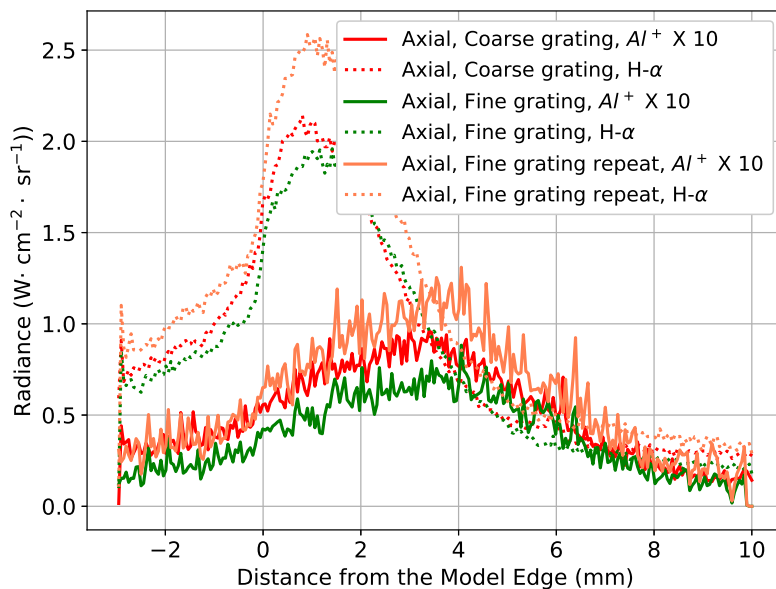


Figure 3.18: Radiance profiles of  $\text{Al}^+$  and  $\text{H}-\alpha$  lines from axial experiments, with  $\text{Al}^+$  radiances being scaled by 10.

In this region, aluminum can act as a heavy particle collision partner, which could result in a higher level of  $\text{H}-\alpha$  radiance in the repeat experiment. In the region downstream of 8 mm, the  $\text{Al}^+$  radiance begins to increase. Each  $\text{Al}^+$  ion releases an electron when it is formed, which adds to the electron population, subsequently increasing the rate of  $\text{H}^+$  formation from  $\text{e}^-$ - $\text{H}$  collisions. The increase in

electron number density is also shown in the H- $\alpha$  FWHM profile in Fig. 3.13b. The impact that higher levels of aluminum particles have on the collisions and non-equilibrium processes can be a possible cause of higher H- $\alpha$  radiances. The decrease of Al $^+$  radiance downstream of 4 mm could be due to the further ionization of Al $^+$ .

## 3.5 Abel Inversion of Experimental Data

The measured spectra from the axial experiments are the values integrated by the optical depth along the line-of-sight along the axial plane that includes the stagnation streamline. The spectra from the radial plane enable us to look at the radial distribution through the axisymmetric flow (shown in Fig. 3.5). In this study, the radiances from the radial plane and the axial plane coincide with each other at the overlap point, which is 3.2 mm upstream of the model edge. For axial experiments, the data give the axial distribution through the whole line-of-sight and can not be properly deconvolved to give accurate information about local radiation. Measured radiances in radial experiments are integrated values along the line-of-sight from the radial plane, in which the regions of uniform intensity are circularly symmetric. Thus, the integrated radiation from radial experiments can be Abel inverted [88] to obtain the radial distribution of the local radiance, with the assumption of no self-absorption. It is uncertain whether the H- $\alpha$  radiation measurements with this spherical model was optically thin or not. However, H- $\alpha$  radiation measurements using this condition but with a cylindrical model in Chapter 4 (Fig. 5.7a) showed that with the line-of-sight lengths of 75 mm and 100 mm, there was no significant self-absorption except for the region near the model. For the current study, as the shock was axisymmetric, most line-of-sights of the radiation measurements were smaller than 100 mm. Additionally, with the spherical model, the measured radiance were integrated values through a non-uniform flow, so with the same line-of-sight and same location after the shock, the self-absorption would be less than that with a cylindrical model. Therefore, the radiation measurements in this section were at least optically thin near the shock front. However, the self-absorption which may exist will lead to the under-estimation of the Abel inverted radiance value. In this section, the discussions assumed that the radiation measurements had negligible self-absorption.

Figure 3.19 shows the measured H- $\alpha$  and Al $^+$  radiances (Fig. 3.19a) from the radial experiment, and the Abel inverted radiance profiles (Fig. 3.19b). Al $^+$  radiance profiles have been scaled by 10 for a better comparison with H- $\alpha$  radiance data. Because Abel inversion only requires the data from the shock edge to the centerline, only the radiance profiles on the top half of the flow field are shown here.

From the inverted radiance profiles, some hidden features can be seen more clearly. In Fig. 3.19b, the region from the shock edge (at 40 mm) to the overlap point with the stagnation streamline (at 0 mm) can be divided into three broad regions: 1. In the region near the shock, the intensity of the H- $\alpha$  radiation is relatively low and gets higher when closer to the second region. 2. The H- $\alpha$  radiance is approximately constant. 3. The H- $\alpha$  radiation gets stronger near the overlap point. These three regions for this radial experiment were marked in Fig. 3.19b. The flow in these three regions can be representative of the flow in different non-equilibrium stages along the stagnation streamline, which

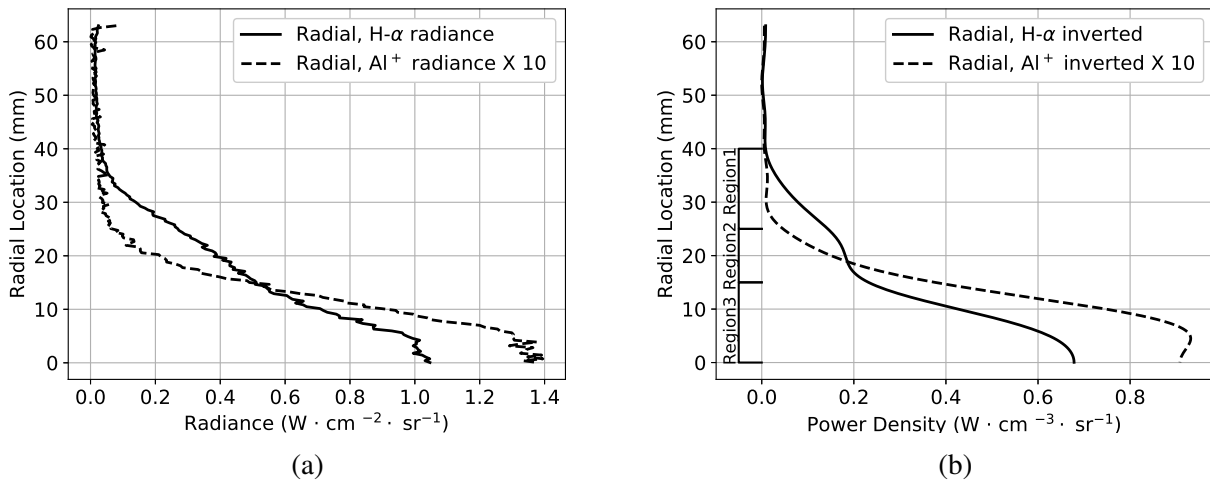


Figure 3.19: (a): Measured H- $\alpha$  and Al $^+$  radiance profiles, (b): Abel inverted results, from the radial experiment.

have been discussed in Introduction. The first region displays the flow immediately behind the shock, the second region represents the flow further downstream of the shock front along the streamlines, and region 3 shows the flow close to the overlap point. This increase-steady-increase characterization in H- $\alpha$  radiance profile was also seen in stagnation streamline radiation measurements, when this condition was tested using a quasi two-dimensional cylinder model, in which flow is nominally two-dimensional [7].

Region 1 for this experiment is from around 40 mm to 25 mm. The inverted Al $^+$  radiance in this region is negligible, while H- $\alpha$  emission can be seen. In this immediate post-shock region, as the time allowed for chemical reactions is limited, the potential for hydrogen ionization can be relatively low.

Region 2 demonstrates the area in between region 1 and region 3. The Al $^+$  becomes visible in this region, showing the ionization of Al, and implying more potential of H ionization. In this region, hydrogen ionization could be mainly caused by heavy particle collisions, which is a slow mechanism for hydrogen ionization, as the electron number density is not high enough to fully initiate the main ionization mechanism (e $^-$ -H collision). Thus, ionization is slow in this region, and the H- $\alpha$  radiance is approximately constant. For this experiment, the region is from 25 mm to 15 mm.

Region 3 in this experiment is from around 15 mm to the overlap point. Here, H- $\alpha$  emission is higher, and the radiance reaches the peak near the overlap point. This strong emission could be attributed to the second stage of hydrogen ionization, which is caused by e $^-$ -H collisions. As the electrons accumulate with the reactions along the streamlines after the shock, the electron number density may become considerable in this region. This could be due to the relaxation development or the boundary layer effects where the flow slows down and can have more time to relax further. If so, this will make e $^-$ -H collisions a superior mechanism, and electronic temperature increases due to elastic energy transfer rate becoming higher than inelastic energy transfer rate. These can lead to the rapid ionization and the strong H- $\alpha$  emissions.

The spectral radiances from this experiment were also Abel inverted, so that the spectral radiance

at each local point along the radial direction were obtained. Then the spectral line shape was analyzed to get the FWHM, shown in Fig. 3.20. As has been discussed in section 3.4.2, increased broadening for this condition is dominated by a stronger Stark effect, caused by the presence of electrons in the flow, or self-absorption. It is found that the broadening effect of H- $\alpha$  is most significant in the region within 25 mm from the center. This indicates that the electron number densities might be notably high here, thus electrons can act as the main collision partner in the region, accelerating the e<sup>-</sup>-H collisions. This is consistent with the high level of H- $\alpha$  radiance in region 3 shown by Fig. 3.19b. Also, the delayed presence of electron number density increase conforms with region 1 and 2 of the Fig. 3.19b, indicating a slow ionization rate in these regions.

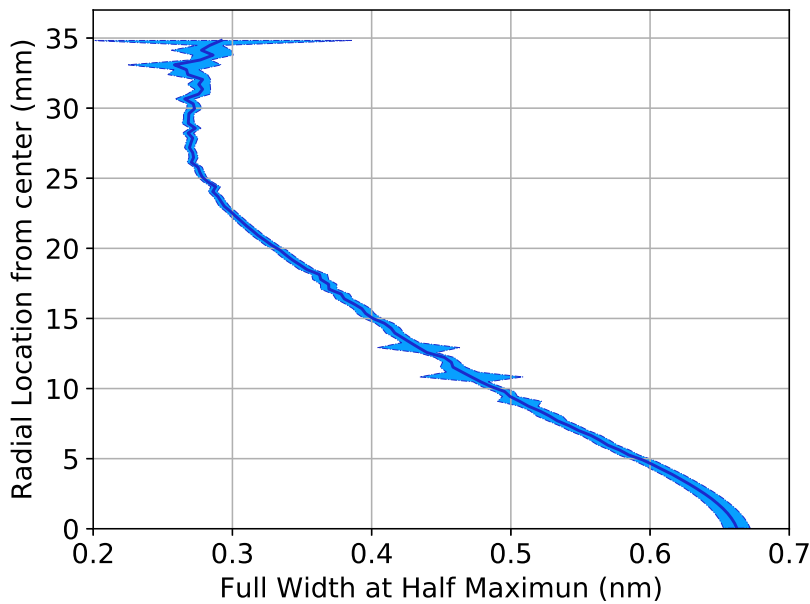


Figure 3.20: Linewidths for Abel inverted spectral radiances of H- $\alpha$  along the radial direction for the radial experiment.

### 3.5.1 Effect of Aluminium Contamination on Radial Distributed Radiation

A repeat radial experiment was performed, which has repeatable shock speeds with the other one, but the observed Balmer radiation is much stronger. The H- $\alpha$  and Al<sup>+</sup> radiance from this repeat experiment, as well as the data from the other radial experiment, which has been shown in section 3.4.2, are shown in Fig. 3.21a. It was found that the Al<sup>+</sup> radiation level in this repeat experiment is higher, and occurs closer to the outer edge of the shock layer than the other one. In order to investigate the relationship between Al<sup>+</sup> and H- $\alpha$  radiation, data from these two experiments were Abel inverted, and shown in Fig. 3.21b.

From the shock edge (at 40 mm) to the overlap point (at 0 mm), although these two experiments have different levels of H- $\alpha$  and Al<sup>+</sup> radiation, their radial radiance distributions, as well as the relationships between H- $\alpha$  and Al<sup>+</sup> radiance profiles are similar. Three non-equilibrium regions can also be seen in the inverted data from the repeat experiment, and are marked in Fig. 3.21b. The

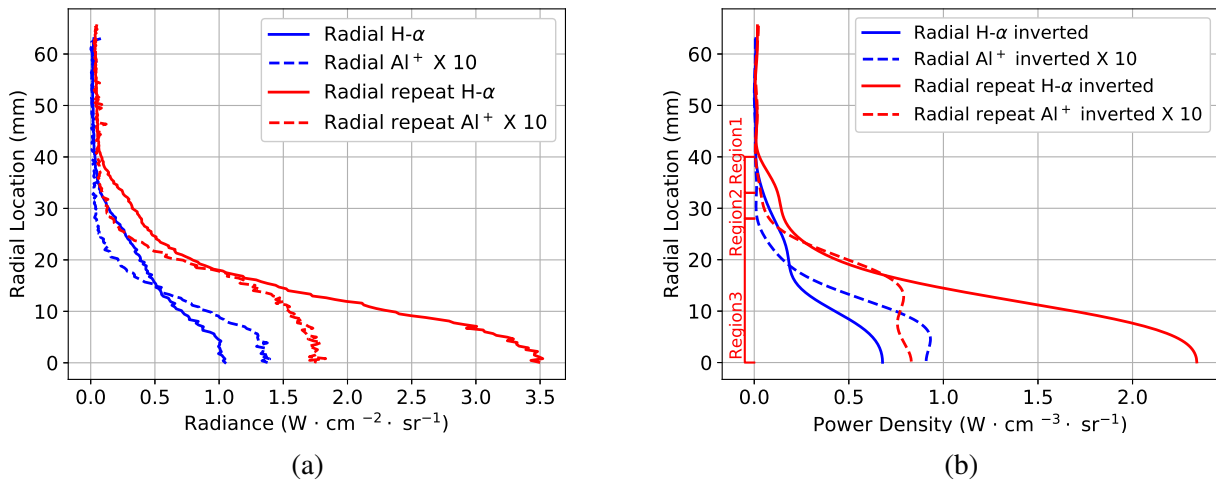


Figure 3.21: (a): Measured H- $\alpha$  and Al<sup>+</sup> radiance profiles. (b): Abel inverted results from radial experiments and its repeat.

radiance variation could be due to different levels or the distributions of aluminum contamination, or other contaminants, due to different tunnel cleanliness. However, higher levels of contamination appears to only squeeze the non-equilibrium process spatially but won't affect the characterization of these three regions in the shock layer. It is also worth noting that the region 2 becomes shorter when the aluminum contamination is present in larger amounts. This might suggest that a cleaner flow may obtain an even larger region 2, therefore the timing of the region 3 transition may not be representative of a flight condition.

## 3.6 Conclusions

Experiments using a substituted test gas with an increased helium concentration compared to Saturn's atmosphere have been conducted in the X2 expansion tube. This condition was designed to recreate the frozen post-shock temperature in a proposed Saturn entry trajectory, to simulate representative Saturn entry conditions at around 26 km/s with an achievable speed in X2 of around 18 km/s and to study the mechanisms of radiation in such flows.

The time-resolved shock layer radiation from H- $\alpha$  was captured using a high speed camera with a bandpass filter. During the test time the measured intensity was low in the post-shock region, and high near the body. This can be indicative of a highly non-equilibrium post-shock flow.

Spectra measured axially and radially were calibrated and analyzed. Axial spectra show the radiation along axial plane that includes the stagnation streamline. Steady H- $\alpha$  and H- $\beta$  radiances in the post-shock region were observed, which conforms with the spectroscopic measurements performed in other Saturn entry experimental studies. After Abel inversion, the radiance measured through the radial plane can be interpreted to obtain the radial radiation distribution. Combining the inverted radiance profiles of H- $\alpha$  and Al<sup>+</sup>, the radial distribution can be divided into dissociation, heavy particle collisions dominated ionization, and e<sup>-</sup>-H collisions dominated ionization regions. This is consistent

with the natural processes of hydrogen ionization, which start with heavy particle collisions, and proceed with  $e^-$ -H collisions as the primary ionization mechanism after a sufficient pool of electrons has been reached. The evidence of the slow ionization was also observed by Abel inverted spectral lines, which have constant line widths in the radial region near shock front, and get more broadened near the overlap point.

In these experiments, it appears that the non-equilibrium processes can be affected by aluminum contamination, as it can act as the colliding partner in heavy particle collisions, and also ionize to releases electrons, which is the main catalyst for  $e^-$ -H collisions. After the concentration of  $e^-$  is sufficient to start the  $e^-$ -H mechanism of ionization, the role of contaminants would be less important.

In conclusion, a non-equilibrium radiative field with delayed ionization, which is the characterization of the chosen Saturn entry trajectory, has been generated by this increased helium condition in X2. This experimentally shows that increasing the amount of helium gives the possibility for this type of ground testing facility to simulate the radiation during Saturn or other giant planet entries.

This condition will be used in X2 for more complex blunt body measurements, such as heat flux measurements or ablation tests, to further investigate Saturn entry post-shock environment. This substitution can also be used to enable other ground testing facilities to simulate Saturn or other giant planet entries. Moreover, the substitution using neon as the diluent in the test gas instead of helium is another way to enable ground facilities to simulate non-equilibrium shock layer in giant planet entries, inside their performance envelopes. Neon has a lower specific heat than helium, so using neon in the test gas will provide more room to get to a higher post-shock temperature with the same energy addition.



## Chapter 4

---

# Experimental Validation of a Test Gas Substitution for Simulating Scaled Giant Planet Entry Conditions

---

**Reproduced entirely from a paper published in the Experiments in Fluids [2]:**

Yu Liu, and Christopher M. James, and Richard G. Morgan ,and Timothy J. McIntyre, “Experimental Validation of a Test Gas Substitution for Simulating Scaled Giant Planet Entry Conditions in Impulse Facilities,” *Experiments in Fluids*, 61(9):198, 2020.

See *Publications included in this thesis* in the preamble of this thesis for a statement of the author contributions to this paper. Some minor changes were made to the as-published paper for the purposes of inclusion into this document, and are detailed in Appendix A. The Introduction and Section 4.4.1 have also been adjusted to avoid overlapping contexts among chapters.

### Abstract

Scaled giant planet entry testing is beyond the simulation capability of most impulse facilities, which limits the ground testing data available for computational model validation. Substituting the He in their predominately H<sub>2</sub>/He atmospheres with Ne has been used in the previous experiments. This enables higher temperature shock layers to be recreated using the same facility performance. For binary hydrogen dissociation and ionization reactions, the substitution gives similarity with non-equilibrium processes, but has never been experimentally validated by direct comparison with H<sub>2</sub>/He relaxation data in a region where the facility simulation capabilities in using H<sub>2</sub>/He and H<sub>2</sub>/Ne overlap. This work demonstrates and validates a scaling method based on the substitution in terms of flow relaxation. A H<sub>2</sub>/Ne condition was designed to recreate the post-shock relaxation of a H<sub>2</sub>/He condition in our X2 expansion tube. The two conditions were experimentally tested with cylindrical test models, and shock layer radiation from the Balmer series was measured. The spectroscopic data using the H<sub>2</sub>/Ne condition show a successful recreation of the non-equilibrium processes of the target H<sub>2</sub>/He condition, experimentally validating the scaling method. High speed

images demonstrate that the associated radiation field is also correctly reproduced. With the use of this substitution, the facility can now be used to simulate high speed giant planet entries with confidence, and the available ground testing envelope is extended to much higher speeds.

## 4.1 Introduction

Giant planets—Jupiter, Saturn, Uranus, and Neptune, are the gaseous planets in our solar system composed mainly of hydrogen and helium. Since the successful Galileo mission to Jupiter and its moons, there is a growing interest for further exploration of the giant planets [30, 89]. The proposed entry velocities for the missions into these planets are between 20 and 50 km/s [18, 25, 32], which are beyond the performance envelopes of most ground facilities. This limits the breadth of the ground testing data that can be obtained to assist computational model validation.

In 1995, the Galileo Probe entered Jupiter’s atmosphere at a velocity of 47.4 km/s. This probe experienced the highest entry heat load ever recorded. For this extremely hot shock layer, there were not many methods available to validate the numerical modeling, and there was not sufficient knowledge to understand the aerothermodynamics. Shock layer prediction for the heat shield design was conducted with the assumption of thermochemical equilibrium and fully turbulent flow [34]. The flight data showed that the models which were used to design the heat shield over-predicted the recession at the stagnation point, whereas the ablation in the frustum region was under-predicted [17, 18]. Overall, only half of the heat shield’s mass ablated during the entry. These dependencies can be explained by the lack of knowledge of Jupiter’s atmospheric composition [64, 65], the non-equilibrium phenomenon during radiative heating [63], and the turbulence in the ablation layer [19]. After the mission, progress in numerical modeling of the recession during the entry has been performed with updated numerical models [19, 36–38]. However, those numerical models have only been validated macroscopically against the flight recession data, and have not been further investigated through ground testing data, such as spectroscopic data, heat flux, and shock standoff. This drives the development of improved ground testing techniques to generate more datasets for a better understanding of the aerodynamic heating during this type of entry.

The entry conditions into Saturn and Uranus were ground tested in EAST, and the shock layer radiation was measured by Cruden and Bogdanoff [20]. EAST data were also compared with the numerical results from Palmer et al. [25]. Qualitative agreement of the flow relaxation was found, while further validation is required with more extensive measurements over a longer length scale.

EAST is a non-reflected shock tube and cannot start steady flows around a test model at these conditions. Expansion tubes, such as X2 [42] at the University of Queensland, have longer test times for comparable conditions; it is, thus possible to conduct blunt body experiments with a broader range of measurements. However, a recent work showed that it was only able to simulate giant plant entry up to the enthalpy experienced in the Uranus entry [9] using H<sub>2</sub>/He mixtures. However, since testing was conducted at the facility’s peak performance, the generated flow condition had a very low density, meaning that it was not appropriate for scaled testing. As these were the fastest experiments ever

performed in an expansion tube (at around 20 km/s), the facility's shock detection system was found to be not suitable for accurately measuring shock speeds at such high speed and low-density conditions, and very high uncertainties were seen.

In 1998, Stalker and Edwards [22] proposed a substitution using higher fractions of helium than in real entries or using H<sub>2</sub>/He instead of H<sub>2</sub>/Ne to simulate the non-equilibrium processes during the entry into hydrogen-helium atmospheres. To validate the increased helium test gas substitution method, a condition with 80% He/20% H<sub>2</sub> (by volume) was designed [23] and tested in with a spherical test model in X2 [1]. This condition can recreate the post-shock frozen temperature for the proposed Saturn entry trajectory point  $t = 206$  s [25]. Spatially resolved radiation from hydrogen atomic species was imaged. Radiation measurements found that a highly non-equilibrium flow field was generated with this higher amount of helium condition, and the representative Saturn entry non-equilibrium flow that was observed in the EAST tests was achieved. However, this condition is at the upper end of X2's performance, so the limitations of the helium substitution have already been reached. Thus, merely increasing the fraction of helium in the test gas is not enough to simulate faster giant planet entries, or to perform scaled tests.

The substitution using neon instead of helium in the test gas was also proposed by Stalker and Edwards [22]. They found that using neon or helium as the inert collision partners did not affect the normalized density variable along a streamline, except when the ionization of neon took place when the temperature exceeds around 20000 K. Neon weighs five times as much as helium, and thus its specific heat is one-fifth of that for helium. Hence, the neon substitution can be used to generate hotter shock layers with the same performance compared to H<sub>2</sub>/He conditions. Giant planet entry conditions can be achieved at much slower speeds, allowing excess facility performance to be used to generate scaled conditions.

The neon substitution was used by Stalker [16] in employing H<sub>2</sub>/Ne mixtures to generate ionizing flows for H<sub>2</sub>/He ionization rate validation. The H<sub>2</sub>/He ionization rates were found to be consistent with the H<sub>2</sub>/Ne flow relaxation measurements. This substitution was also tested by Higgins [45] in X2 in terms of the matching of macroscopic flow properties such as shock standoff. A test gas with 85% neon in a H<sub>2</sub>/Ne mixture was used to generate a highly ionized test flow at around 11 km/s. The validation of shock standoff with the ionization rate was used to obtain coefficients for an empirical model of the ionization process, but no direct measurements of relaxation or radiation were made. This work is also at the edge of the validity of the neon substitution, as the neon was partially ionized [23], and it is not yet known what the effect of Ne ionization will be on the H kinetics.

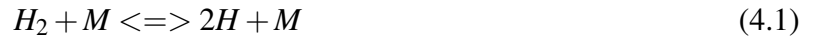
The current study demonstrates an experimental validation of the neon substitution, in terms of its application to non-equilibrium flow scaling. A condition with H<sub>2</sub>/Ne as the test gas was designed to match the existing H<sub>2</sub>/He condition from the authors' previous work [1] by duplicating the post-shock frozen temperature. The designed H<sub>2</sub>/Ne condition and the target H<sub>2</sub>/He condition were tested on cylindrical models in X2. Spatially resolved hydrogen atomic radiation along the stagnation streamline, as well as filtered high speed images of the whole flow-field focusing on hydrogen atomic radiation, were obtained. The spectroscopic data from these two conditions were interpreted and compared for

the experimental validation. This is the first time that spectrally resolved data from both H<sub>2</sub>/He and H<sub>2</sub>/Ne conditions are obtained for direct quantitative comparison.

## 4.2 Test Gas Modeling

In this section, the key factors that control the binary dissociation and ionization rates along a streamline in non-equilibrium H<sub>2</sub>/Ne and H<sub>2</sub>/He mixtures are discussed. It has been noted that, in the shock layers during giant planet entries such as for Jupiter, Saturn, and Uranus, dissociation is a much faster process than ionization [25, 90]. In the cases when hydrogen dissociation is not efficiently complete before ionization begins, the scaling method in this section will also work due to the binary nature of the reactions involved. Thus, in the analysis, dissociation is assumed to be complete before significant ionization starts.

In this study, helium and neon are considered as inert gases and only act as the collision partners, as their excitation energies (21 eV and 17 eV respectively) are sufficiently higher than that for hydrogen (10 eV) [22]. Using M to represent a He or Ne atom, the dissociation process in the immediate post-shock flow can be described as:



Taking  $r$  to be the mole fraction of molecular hydrogen in the test gas fill state, the molar concentration of hydrogen and the inert gas can be calculated from the perfect gas equation and Dalton's law of partial pressures as

$$[H_2] = \frac{rP_f}{RT_f} \quad (4.2)$$

$$[M] = \frac{(1-r)P_f}{RT_f} \quad (4.3)$$

Here,  $P_f$  and  $T_f$  are the local pressure and temperature of the flow at the immediate post-shock state, and R is the universal gas constant. The time rate of change of H molar concentration can be expressed as:

$$\frac{\partial[H]}{\partial t} = 2K_{fd}[H_2][M] = 2K_{fd}r(1-r)\left(\frac{P_f}{RT_f}\right)^2 \quad (4.4)$$

Here  $K_{fd}$  is the forward dissociation reaction rate coefficient. The reverse reaction rate is negligible in the highly non-equilibrium region especially in the immediate post-shock region. This is because the density of the giant planet entry conditions is generally low, and little recombination is seen.

Defining the mole fraction of the initial H<sub>2</sub> dissociated to H to be  $\alpha$ , the molar concentration of H and H<sub>2</sub> can be expressed as

$$[H] = \frac{2rP\alpha}{RT} \quad (4.5)$$

$$[H_2] = \frac{rP(1-\alpha)}{RT} \quad (4.6)$$

Then  $\alpha$  can be written as:

$$\alpha = \frac{[H]}{2[H_2] + [H]} \quad (4.7)$$

The time rate of change of  $\alpha$  at the immediate post-shock state (where  $[H] = 0$ ) can be calculated by:

$$\frac{\partial \alpha}{\partial t} = \frac{\partial [H]}{\partial t} \frac{1}{2[H_2] + [H]} = K_{fd}(1-r) \frac{P_f}{RT_f} \quad (4.8)$$

Introducing the streamline velocity  $V$ , we can write  $\frac{\partial \alpha}{\partial x} = \frac{\partial \alpha}{\partial t} \cdot \frac{\partial t}{\partial x} = \frac{1}{V} \cdot \frac{\partial \alpha}{\partial t}$ . The dissociation rate along the streamline at the immediate post-shock state can then be described as:

$$\frac{\partial \alpha}{\partial x} = K_{fd}(1-r) \frac{1}{RT_f} \frac{P_f}{V_f} \quad (4.9)$$

The reaction rate coefficient  $K_{fd}$  is only related to the local temperature  $T_f$ , which is the immediate post-shock temperature. Equation 4.9 shows that, if  $T_f$  in the H<sub>2</sub>/He condition is duplicated in a H<sub>2</sub>/Ne condition, the initial dissociation rate would also be duplicated along  $(1-r)x_V^P$ . Dissociation processes are binary reactions when recombination is negligible; thus, the net production of dissociated product is proportional to the Damköhler number when traversing a distance L [82].

Introducing the binary scaling variable  $\chi = \int \frac{P}{V} dx$  [22], the dissociation rate along the  $\chi$  coordinate can be expressed as:

$$\frac{\partial \alpha}{\partial \chi} = K_{fd}(1-r) \frac{1}{RT_f} \quad (4.10)$$

In the binary scaling variable coordinate, only the hydrogen mole fraction  $r$  and the post-shock frozen temperature,  $T_f$ , are required to match the target condition to recreate the dissociation rate. If  $r$  is different from that in the target condition,  $\chi$  needs to be scaled by  $(1-r)$  to compensate for the hydrogen composition difference to match the dissociation rate.

At the initial stage of ionization, the major contributors to the reaction are collisions between inert gas (helium or neon) and hydrogen atoms, with the reaction:



When dissociation completes, the molar concentrations in the flow have a ratio of  $[H]/[M] = 2r/(1-r)$ . The molar concentrations of the hydrogen atoms  $[H]$  and the diluent gas  $[M]$  are

$$[H] = \frac{2rP_i}{(1+r)RT_i} \quad (4.12)$$

$$[M] = \frac{(1-r)P_i}{(1+r)RT_i} \quad (4.13)$$

Here,  $P_i$  and  $T_i$  are the local pressure and temperature when ionization begins.

The time rate of change of the H<sup>+</sup> molar concentration can be expressed as:

$$\frac{\partial [H^+]}{\partial t} = K_{fi}[H][M] = K_{fi} \frac{2r(1-r)}{(r+1)^2} \left( \frac{P_i}{RT_i} \right)^2 \quad (4.14)$$

Here  $K_{fi}$  is the forward reaction rate coefficient for ionization. The reverse reactions are negligible due to the low density.

Defining the mole fraction of H ionized to  $H^+$  to be  $\beta$ , the molar concentration can be expressed as

$$[H^+] = \frac{2rP\beta}{(r+1)RT} \quad (4.15)$$

$$[H] = \frac{2rP(1-\beta)}{(r+1)RT} \quad (4.16)$$

Then  $\beta$  can be written as

$$\beta = \frac{[H^+]}{[H^+] + [H]} \quad (4.17)$$

The time rate of change of  $\beta$  at the initial ionization state (where  $[H^+] = 0$ ) can be calculated by:

$$\frac{\partial \beta}{\partial t} = \frac{\partial [H^+]}{\partial t} \frac{1}{[H^+] + [H]} = K_{fi} \frac{1-r}{r+1} \frac{P_i}{RT_i} \quad (4.18)$$

Similarly, the ionization rate along the stream-wise distance at the initial ionization stage can be described as:

$$\frac{\partial \beta}{\partial x} = K_{fi} \frac{1-r}{r+1} \frac{1}{RT_i} \frac{P_i}{V_i} \quad (4.19)$$

Accordingly, the ionization rate along the binary scaling variable  $\chi$  is:

$$\frac{\partial \beta}{\partial \chi} = K_{fi} \frac{1-r}{r+1} \frac{1}{RT_i} \quad (4.20)$$

Combining Equations 4.10 and 4.20, to recreate both dissociation and ionization rates along  $\chi$  in the target condition,  $r$ ,  $T_f$ , and  $T_i$  need to be duplicated. When  $r$  is matched, if  $T_f$  can be duplicated,  $T_i$  will also be recreated, and vice versa, as the energy available to be turned into dissociation is identical with the same  $r$ . Then, the relaxation processes before recombination becomes significant can be recreated.

It should also be noted that the scaling method above is only applicable to two body interactions. Radiative processes are single body interactions. If they play an important role in determining the state populations, this will not be achieved through binary scaling. Also, the three body recombination processes will become more important as the pressure is increased or the flow reaches an equilibrium state. In these cases, this binary scaling method will be no longer valid.

### 4.3 Condition Design and Numerical Validation

In previous studies, an X2 condition with 20%/80%  $H_2/He$  (by volume) as the test gas was developed [23] and tested [1] targeting the Saturn entry trajectory point  $t = 206$  s [25]. The entry velocity of this trajectory point is 26.3 km/s, and its temperature and density are 141 K and  $1.8 \times 10^{-5}$  kg/m<sup>3</sup> respectively [25]. This  $H_2/He$  condition can recreate the post-shock frozen temperature  $T_f$  for this entry trajectory point, and has been experimentally shown to generate representative non-equilibrium flow for this entry [1]. In the current study, this  $H_2/He$  condition is used as a reference to design the condition with a  $H_2/Ne$  test gas. The goal for the new condition design is to duplicate the hydrogen mole fraction  $r$  and the post-shock temperatures  $T_f$  and  $T_i$ . From Section 4.2, if these requirements

have been satisfied, the dissociation and initial ionization rates generated by the target condition will be recreated along  $\chi$ .

In the designed H<sub>2</sub>/Ne condition, the chosen test gas composition is 20%/80% H<sub>2</sub>/Ne (by volume) to maintain the hydrogen mole fraction  $r$  between the two conditions. The freestream flow properties generated by the target condition and the designed H<sub>2</sub>/Ne condition were predicted by a state-to-state analytical expansion tube analysis code PITOT [24], and are shown in Table 4.1. PITOT prediction was run in a partially theoretical mode where experimentally measured shock tube shock speed and fill pressures were used to predict the freestream flow properties. It should be noted that as the PITOT prediction of the freestream properties prediction for this target condition in the previous chapter was using the fully theoretical mode, there is a slight difference for the calculated flow properties between Table 3.2 and Table 4.1. The post-shock frozen state was obtained from the numerical prediction using the in-house code Poshax3 [80, 81], which predicts the post-shock flow properties in inviscid and one-dimensional flow assuming no body. The fully dissociated state and equilibrium state flow properties were calculated by NASA's Chemical Equilibrium with Applications (CEA) program [91, 92]. These results are listed in Table 4.1. Here, the designed condition which uses H<sub>2</sub>/Ne as the test gas, and the target H<sub>2</sub>/He condition, are termed ‘helium condition’ and ‘neon condition’, respectively.

Table 4.1: Details of the test conditions.

Condition name	Helium condition	Neon condition
Condition details		
Driver fill gas (by volume)	77.2 kPa He	110.3 kPa He
Primary diaphragm	2.5 mm scored steel	1.2 mm scored steel
Shock tube gas (by volume)	2.0 kPa 20%/80% H <sub>2</sub> /He	2.0 kPa 20%/80% H <sub>2</sub> /Ne
Secondary diaphragm thickness	13 $\mu$ m aluminum foil	13 $\mu$ m aluminum foil
Acceleration tube	0.5 Pa air	13.5 Pa air
Freestream flow		
Pressure	80 Pa	980 Pa
Temperature	500 K	1900 K
Velocity	18810 m/s	8550 m/s
Mach number	14.6	7.3
Gas composition (by volume)	20%/80% H <sub>2</sub> /He	20%/80% H <sub>2</sub> /Ne
Post-shock flow		
Frozen state temperature	26700 K	26200 K
Frozen state pressure	19200 Pa	58000 Pa
Frozen state velocity	4190 m/s	1970 m/s
Frozen state density	$3.1 \times 10^{-4}$ kg/m <sup>3</sup>	$44.0 \times 10^{-4}$ kg/m <sup>3</sup>
Fully dissociated state temperature	21100 K	21000 K
Fully dissociated state pressure	19500 Pa	58900 Pa
Equilibrium state temperature	12300 K	13000 K
Equilibrium state pressure	21600 Pa	64900 Pa
Equilibrium gas composition (by volume)	e-: 0.12, H: 0.18, He: 0.59, H+: 0.11	e-: 0.11, H: 0.20, Ne: 0.59, H+: 0.10

It can be seen in Table 4.1 that the designed neon condition can approximately recreate the post-shock temperature of the helium condition in both frozen and fully dissociated states, with slower flow speed and elevated pressure. Thus, temperature requirements for the substitution are satisfied.

The frozen temperature T<sub>f</sub> in the X2 conditions approximately matches that in the Saturn entry condition. According to Equation 4.10, their dissociation rates would match in the (1-r) $\chi$  axis at the immediate post-shock state, if recombination is ignored. However, both X2 conditions have an

elevated hydrogen mole fraction (80%) compared to the flight condition(15%), so that the dissociation process in the Saturn entry condition will equilibrate to a different state. Thus, only the dissociation rate at the immediate post-shock region will match along  $(1-r)\chi$  among the X2 conditions and the Saturn entry condition.

The post-shock flow relaxation generated by the helium condition, neon condition, and the trajectory point  $t = 206$  s [25] were numerically calculated by Poshax3. The chemical reaction schemes [37] implemented for these conditions include molecular hydrogen dissociation, ionization of hydrogen atoms, and ionization of helium or neon. The hydrogen dissociation and ionization rates for H<sub>2</sub>/He were also used in H<sub>2</sub>/Ne mixtures, as the dissociation rates employed are for the collisions between H<sub>2</sub> and all collision partners, and hydrogen ionization rates for H<sub>2</sub>/Ne were experimentally found to agree with that for H<sub>2</sub>/He mixtures [16]. In addition, it was assumed that neon ionization has the identical reaction rate coefficient as helium, except that the activation energy becomes 21.6 eV. The flow is assumed to be in thermal equilibrium and with no radiative energy exchange. Freestream pressure, temperature, velocity, and the gas composition predicted by PITOT were the inputs for Poshax simulations.

The flow properties in the non-equilibrium flows generated by the two X2 test conditions and the equivalent Saturn entry condition are presented along the  $(1-r)\chi$  axis in Fig. 4.1. Quantitative agreement can be seen in the non-equilibrium relaxation processes generated by the helium and neon conditions, in terms of temperature and species mole fraction profiles. This numerically validates that, if T<sub>f</sub> and r are duplicated, the non-equilibrium processes will be recreated along  $\chi$ .

Qualitative agreement can also be found between the results from the Saturn entry condition and the X2 conditions. Although the temperature and species mole fraction profiles do not match due to r being different, the dissociation in the Saturn entry condition approximately finishes at the same point. This shows that this substitution theory will approximately work well even with different H<sub>2</sub> mole fractions r, if recombination is negligible.

It is worth noting that the pressure and velocity are approximately constant during the relaxation when there is no body, so that the P/V value will remain approximately constant. Based on Equations 4.9 and 4.19, the binary scaling variable axis can be simplified as the stream-wise axis scaled by P<sub>f</sub>/V<sub>f</sub>. Compared to the  $\chi$  coordinate which requires local pressures and velocities, this provides a more direct scaling method for experimental data interpretation, and was used in this work to perform a quantitative comparison of the flow relaxation using helium and neon conditions.

## 4.4 Experimental Results

### 4.4.1 Facility

The experiments were performed in the X2 expansion tube at the University of Queensland. Introduction of X2 facility can be found in Chapter 3.

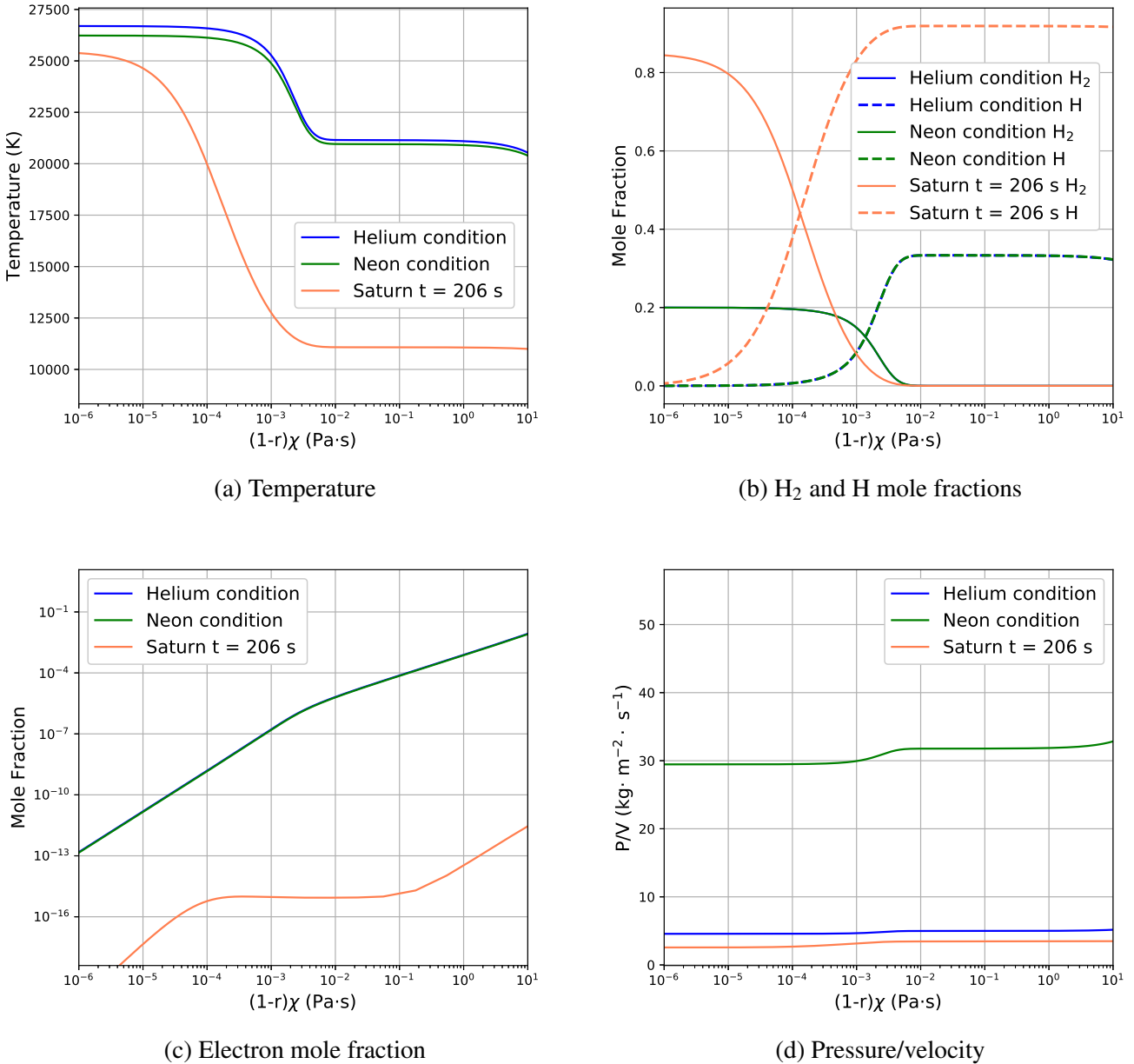


Figure 4.1: Selected flow properties predicted along the  $(1 - r)\chi$  coordinate in the target helium condition, designed neon condition, and Saturn entry trajectory point [25] from Poshax.

#### 4.4.2 Test Model and Instrumentation

The test model used to study relaxation similarity generated by the two conditions is a cylinder, with a diameter of 25 mm and a length of 75 mm, to achieve the aspect ratio of 3 to reduce edge effects. The model size was chosen to fit the core flow of both the helium condition and the neon condition. Compared to spherical models, cylindrical models have the advantage of generating quasi-two-dimensional flows with a large shock standoff, which makes it easier to study relaxation and compare to two-dimensional simulations as observations can be made along lines of approximately uniform conditions.

Two cylindrical models with an identical length of 100 mm, but with different radii (25 mm and 33.3 mm respectively) were also used in this study to explore how the velocity gradient affects the

flow relaxation. In these experiments, a larger model length was chosen to make the full use of the core flow size of the helium condition.

The instrumentation used in this study is demonstrated shown in Fig. 4.2, with a high speed camera imaging the shock layer on one side of the test section, and an OES system, placed on the other side, capturing the radiation emitted from the stagnation streamline in front of the model.

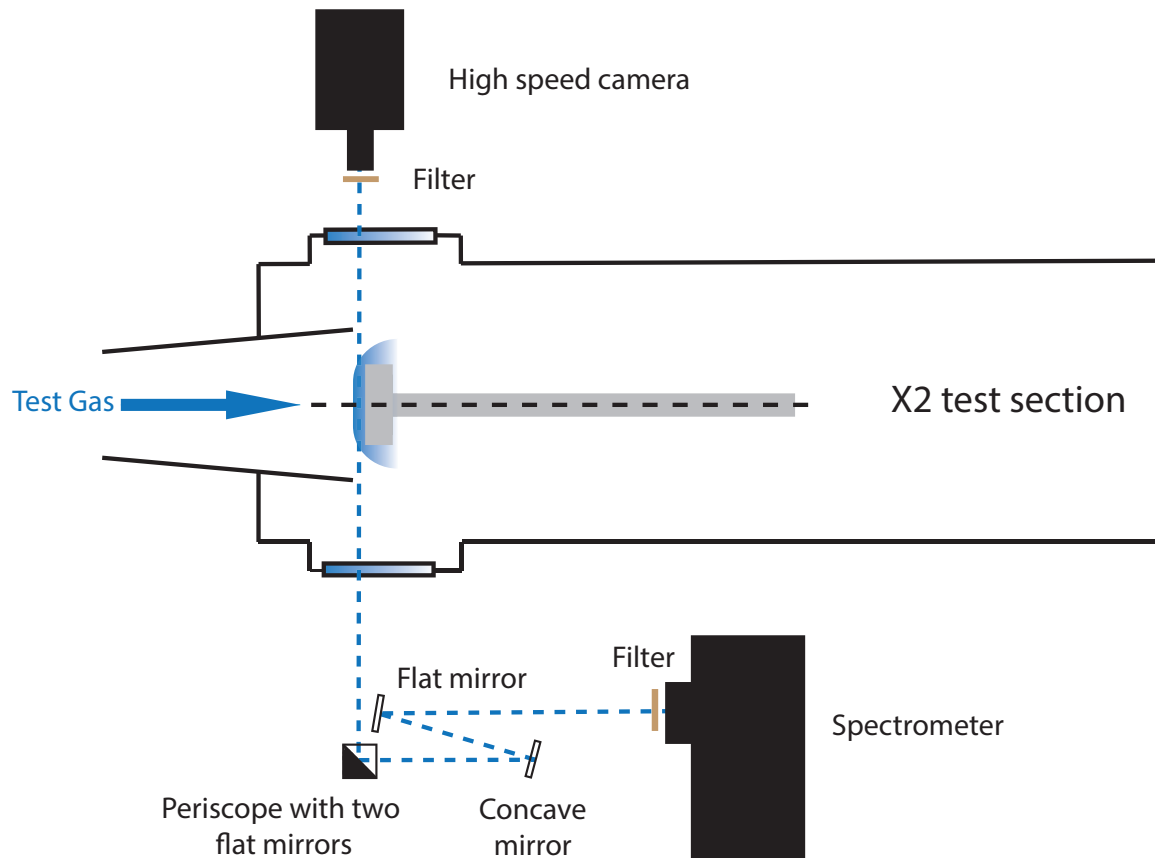


Figure 4.2: Schematic of a typical arrangement of the high speed imaging system and optical emission spectroscopy system for stagnation region radiation studies (not to scale).

In this study, a Shimadzu HPV-1 high speed camera with a Nikon Micro Nikkor 200mm 1:4D lens was used to record the time-resolved emission during each experiment. This camera can record 100 frames per trigger. Hence, with the recording frequency set to 500 kHz, the camera will record the emission for 200  $\mu$ s for each experiment.

The OES system consists of a spectrometer mounted with an intensified CCD (charge-coupled device) camera that is sensitive at visible and near-infrared wavelengths, and supporting optics (mirrors, filter, periscope). A longpass filter (FGL400S) was used to cut off the emission below 400 nm, so that the strong emission lines from the contaminants (aluminum: 394 nm, 396 nm, and calcium: 393 nm, 397 nm) that are just below 400 nm can be removed from the spectrum.

### 4.4.3 Spectroscopic Data

#### Spectroscopic Results

There are six experiments included in this paper. Four experiments were conducted with the helium and neon conditions tested on the 75 mm length model, to investigate the flow relaxation similarity. Among them, two experiments were conducted with each condition. Two experiments were conducted using the helium condition tested with the two different radii models for boundary layer effect investigation. Grating settings and the measured shock speeds are listed in Table 4.2. The shots are named by the condition, model length, model diameter, and the repeat if applicable. Spectra with the center wavelength of 525 nm were obtained with a 150 gpmm grating, enabling the radiation from the hydrogen Balmer series between 400 nm and 690 nm to be measured. To check the repeatability, shock speeds along the shock tube and the acceleration tube were measured and compared. It can be seen from the table that the shock speeds of these experiments are statistically the same as they have overlapping uncertainties.

Table 4.2: Grating settings and the measured shock speeds for each experiment.

Shot name	Grating gpmm	Center wavelength nm	Shock speed (Shock tube) m/s	Shock speed (Acceleration tube) m/s
<b>Helium condition</b>				
HE-75-25-1	150	525	$8600 \pm 80$	$18200 \pm 300$
HE-75-25-2	150	525	$8440 \pm 80$	$18600 \pm 300$
HE-100-25	150	525	$8530 \pm 80$	$18600 \pm 300$
HE-100-33.3	150	525	$8570 \pm 80$	$18500 \pm 300$
<b>Neon condition</b>				
NE-75-25-1	150	525	$4910 \pm 40$	$8330 \pm 20$
NE-75-25-2	150	525	$4890 \pm 40$	$8330 \pm 20$

In the experiments, spatially-resolved emission from the stagnation streamline region was diffracted by the chosen grating and recorded as a two-dimensional image on an intensified CCD camera. The absolute intensity values were calibrated and are shown in Figs 4.3a and 4.3b. The horizontal axis of the image shows wavelength, while the vertical axis represents the physical location of the emitted radiance. Flow direction is from top to bottom. It can be seen that similar spectral lines are shown in the spectra from these two conditions, but the H- $\alpha$  (656.3 nm) and H- $\beta$  (486.1 nm) lines using the neon condition are broader near the model than using the helium condition, which may indicate stronger ionization near the stagnation region in the neon condition. The shock fronts in this thesis were defined manually as the location where the H- $\beta$  radiance profiles have the highest gradient, and they have been set as 0 mm. This definition of the shock front was used in shock detection for high speed images [79, 93]. The model edge for the experiments using the helium condition (Fig. 4.3a) is at a location around 5.8 mm, while the model edge is approximately at 4 mm in the experiments using the neon condition (Fig. 4.3b). Weak molecular features can be observed near 470 nm, 515 nm, and 544 nm in the immediate post-shock region in both experiments. These are shown in Fig. 4.4 with the

spectral radiance integrated spatially over 0.1 mm in this region. Some of these molecular features were also observed in the 26.3 km/s EAST experiment [20], and they are possibly the emission from water impurities in the tunnel, such as the OH visible B-X band. Near the stagnation point, stronger broadband bremsstrahlung can be observed in the experiments using the neon condition compared to the helium condition, which implies more ionization in the stagnation region.

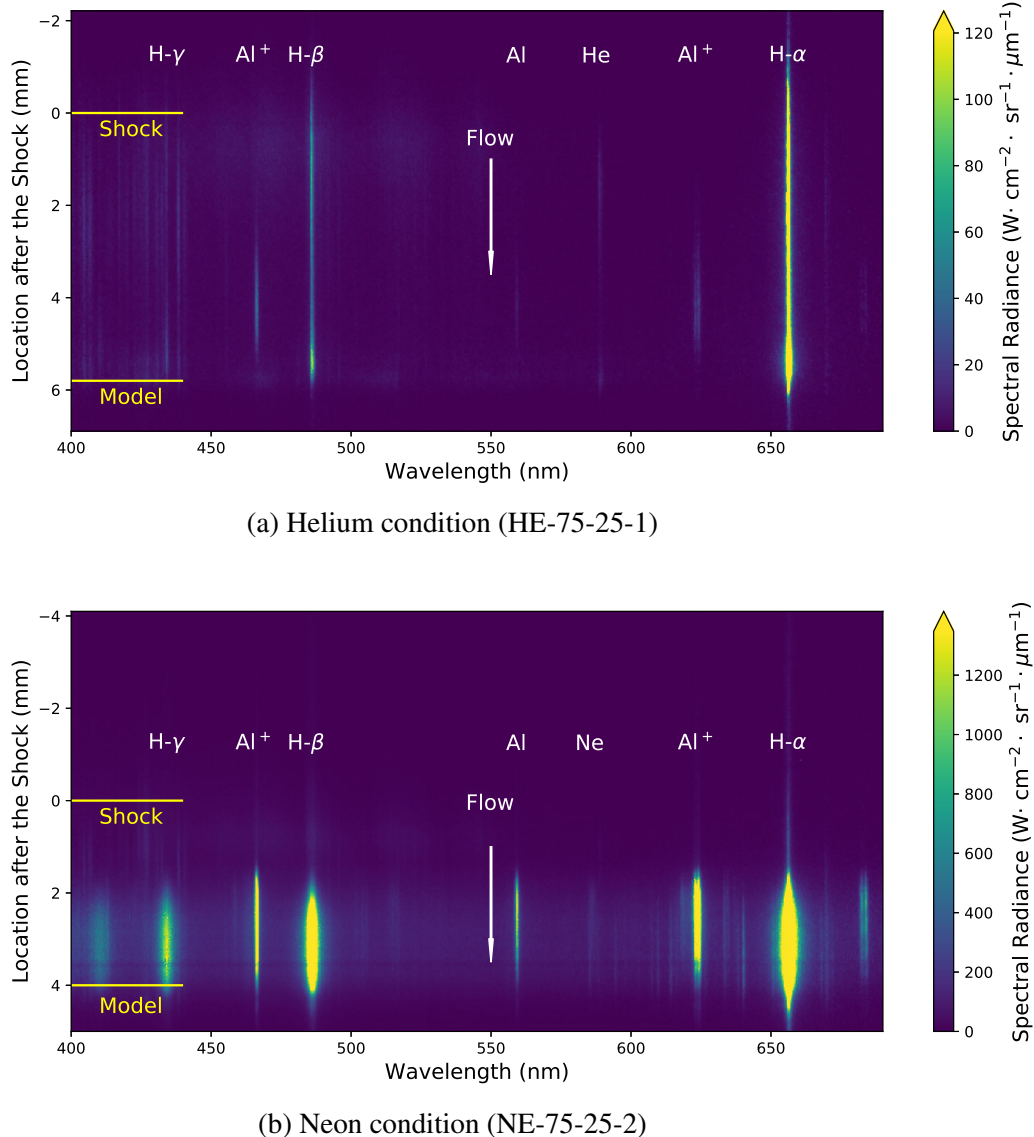


Figure 4.3: Example calibrated spectral data from the experiments with the helium and the neon condition.

The radiance profile for a specific transition along the stagnation streamline can be obtained by integrating the intensity over a wavelength range. In this section, the H- $\alpha$  and H- $\beta$  radiance profiles were obtained over 644-668 nm and 475-495 nm, respectively. The molecular band in the immediate post-shock region and the bremsstrahlung near the stagnation point overlap with H- $\alpha$  and H- $\beta$  spectral lines, and contribute to the integrated radiance as a background. To reduce the contribution from these features, the radiation at the two edges of the integration region was averaged as the background signal and subtracted from the integrated radiance. These H- $\alpha$  and H- $\beta$  radiance profiles are shown in

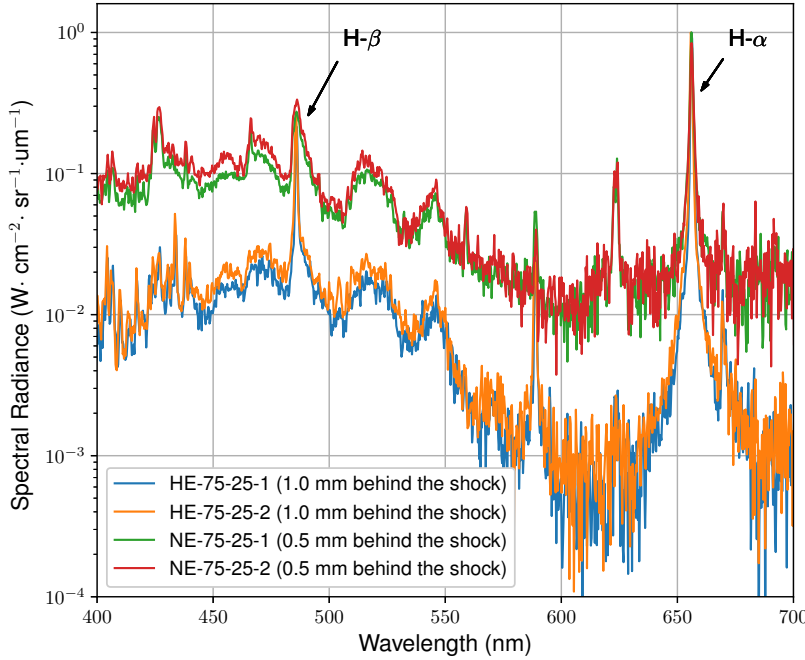


Figure 4.4: Sample spectra behind the shock from the helium condition and the neon condition.

Figs. 4.5a and 4.5b respectively.

In Fig. 4.5a, using the helium condition, H- $\alpha$  radiance profiles experience an increase immediately behind the shock, followed by a flat region, then a rapid increase near the stagnation point. The increase near the stagnation point could be due to the development of the relaxation processes, as the flow slows down and near the stagnation point, there is more time for further relaxation. For the experiments with the neon condition, because the higher  $P_f/V_f$  value will lead to higher reaction rates along the stagnation streamline, the rapid H- $\alpha$  radiance increase near the stagnation point occurs earlier than in the helium condition.

In Fig. 4.5b, H- $\beta$  radiance profiles show a similar trend as in the H- $\alpha$  radiance profiles, except that behind the shock, the H- $\beta$  appears to experience a gradual drop. This is thought to be due to the remaining contribution from the molecular features that cannot be fully eliminated by subtraction as their radiance is not evenly distributed over the chosen wavelength regions.

### Spectroscopic data scaling

The scaling method was numerically validated in Section 4.3, and the experimental data show a qualitatively similar trend in the integrated radiance profiles along the stagnation streamline in Fig.4.5. For experimental validation, spectroscopic data are presented on the stream-wise distance axis scaled as  $(1 - r)x\frac{P_f}{V_f}$  to obtain a quantitative comparison. The radiance values from the X2 experiments were normalized by their  $P_f$  to compensate for the relative number densities of H, and are shown in Fig. 4.6. To give an identical location reference for different conditions, the location of the molecular features in the immediately post-shock region was marked as zero. These plots have been truncated to remove

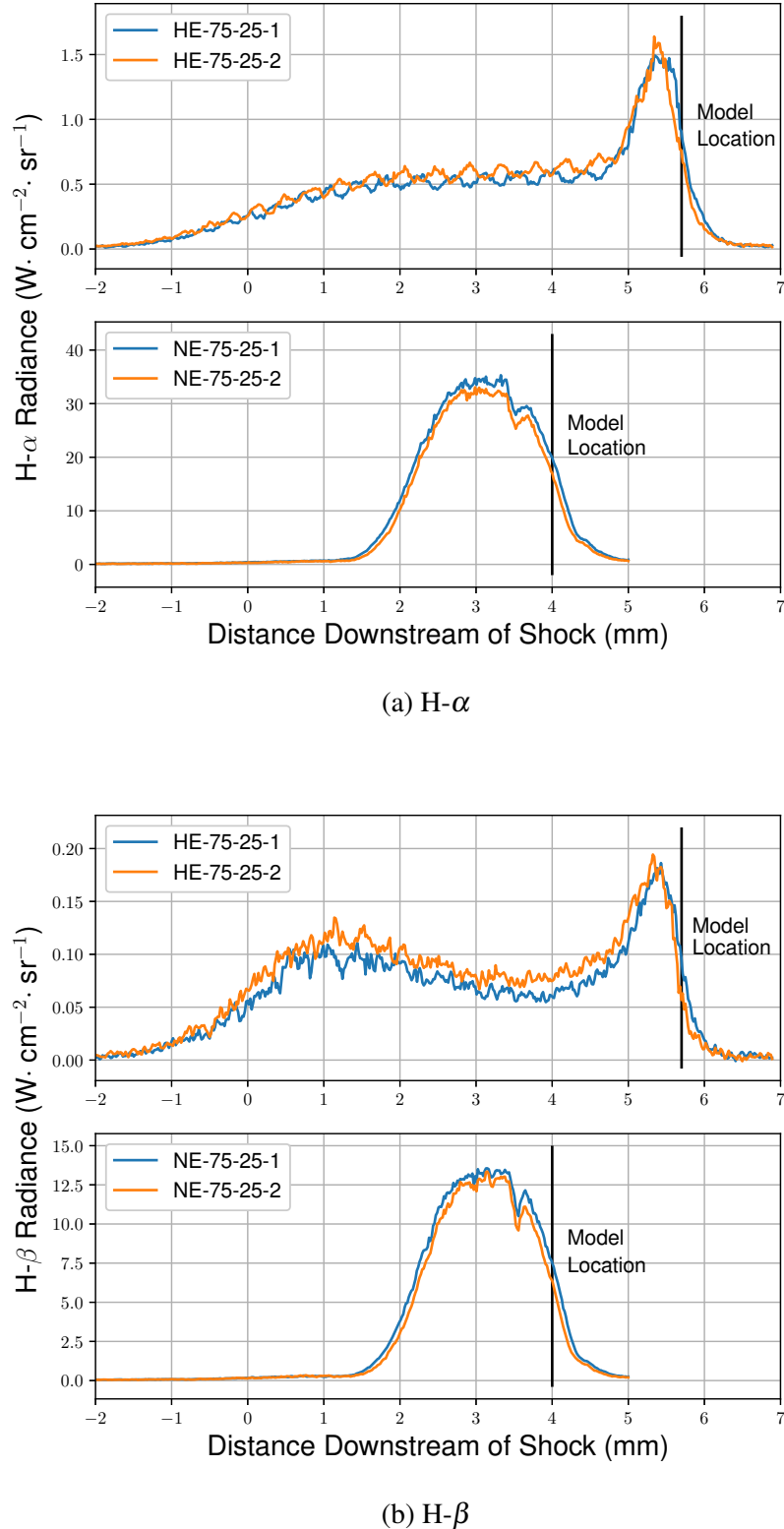


Figure 4.5: Integrated radiance along the stagnation streamline.

further relaxation with the neon condition, to focus on the overlapping region.

It can be seen in Fig. 4.6 that the reactions in the neon condition are more complete in the helium condition. This is because  $(1-r)\frac{P_f}{V_f}$  in the neon condition is larger than in the helium condition. This again shows that the neon substitution allows a binary scaled condition to be designed, and further

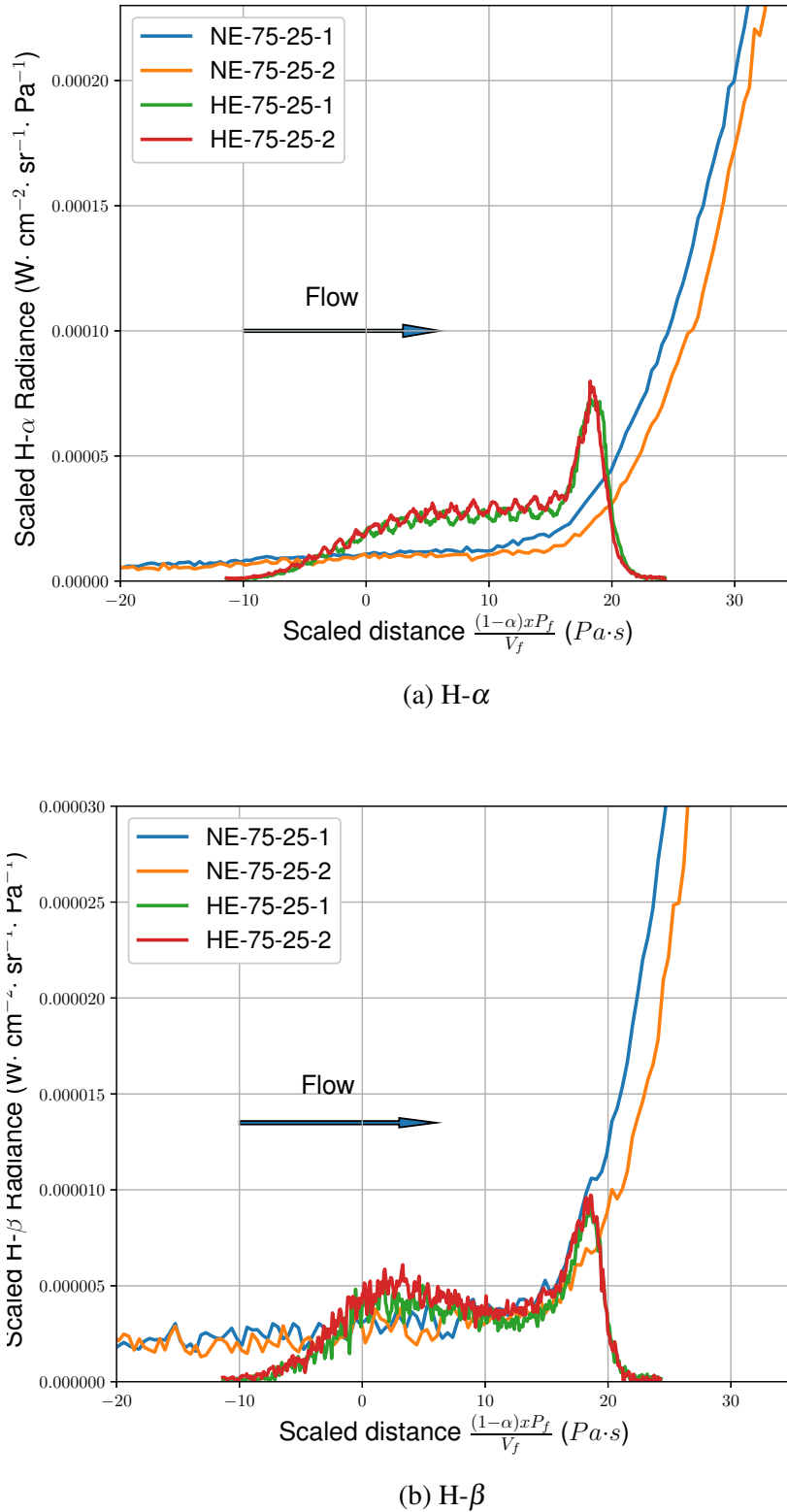


Figure 4.6: Scaled radiance along the scaled stream-wise axis in helium and neon condition. Radiance for helium and neon condition was scaled by  $P_f$ .

relaxation of the target condition can be simulated with a similar shock standoff distance. It is worth noting that with the more complete relaxation achieved by the neon condition, the maximum intensity in the spectra (near the model) will be higher. To capture the maximum intensity without saturating

the camera, the gain would be set low, and there will be not enough signal for the radiation near the shock front. In this case, noise appears to be a problem in the region close to the shock.

In Fig. 4.6a, a qualitative agreement was not found in the scaled H- $\alpha$  data. The radiance profiles in the helium condition ramp up near the wall at 15 Pa·s and stop developing at the stagnation point at around 18 Pa·s; whereas, the neon condition profiles keep developing until they get to the stagnation point.

For the scaled H- $\beta$  data, a quantitative agreement is found between the helium and neon condition data shown in Fig. 4.6b. The radiance profiles match well before the radiance profile in the helium condition gets to the stagnation point at 18 Pa·s and stops developing.

A possible explanation of the discrepancies in H- $\alpha$  profiles is the velocity gradient along the stagnation streamline. In the Section 4.3, we obtained the simplified binary scaling parameter  $(1-r)x\frac{P_f}{V_f}$  to scale the relaxation process generated by the neon condition and the target helium condition. However, this is based on the relaxation process without a body. In our experiments, due to the existence of the body, there will be a velocity gradient along the stagnation streamline, with the velocity decreasing from the frozen state velocity immediately behind the shock to zero near the wall. Along the stagnation streamline, the time of flight increases with  $1/V$ , increasing the available time for reaction. When a particle approaches wall, the velocity gets close to zero, rapidly increasing the time of flight, so that further reaction can occur. Also, temperature tends to quench radiation near the wall. These effects may merge, or the thermal cooling may occur after a localised peak in radiation or reaction caused by the rapid temperature deceleration and the increased time of flight. As the designed neon condition is a binary scaled condition for the existing helium condition due to its higher  $P_f/V_f$  value, to fully recreate the velocity distribution along the scaled distance axis, a scaled down model is required for the neon condition to generate the same binary scaled shock standoff distance as generated by the helium condition.

To investigate how the velocity distribution with different binary scaled shock standoff distance would affect the measured radiance, cylindrical test models with a length of 100 mm, but with different radii (25.0 mm and 33.3 mm) were tested. Experiments using these two models were conducted with the helium condition, and spectroscopic measurements along the stagnation streamline are shown in Fig. 4.7. The estimated shock fronts were marked as 0 mm. Comparing the 25.0 mm radius case with the 33.3 mm radius case, as expected, a larger shock standoff was generated with the larger radius model. As the binary scaling parameter was the same in these two cases, a larger shock standoff can lead to further relaxation.

The results show that the rapid increase in H- $\alpha$  radiance occurs later and develops further in the larger shock standoff case. This discrepancy shows that a larger shock standoff gives further relaxations, and the varying distribution of the velocity is likely to affect the radiance profiles especially near the stagnation point where the velocity gets close to zero. However, a quantitative agreement can be seen in the H- $\beta$  radiance profiles with the different shock standoffs, and with a larger shock standoff, the H- $\beta$  radiance develops further. Different features for H- $\alpha$  and H- $\beta$  profiles could be due to the non-Boltzmann state distributions, which was also found by the Saturn entry radiation tests in

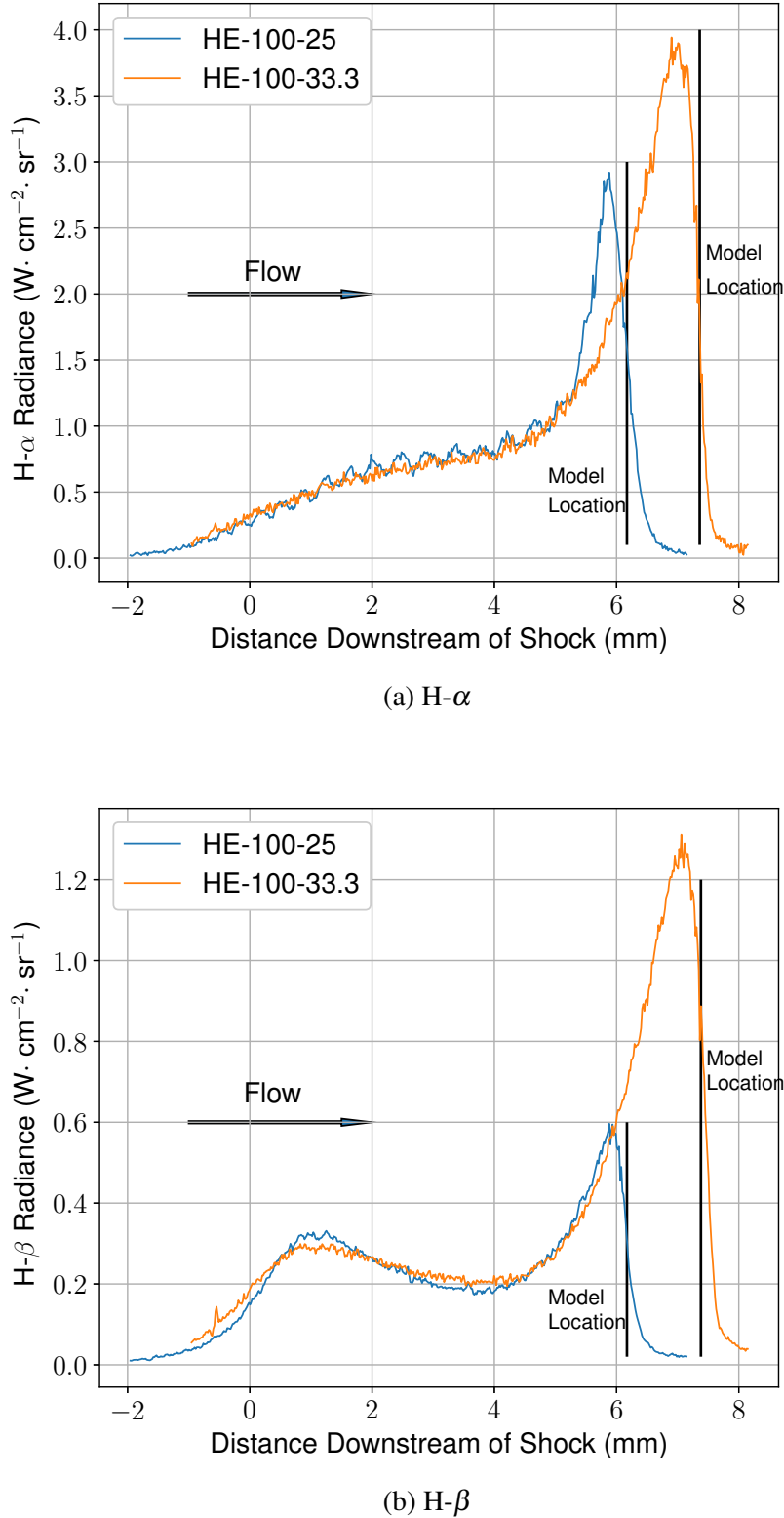


Figure 4.7: Radiances profiles along stagnation streamline using different radii models for the helium condition.

EAST [20]. In the rapid radiance increase region, the velocity gets close to zero and allows further ionization to occur. Due to the building up of the electrons, electron impact ionization would be more significant in this region comparing to the region near the shock front. Such electron impact ionization

processes will lead to the depletion of the upper electronic states. Since the channels of communication between high and low-lying bound electronic states are relatively inefficient, the state distribution would be no longer Boltzmann [46]. This could be the reason of the more depleted H- $\beta$  emission at the rapid increase region, as H- $\beta$  is from the transition from an upper state ( $n = 4 \rightarrow 2$ ) comparing to H- $\alpha$  ( $n = 3 \rightarrow 2$ ).

Thus, Fig. 4.7 gives an example of how the radiance profile would be if there is more room (large binary scaled shock standoff distance) for relaxation. As the relaxation generated by the neon condition is further than generated by the helium condition, in Fig. 4.6a and Fig. 4.6b, the difference of the velocity distribution along the scaled distance axis would lead to the discrepancies. When there is more room for further relaxation when using the helium condition, there will be a less rapid increase for H- $\alpha$  when the electron-atom impact ionization occurs. Hence, when there is more room for relaxation, the H- $\alpha$  radiance profile in the helium condition will increase less rapidly after 18 Pa·s, and would have a better qualitative agreement with the profiles using the neon condition. Similarly, the H- $\beta$  radiance will still match if there is more room for relaxation for the helium condition cases. This gives a quantitative validation of the successful recreation of the relaxation using the scaling method.

It is also noted that after being scaled by  $P_f$ , the scaled H- $\alpha$  radiance in the neon condition is significantly lower than that in the helium condition. This is possibly due to the stronger H- $\alpha$  self-absorption in the neon condition experiments than in the helium condition experiments. According to the Beer-Lambert law, in the optically thick case, the absorbency  $A$  of a gas is a function of the molar concentration of the attenuating species ( $c$ ), with a molar absorption coefficient ( $\varepsilon$ ) and path length ( $l$ ) through the absorbing gas:

$$A = \varepsilon cl \quad (4.21)$$

The molar absorption coefficient ( $\varepsilon$ ) is an absorbance dependent property and is a measure of how strong an absorbance is at a particular wavelength of light. In the neon condition experiments, higher post-shock pressure leads to a higher molar concentration. Thus the self-absorption for H- $\alpha$  emission in the neon condition is stronger than in the helium condition.

When comparing the radiance profiles of different transitions using the same condition, the variation of absorbency is due to the variation of the molar absorption coefficient  $\varepsilon$ . The scaled H- $\beta$  radiance profiles using different conditions did not show variation, whereas the scaled H- $\alpha$  radiance in the neon condition is lower than in the helium condition. This experimentally shows that the absorption coefficients for H- $\beta$  absorption are much weaker than H- $\alpha$ .

#### 4.4.4 High Speed Imaging

Filtered high speed images of the radiating flow were also obtained separately using two narrow bandpass filters in front of the high speed camera. Andover corporation filters 656FSX10-50 and 486FSX10-50 were used to capture the radiance from a wavelength region with a center wavelength of 656 nm (H- $\alpha$ ) and 486 nm (H- $\beta$ ) respectively and with a 10 nm bandwidth. The H- $\alpha$  and H- $\beta$  filtered images in the test time are shown in Figs. 4.8 and 4.9 respectively. Note that for the images from the

neon condition experiments, the bright regions near the body were saturated as a small f-number was chosen for the camera to capture the relatively dimmer immediate post-shock region. In Fig. 4.8b, the bright region beneath the model is also due to the saturation of the camera. These images can be used for the comparison with CFD results, in terms of shock standoff and shock shape comparison; whereas, shock layer relaxation can only be compared with the helium condition images.

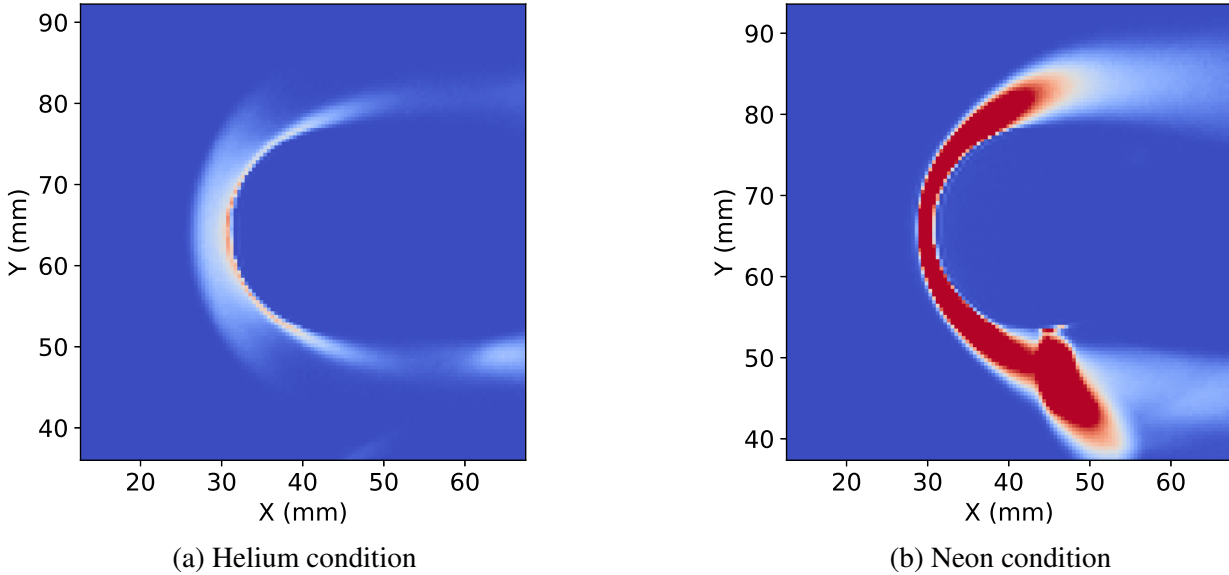


Figure 4.8: H- $\alpha$  filtered high speed images in the test time.

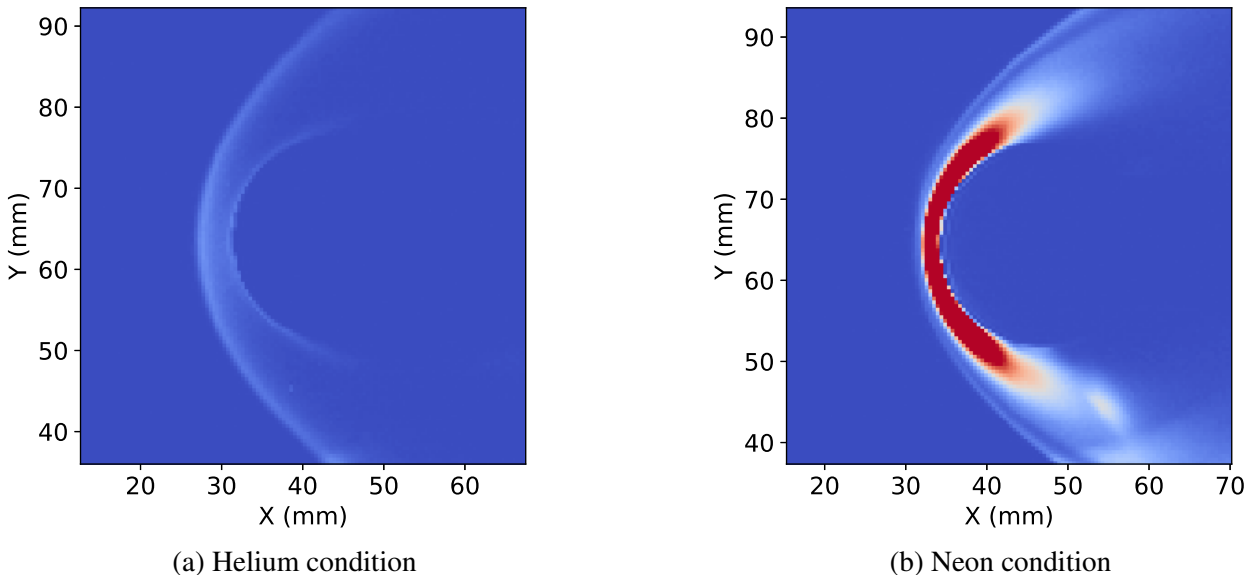


Figure 4.9: H- $\beta$  filtered high speed images in the test time.

High speed images provide a more direct comparison for the two-dimensional emission around the test model. For both H- $\alpha$  and H- $\beta$  transitions, the radiative field generated by these two conditions are very similar; whereas, the features are more compressed and the strong emission area near the

body is larger in the neon condition. These are consistent with the stagnation streamline spectroscopic data, and again show that the designed neon condition based on the substitution theory can generate a similar but more compressed non-equilibrium flow compared to the target helium condition.

## 4.5 Conclusions

A non-equilibrium flow scaling method for giant planet entry using H<sub>2</sub>/Ne to substitute H<sub>2</sub>/He as the test gas is presented and experimentally validated. The use of Ne rather than He as the heavy particle collision partner did not change the hydrogen thermochemical relaxation behavior, such as dissociation, ionization, and radiation. Hence the substitution is a valid way to study these processes. With a lower specific heat, H<sub>2</sub>/Ne mixtures require less energy addition to achieve the same post-shock temperature as in the H<sub>2</sub>/He mixtures. This is the main requirement for generating flow relaxation similarity.

Analytical modeling of the chemically non-equilibrium flow for H<sub>2</sub>/Ne and H<sub>2</sub>/He mixtures shows that hydrogen mole fraction  $r$ , post-shock temperatures  $T_f$  and  $T_i$ , and the ratio between P/V which controls the chemical reaction timescale with respect to convective transport, are the key factors to achieve the similarity of the relaxation rates along a streamline. If the post-shock temperatures  $T_f$  and  $T_i$  of the target condition have been recreated, binary dissociation and ionization rates, before recombination becomes significant, will be recreated along the scaled coordinate  $(1 - r)x\frac{P_f}{V_f}$ . Based on this, a condition using H<sub>2</sub>/Ne as the test gas was designed targeting an existing H<sub>2</sub>/He Saturn entry condition. This designed neon condition duplicates  $r$ ,  $T_f$ , and  $T_i$  of the target helium condition, with a lower freestream velocity and higher pressure. Thus, it is a scaled condition for the target helium condition.

Experimental validation of the scaling method was conducted by testing the helium condition and the neon condition with cylindrical test models. H- $\alpha$  and H- $\beta$  spectral lines in the stagnation region were identified and interpreted for relaxation comparisons. Quantitative agreement was observed in the scaled H- $\beta$  radiance along the scaled coordinate  $(1 - r)x\frac{P_f}{V_f}$ , whereas discrepancies were observed on the scaled H- $\alpha$  radiance profiles. This is because different velocity distributions were generated in the flow with different binary scaled shock standoff distances, and this effect varies between H- $\alpha$  and H- $\beta$  because of the non-Boltzmann feature of the flow. In the experiments with a test model, the decrease of the velocity allows more time for further relaxation, and this effect will become significant when the flow gets close to the wall. To recreate the velocity distribution along the scaled coordinate, same binary scaled shock standoff distance is required to be generated by the helium and neon conditions. In this paper, it is also experimentally shown that when the binary scaled shock standoff distance generated by these two conditions becomes similar, there will be quantitative agreement in both H- $\alpha$  and H- $\beta$  radiance profiles, which successfully validates the scaling method. Consistent with the spectroscopic data, similarities in H- $\alpha$  and H- $\beta$  filtered images were also found using these two conditions, and again validated the scaling method in terms of the whole radiative field recreation.

In this study, the helium condition, which targets Saturn entry at the upper-performance edge of X2, can be substituted with a scaled neon condition which employs the facility's least powerful driver

condition. This shows that, using the neon substitution, the facility's performance envelope can be extended to higher equivalent flight speeds, and considerable facility performance is left for further scaled testing. Based on this work, more scaled tests for giant planet entry study can be conducted in X2 or other impulse facilities, so that an extensive dataset can be generated to assist numerical model validation and development in the future.



## Chapter 5

---

# Electron Number Density Measurements in a Saturn Entry Condition

---

**Reproduced entirely from a manuscript submitted to the AIAA Journal:**

Yu Liu, and Christopher M. James, and Richard G. Morgan, and Peter A. Jacobs, and Rowan Gollan, and Timothy J. McIntyre, “Electron number density measurements in a Saturn entry condition,”

*Submitted to AIAA Journal.*

See *Submitted manuscripts included in this thesis* in the preamble of this thesis for a statement of the author contributions to this paper. The introduction of facility has been cut off to avoid overlapping contexts among chapters.

### Abstract

The aerodynamic heating experienced by capsules entering into the atmospheres of Saturn, Uranus, and Neptune is greatly affected by chemically non-equilibrium processes occurring in the shock layers. There are several reaction schemes available in numerical predictions for hydrogen dissociation and ionization, and more experimental data would assist verifying these existing models. This paper reports the results of electron number density measurements conducted in the X2 expansion tube at the University of Queensland using a condition representative of a proposed Saturn entry where significant non-equilibrium effects in the shock layer are expected. Electron number density along the stagnation streamline was obtained from Stark broadening. The data presented here provide independent measurements for evaluating the reaction schemes for the conditions created. It was found that the experimental data were qualitatively modeled by a contemporary kinetic model. Quantitative agreement between experimental and numerical data was found by adjusting the ionization rate coefficients from an existing reaction scheme by a factor of 25. This updated reaction rate set was also cross-validated with electron number density measurements in NASA’s shock tube tests, and a satisfying agreement was found.

## 5.1 Introduction

Atmospheric probes to all four giant planets—Jupiter, Saturn, Uranus, and Neptune—have long been of interest for the science community. In 1995, the Galileo probe entered the atmosphere of Jupiter with an entry velocity of 47.4 km/s [17]. The heat load during the entry is the most severe for the probe missions that humankind has ever performed. More recently, the Cassini spacecraft, which carried the Huygens probe, was sent to explore the Saturnian system for 13 years and ended its journey by diving into Saturn’s atmosphere in 2017, which laid the groundwork for a future Saturn atmospheric probe. After these missions, there is a growing interest for further exploration of these giant planets, especially for Uranus [30] and Neptune, which are believed to have liquid oceans beneath the atmosphere and have never been explored in detail [26].

When designing the heat shields which protect spacecraft during the entry into the atmosphere of Saturn and Uranus, large uncertainties remain in the aerodynamic heating prediction [25]. Accurate modelling of catalytic wall effects and transport properties is required to accurately predict convective heating, while chemical non-equilibrium processes are important for simulating the heating environment in trajectories where radiative heating is significant [25]. Major chemical reactions involved in these entries are the dissociation of H<sub>2</sub> and the ionization of H atoms. Dissociation of H<sub>2</sub> is firstly initiated by H<sub>2</sub>-H<sub>2</sub> and H<sub>2</sub>-He collisions, then the collisions between H<sub>2</sub> and other generated particles (H, H<sup>+</sup>, e<sup>-</sup>). In the literature, kinetic schemes for H ionization include one-step and two-step mechanisms [94]. H atoms lose their electrons directly after collisions in the one-step mechanism, while in two-step ionization the bound electrons inside H atoms will be excited to higher levels first and then subsequently be freed by further collisions.

In 1973, Leibowitz investigated the chemical reaction scheme in H<sub>2</sub>/He mixtures via emission measurements in an electric arc driven shock tube. A reaction scheme including hydrogen dissociation and ionization was proposed in this work [14]. However, it was found that the radiating driver gas [55] in the facility used by Leibowitz [14] could result in errors in the proposed rates [40]. Subsequently, shock tube measurements with higher shock speeds were conducted by Leibowitz and Kuo [15] in an ANAA shock tube with a modified arc driver. Lower dissociation and ionization rate coefficients than in the previous study [14] were obtained. Stalker [16] examined both sets of ionization rates in a non-reflected shock tube by using interferometry to obtain species number densities in a hydrogen-neon mixture and comparing them with numerical predictions. It was found that comparing to the rates in Leibowitz [14], the species number density predictions by using the rates in Leibowitz and Kuo [15] agreed better with the measured post-shock relaxation data.

Apart from Leibowitz’ and L&K’s chemical kinetic models, there were several other models developed to describe chemically reacting H<sub>2</sub>/He mixtures. Boyd [39] summarized the reaction rates from the NIST Chemical Kinetics Database [95] and low temperature plasma experiments [96]. A DSMC simulation of the low power arc jet test was then conducted, and compared with experimental measurements of temperature and species number densities on the flow across the nozzle exit. The comparison between DSMC simulation and experimental measurements showed that this model

captured the translational temperature, H<sub>2</sub> number densities, and velocity distributions well. The H number density was under-estimated by 3-4 times, whereas the electron number density was over-estimated by an order of magnitude. The analysis in this paper [96] shows that chemical reaction model was not supposed to be the source of the disagreement. Another set of hydrogen dissociation and ionization rate can be found in a chemical kinetic model for earth entry [97]. These rates were then used to numerically investigate the Galileo probe ablation [38]. However, only the electron-impact ionization rate was included in this rate set, and there is a lack of hydrogen ionization mechanisms to produce the initial electrons. Furthermore, Park [40] assembled the latest chemical kinetic models, including the dissociation models from Kim et al [98, 99] and an ionization model that describes the rates for H excitation to the first excited state and to other excited states separately. It was confirmed that, by adjusting the rate coefficients, the ionization model proposed by Leibowitz and Kuo [15] can correctly simulate the experimental data of Leibowitz [14] and Livingston [56]. This model has been used by Furudate and Michiko [68]. In the literature, Leibowitz and Kuo's model [15] is the most commonly used one for non-equilibrium giant planet entries, and has been adopted in Refs. [21, 25, 37, 57]. It should be noted that in the work of Santos Fernandes et al. [37], the original reaction rate coefficients [15] which were originally given in cgs units were interpreted in SI units. Therefore, the rates were interpreted two orders of magnitude lower than the correct values. Furthermore, Santos Fernandes et al. [15] has omitted the rate with lowered activation energy that is assigned to the two-step ionization process.

The proposed entry velocity and density for Saturn and other giant planet entries are beyond the performance envelopes of most impulse facilities. Thus, there have been very few relaxation rate measurements conducted of representative gas giant entry conditions. In addition to the measurements made in 1970s [14, 56], shock layer radiation was measured in NASA's EAST facility [20] and in the UQ's X2 expansion tube [45]. The X2 data were obtained in a H<sub>2</sub>/Ne shock layer with a post-shock frozen temperature exceeding 40000 K, where the polynomial fitting [100] that is commonly used to determine thermodynamic properties will be invalid. EAST's measurements were conducted in simulated Saturn and Uranus entry conditions. Shock layer radiation as well as electron density profiles were obtained. EAST's data have been compared with a DSMC simulation [21]. It was found that the experimental radiation data can be only qualitatively reproduced, and the trend of electron number density was not correctly simulated. This suggests that further investigations of reaction models are required for successfully rebuilding the experimental measurements. More recently, a physically-based state-to-state chemical kinetics of the H<sub>2</sub>/He mixture was proposed [41] with an alternative path to ionization. The proposed chemical kinetics was then validated against EAST's data [20], and good agreement was found in temperature and electron number density comparison between experimental data and numerical simulations.

Expansion tubes can generate these flow conditions over scaled test models, allowing post-shock radiation measurements to be made. This makes X2 a powerful tool in terms of generating relaxation data in a blunt body shock layer. However, it is not possible to recreate the post-shock radiation of the proposed Saturn entry in X2 using the gas composition representative of Saturn's atmosphere

(89%/11% H<sub>2</sub>/He by volume). In earlier studies [1, 2, 23], the non-equilibrium processes during a proposed Saturn entry shock layer were found to be able to be simulated by increasing the mole fraction of helium to 80% (by volume) in the test gas in X2. As a highly non-equilibrium flow with a slow ionization was observed, it can be a useful test case for chemical model validation. This Saturn condition was used in the current study for electron number density measurements.

Emission spectroscopy is a useful diagnostic technique for quantifying the radiative field in the shock layers. The measured spectral lines emitted by the test gas can be broadened in many ways, such as Doppler broadening caused by the random motion of the emitting species particles and Stark broadening due to the presence of charged particles. Broadened line widths of these effects are functions of transition type, translational temperature of species, electron number densities, and other factors. Thus, the measured spectral line profiles can be used to obtain flow properties such as the electron number density. However, relating the externally recorded signals to the internal source flux is a complex task, as the measured signals are strongly dependent on edge effects and self-absorption. If the flow field is perfectly two-dimensional and the gas is transparent to the photons, the recorded radiance will increase linearly with the optical path length. However, the hydrogen gas, especially in high-temperature conditions, tends to be optically thick and not fully transparent to photons, so that the photons can be re-absorbed by the radiating gas before they escape. This will lead to lower recorded emission intensities than otherwise expected [101, 102]. Also, self-absorption will flatten the spectral line, thus broadening the hydrogen line profile and adding to the uncertainties for a broadening effect analysis. For a given flow condition, self-absorption is a function of the transition type and the optical path length. Hence, a careful selection of the transition and the model length is required for spectral line profile measurements.

The goal of this study was to obtain the electron number density data in a representative Saturn entry condition to provide a new test case for numerical validation. In this paper, three cylindrical models with identical radii (12.5 mm) but with varying lengths (50 mm, 75 mm, and 100 mm) were used as the test models to generate shock layers with varying optical path lengths for radiation measurements using the selected Saturn entry condition. Spectroscopic data were analyzed to identify the most suitable transition and model length for broadening analysis. Then, broadening analysis was performed on the spectroscopic data to calculate the electron number density along the stagnation streamline. The obtained experimental data were compared with numerical predictions using varying chemical reaction models from the literature to validate and improve the current numerical models.

## 5.2 New Experimental Measurements in X2

The experiments were performed in the X2 expansion tube at the University of Queensland. Introduction of X2 facility can be found in Chapter 3.

### 5.2.1 Test Models and Optical Configuration

Compared to a three-dimensional (3D) model such as a spherical model, nominally two-dimensional (2D) cylindrical models have the advantage of enabling radiation to be measured along the line-of-sight of a nominally uniform flow field, so that optical measurements can be accurately correlated to specific well-qualified observation points. Hence, the shock layer measurements with nominally 2D models is easier to be numerically rebuild.

However, radiation measurements are influenced by edge effects created by finite aspect ratios (ratio between cylinder length and diameter), as is shown in Fig 5.1 in which circle of confusion is ignored. In general, a nominally 2D flow field will have 3D regions of flow superimposed on a 2D flow in the core region. Supposing the aspect ratio of the model is high enough, the non-uniform edge effects area may be ignored, and the measured signals can be considered to be the integrated value along the lines-of-sight (optical path length) in a genuine 2D flow.

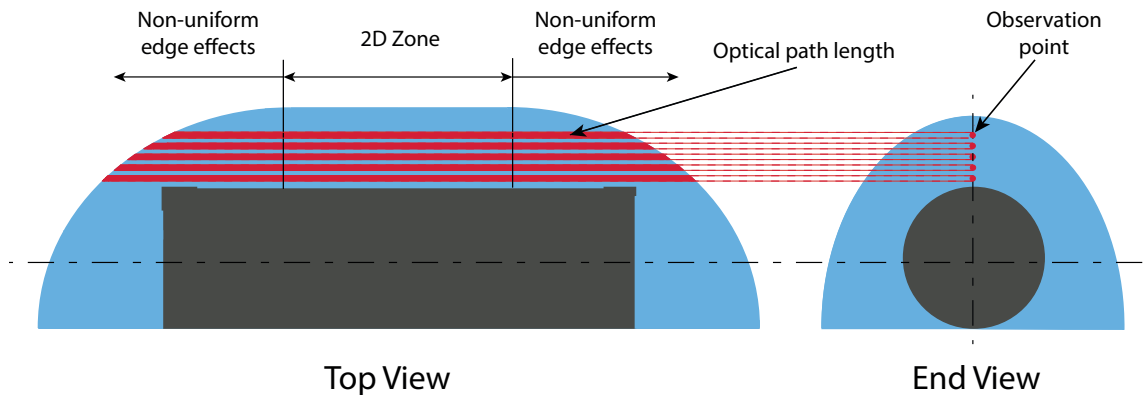


Figure 5.1: Line-of-sight through shock layer and the 2D projected plane of cylindrical model (ignoring circle of confusion).

For a chosen model radius, the aspect ratio can not be arbitrarily large. In the optically thick case, for a certain flow condition, the absorbency  $A$  of a gas is a function of the molar concentration of the attenuating species ( $c$ ), with a molar absorption coefficient ( $\epsilon$ ) and optical path length ( $l$ ) through the absorbing gas according to the Beer-Lambert law [103]:

$$A = \epsilon cl \quad (5.1)$$

The molar absorption coefficient ( $\epsilon$ ) is an absorbance dependent property and is a measure of how strong an absorbance is at a particular wavelength of light. When the optical length increases, the absorbency of the radiating gas will become larger. Thus, careful selection of the test model's size and the transition is required to avoid significant self-absorption while keeping the aspect ratio as large as possible to reduce the associated edge effect.

The test models used in this study are cylinders with identical radii of 12.5 mm, and lengths of 50 mm, 75 mm, and 100 mm, giving aspect ratios of 2, 3, and 4 based on diameter. Both radiation along the stagnation streamline and shock shapes were measured using these three models to investigate which is most suitable for the electron number density measurements.

The optical arrangement used for the experiments is shown in Fig. 5.2. On one side of the test section, a Shimadzu HPV-1 high-speed camera with a Nikon Zoom-NIKKOR 100-300 mm lens is mounted. The optical emission spectroscopy system that includes an imaging spectrometer with a camera sensitive in the visible and near-infrared wavelength range, and supporting optics is placed on the other side. In this study, the spectra were obtained viewing along the axis of the cylinder to get spectroscopic data along the stagnation streamline (shown in Fig.5.3a); whereas the high-speed images were obtained with the high-speed camera imaging viewing perpendicular to the axis of the cylinder to image the shock shape (shown in Fig.5.3b, the model edge has been marked with black lines). With this spectroscopic system set-up, the circle of confusion was calculated to be 0.087 mm. In each experiment, the model was set up in one orientation for either high-speed image or spectroscopic measurements. In Fig. 5.2, the model was set up for spectroscopic measurements, and the slit of the spectrometer was focused on the stagnation streamline.

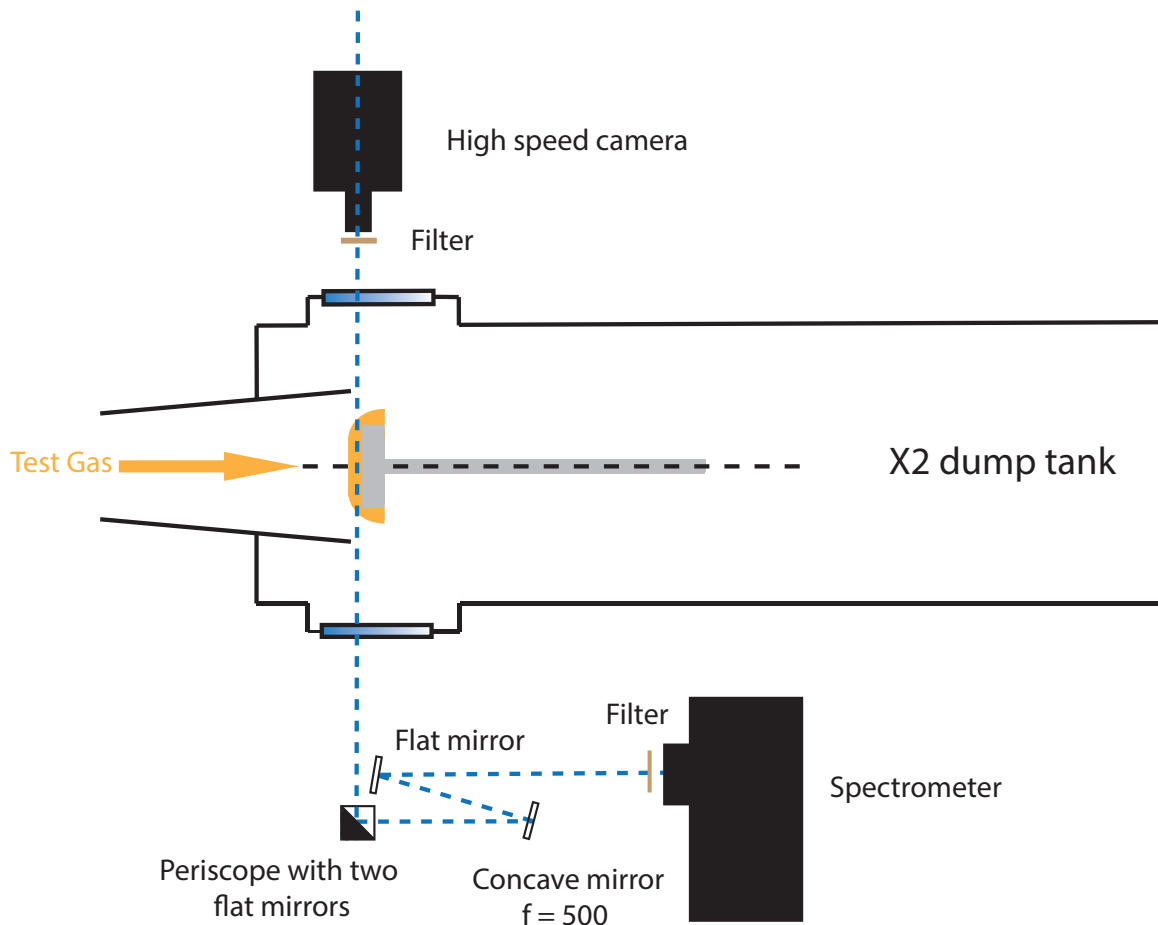


Figure 5.2: Schematic of the optical arrangement with the spectrometer looking along the axis of the model (not to scale).

### 5.2.2 Flow Condition

The test condition used in this work with H<sub>2</sub>/He as the test gas was designed by James et al. [23], and its details are listed in Table 5.1. This condition employs a higher fraction of helium in the

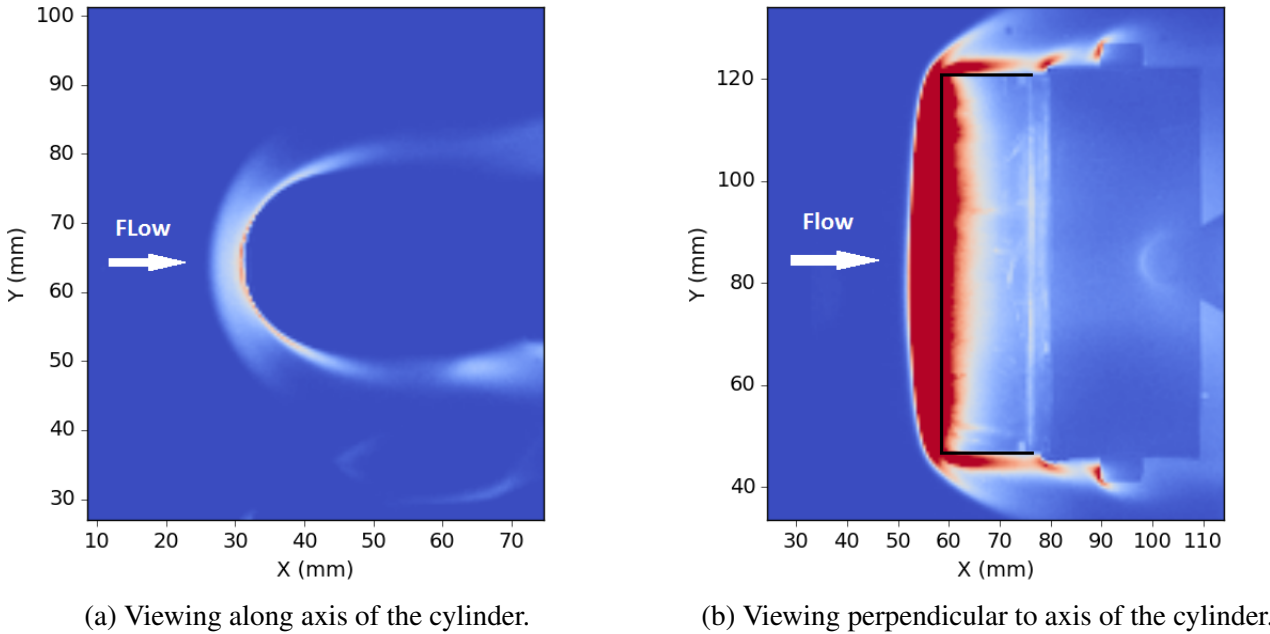


Figure 5.3: Two orientations of the measurements on the model.

test gas than in Saturn’s atmosphere, and has been experimentally shown to be able to simulate a representative non-equilibrium shock layers for Saturn entry [1,2]. In the authors’ previous works [1,2], radiative emission generated by this condition was measured, and evidence of a delayed ionization was presented.

Table 5.1: Details of the test condition.

Driver condition designation	X2-LWP-2.5 mm-0
Primary driver fill condition	77.2 kPa 100% helium
Orifice plate diameter	65 mm
Primary diaphragm	1 x 2.5 mm thick cold rolled steel, scored diaphragm
Rupture pressure	35.7 MPa
Shock tube fill condition	2.0 kPa 80%/20% (by volume) helium/hydrogen
Secondary diaphragm	1 x $\approx 14 \mu\text{m}$ thick aluminum foil diaphragm
Acceleration tube fill condition	0.5 Pa air

In this paper, the data from seven experiments are presented. An experiment was performed for each orientation and each aspect ratio, giving a total of six experiments. These experiments were performed with a 150 gp/mm grating, giving a wavelength range of 400–690 nm which includes important hydrogen atomic emission from H- $\alpha$  (656 nm) and H- $\beta$  (486 nm). Another experiment was conducted to obtain the highly-resolved H- $\beta$  spectral line profile with an 1800 gp/mm grating using the model with an aspect ratio of 3. The mean and standard deviation values of these seven experiments’ flow properties are listed in Table 5.2. Shock speeds in the shock tube and the acceleration tube were measured quantities from experiments. The freestream conditions were numerically calculated based on the shock speed measurements using PITOT [24], which is an in-house flow condition simulation tool for expansion tubes based on compressible and isentropic flow relations. The post-shock flow

properties were calculated by the one-dimensional post-shock flow analysis code Poshax [80, 81], with the free-stream flow properties as the input.

Table 5.2: Details of flow properties.

Measured shock speeds	Mean	Standard Deviation
Shock tube (m/s)	8480	70
Acceleration tube (m/s)	18700	200
<hr/>		
Freestream condition		
Temperature (K)	400	20
Pressure (Pa)	60	10
Velocity (m/s)	18700	100
Mach number	15.4	0.5
Density (kg/m <sup>3</sup> )	$6.7 \times 10^{-5}$	$0.6 \times 10^{-5}$
Total enthalpy (MJ/kg)	175	3
<hr/>		
Post-shock frozen state		
Temperature (K)	26800	400
Pressure (Pa)	18000	1000
Velocity (m/s)	14400	100
Density (kg/m <sup>3</sup> )	$2.9 \times 10^{-4}$	$0.2 \times 10^{-4}$
<hr/>		
Post-shock equilibrium state		
Temperature (K)	12220	30
Pressure (Pa)	20000	1000
Velocity (m/s)	16300	100
Density (kg/m <sup>3</sup> )	$5.4 \times 10^{-4}$	$0.4 \times 10^{-4}$

### 5.2.3 Self-absorption Investigation

#### High speed imaging

High-speed imaging was obtained with the camera focused normal to the axis to observe the shock shape on the cylindrical models with varying aspect ratios. Fig. 5.4 shows false-color images of the recorded radiating shock layer during the test time, with the profile of the model marked as black lines.

The Canny edge detection method [78] was used to identify the shock shapes so that the distances between the model edge and the shock (shock-model distance) along each cylinder can be obtained. The results are plotted in Fig. 5.5.

The roughness in the plot in Fig.5.5a is due to the resolution of the high-speed camera. The uncertainty of shock location is estimated to be two pixels (around 1.2 mm) as shown in the figure. This is because the shock front can be smeared by circle of confusion and by the rarefied gas effect. The optical path length along the line-of-sight for each observation point along the stagnation streamline was extracted and normalized by the cylinder's length. The results are shown in Fig.5.5b. Generally, the radiating gas's optical path length for each observation point along the stagnation streamline, after being normalized by the model length, matches well among these three experiments. This agreement means the path length difference caused by varying aspect ratios can be compensated for by normalizing the measured radiance by its model length. It is also worth noting that the normalized

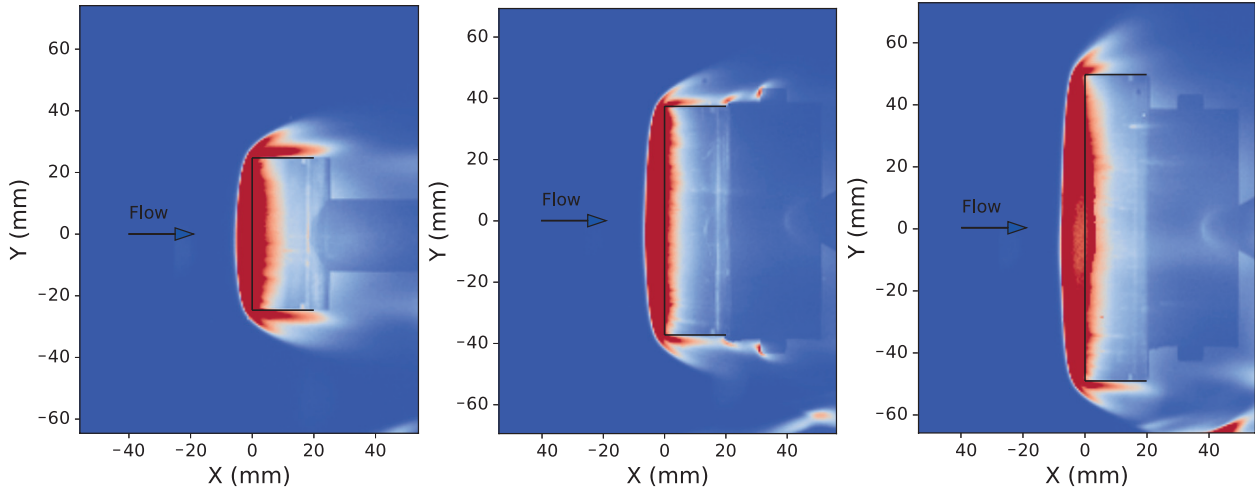


Figure 5.4: High speed imaging in the test time for the experiments with aspect ratios of 3, 4 and 5, with the camera looking perpendicular to the axis of the cylinder.

optical path length in the aspect ratio of 2 case is larger than the other two cases in the region near the model, indicating the edge effect in the aspect ratio of 2 case may be relatively stronger.

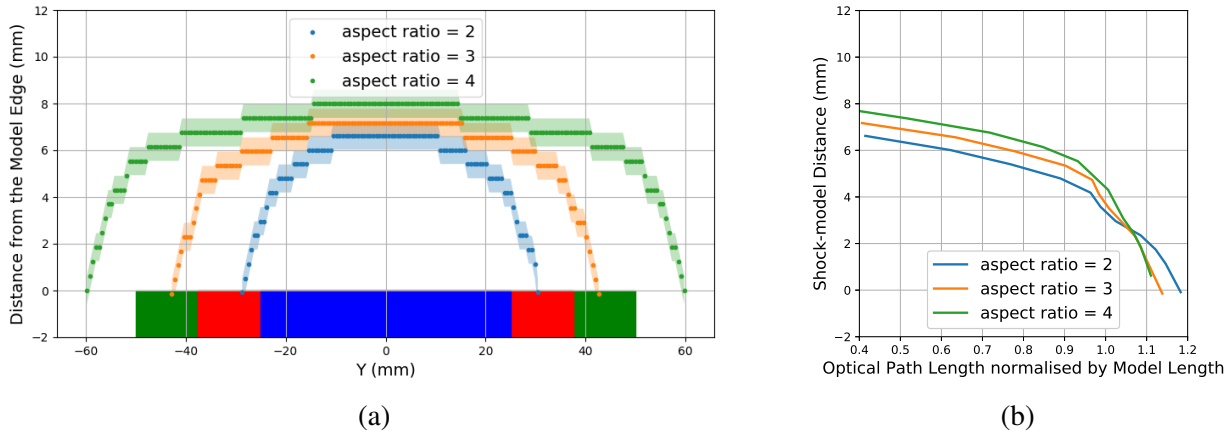


Figure 5.5: (a) Canny edge detected shock shape. (b) Optical path lengths normalized by the model length.

## Spectroscopic data

Spectroscopic data were obtained with the slit of the spectrometer aligned with the stagnation streamline to measure the spatially resolved radiation. An example of the spectroscopic data collected for a model with an aspect ratio of three is shown in Fig. 5.6. The vertical axis shows the radiation data's spatial location, and the estimated shock front is marked as 0, while the horizontal axis shows the wavelength of the diffracted radiation. Flow is from top to bottom. The collected spectra were calibrated on both axes, and the absolute intensity was calibrated using an integrating sphere [84].

The radiance emitted from a specific transition can be obtained by integrating the radiation over a selected wavelength range. Figure 5.7 shows the H- $\alpha$  and H- $\beta$  radiance profiles from the experiments with the coarse grating (150 gpmm). The radiance has been normalized by the model lengths, and the

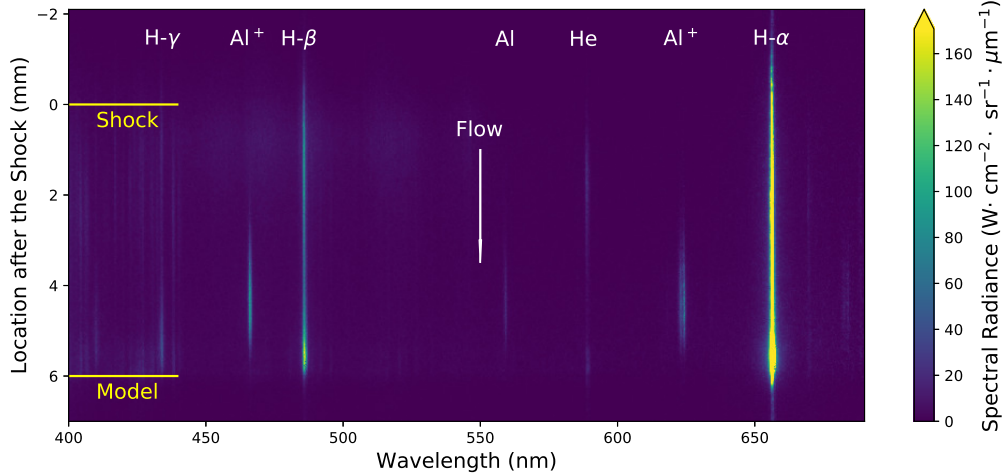


Figure 5.6: An example of calibrated spectral data. Flow from top to bottom, and the estimated shock location is marked as 0.

location axis has been normalized by the shock standoffs. As there is a molecular band overlap with H- $\beta$  range in the immediate post-shock region (at around 1 mm), the radiance contribution from these features has been reduced by averaging the radiation at the two edges of the integration region and subtracting it from the integrated radiance as the background signal. The radiance profile at 1 mm, where the molecular band exists can be found in Fig. 4.4. Also, to minimize the level of noise, a Savitzky-Golay filter was used to smooth the profile. The filter window length for H- $\alpha$  radiance profiles was 0.73 mm; while the length for H- $\beta$  radiance was 0.45 mm. The uncertainty of the radiation measurements was obtained by calculating the coefficient of variation (CV) of the integrated H- $\alpha$  and H- $\beta$  radiance from repeat experiments, and the calculated CV for both transitions is around 10%. This uncertainty is also shown in the figure.

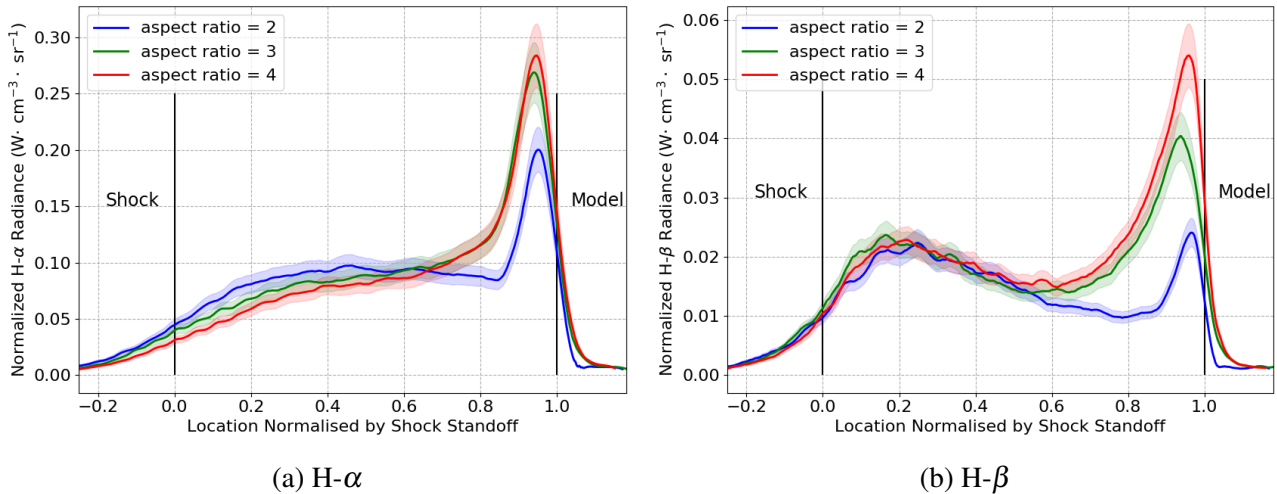


Figure 5.7: Integrated radiance profiles along the stagnation streamline normalized by model lengths.

It is worth noting that both normalized H- $\alpha$  and H- $\beta$  radiance in the aspect ratio 3 and 4 cases statistically match well before the stagnation point, where the radiance drops near the model. Some regions near the shock front where the H- $\alpha$  curves differ by more than the error bars indicate could be

a 3D effect rather than a selfabsorption effect. In contrast, the radiance profile in the aspect ratio of 2 case shows different behaviors with the other two cases. This variation could be due to significant edge effects with the aspect ratio of 2, which has also been seen in the high-speed images. The radiance data show that the model with an aspect ratio of at least three is required to avoid significant edge effects, which is consistent with the result from the study of Eichmann et al. [101] using nitrogen gas. The agreement on both H- $\alpha$  and H- $\beta$  radiance profiles with aspect ratio of 3 and 4 cases indicates that these transitions have negligible self-absorption. Our previous study also found that the H- $\beta$  radiance in this condition increases linearly with pressure, showing that they are probably optically thin [2]. Hence, as a conservative choice to avoid self-absorption, H- $\beta$  spectral lines for the model with an aspect ratio of 3 are used in this paper for broadening analysis.

### 5.2.4 Electron Number Density Calculation

The measured line profiles are a convolution of several broadening effects and thus have finite line widths. As most of these broadening effects are functions of the flow properties such as the translational temperature of heavy particles ( $T_{Tra}$ ) and electron number density ( $N_e$ ), the spectral line shape can be used to diagnose the flow properties of the radiating gas. Specifically, under ionized conditions, the spectral line broadening can be dominated by the broadening effect that is a function of  $N_e$ . In this case, the spectral line profile can be an accurate indicator for  $N_e$ . The hydrogen line shape OES technique for  $N_e$  diagnostics, which is one of the most common methods to obtain  $N_e$  [104], is discussed and applied in this study.

#### Spectral Line Broadening Effect

This section presents an overview of the spectral line broadening mechanisms that can lead to the measured broadened hydrogen spectral lines.

**Natural broadening:** Generally, natural broadening is not the dominant broadening effect for the atomic transition. The FWHM for H- $\beta$  is calculated as  $6.27 \times 10^{-5}$  nm [85].

**Instrument function:** The recorded line profiles will also be broadened by instrument broadening, which is controlled by the optical system setting such as the slit width, grating, ICCD detector, and the focal quality of the optical setup. These effects can be described by an instrument function, which can be fitted by a Voigt function (a convolution of a Gaussian profile and a Lorentzian profile). In this study, the instrument function was experimentally measured using the spectroscopic system to measure the emission from a mercury lamp. The spectrum was measured with a 1800 gpmm grating, and the spectral line profile at 493 nm was fitted with a Voigt profile. The FWHM of the fitted Voigt profile is 0.080 nm, with the Gaussian and Lorentzian contribution to be  $0.056 \pm 0.003$  nm and  $0.039 \pm 0.003$  nm, respectively.

**Doppler broadening:** Doppler broadening is caused by the Doppler effect, which is due to the relative velocity between the emitter and observer generating the shift in the measured wavelength. This broadening effect can be expressed by a Gaussian profile. Doppler broadening is commonly used

to calculate the translational temperature of the heavy particles in the flow. For H- $\beta$ , the FWHM of Doppler broadening can be obtained by [85]:

$$f_{Doppler}[\text{nm}] = 3.39 \times 10^{-4} \sqrt{T_{Tra}[\text{K}]} \quad (5.2)$$

**Van der Waals broadening and Stark broadening:** Apart from the effects above, collisions between emitting particles and other particles will also disturb the emission, thus affecting the line profile. The influence becomes important in the high-pressure conditions so that it is called pressure broadening. The three types of pressure broadening effects: resonance broadening, Van der Waals (VdW) broadening, and Stark broadening are due to the collisions with "like" neutrals, "unlike" neutrals, and charged particles, respectively. For H- $\beta$  line, when  $N_e$  is low ( $\leq 10^{21} \text{ m}^{-3}$ ), resonance broadening is usually negligible [105]. Hence, this paper only focuses on VdW broadening and Stark broadening.

The broadening effect caused by VdW broadening can be described using a Lorentzian profile, and its FWHM can be written as [105]:

$$f_{VdW}[\text{nm}] = 5.925 \times 10^{14} K_1 K_p P[\text{mbar}] T[\text{K}]^{-0.7} \quad (5.3)$$

Here,  $K_1$  and  $K_p$  are the coefficients depending on the transition and the perturber, and their values can be found in the literature [105]. In this study, H- $\beta$  is used for  $N_e$  diagnosis and helium is the inert perturber, Equation 5.3 can be simplified as:

$$f_{VdW}[\text{nm}] = 2.495 \times 10^{-3} P[\text{mbar}] T[\text{K}]^{-0.7} \quad (5.4)$$

Apart from the collisions with neutral particles, the Coulomb's collisions between outer electrons in the emitting atoms and the charged particle collision partners can also alter the emission frequency. This phenomenon is called Stark broadening. The FWHM of Stark broadening is the function of electronic temperature ( $T_e$ ) and number density ( $N_e$ ) of electrons, whereas the effect from  $T_e$  is generally very weak [85]. The FWHM due to the Stark broadening has been tabulated by Touma et al. [106]. For H- $\beta$ , the FWHM can be approximated as [85]:

$$\log_{10} f_{Stark}[\text{nm}] = 0.686 \log_{10} N_e[\text{m}^{-3}] - 15.13 \quad (5.5)$$

This equation is valid when the temperature is 5000-40000 K, and  $N_e$  is within  $10^{20}$ - $10^{25} \text{ m}^{-3}$  [106].

## Spectral Line Fitting Method

In this section, the experimental data using the test model with an aspect ratio of 3 and a fine grating (1800 gpmm) were used for the broadening analysis. For a sufficient signal to noise ratio, 11-pixel rows (0.2 mm) have been binned and averaged for each spectrum along the stagnation streamline. The measured H- $\beta$  line profiles were well-fitted by a Lorentzian profile in most cases. An example fit is shown in Fig. 5.8, and the Lorentzian fitted FWHM as a function of location along the stagnation streamline is shown in Fig. 5.9.

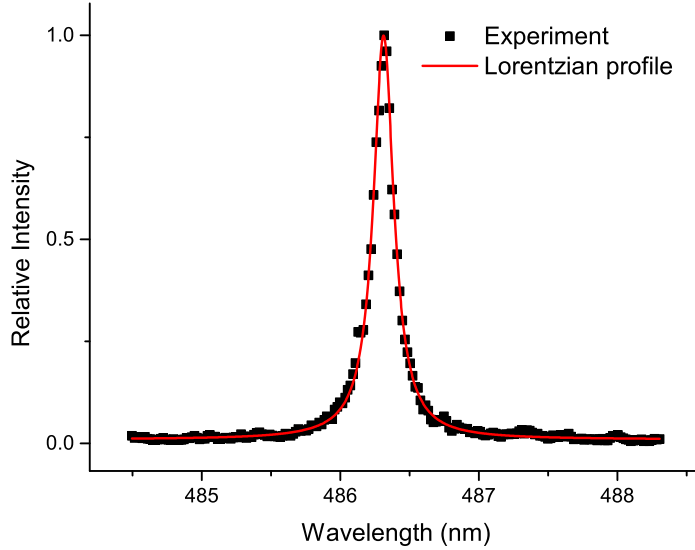


Figure 5.8: Fitted Lorentzian profile for the data measured at 1.49 mm behind the shock.

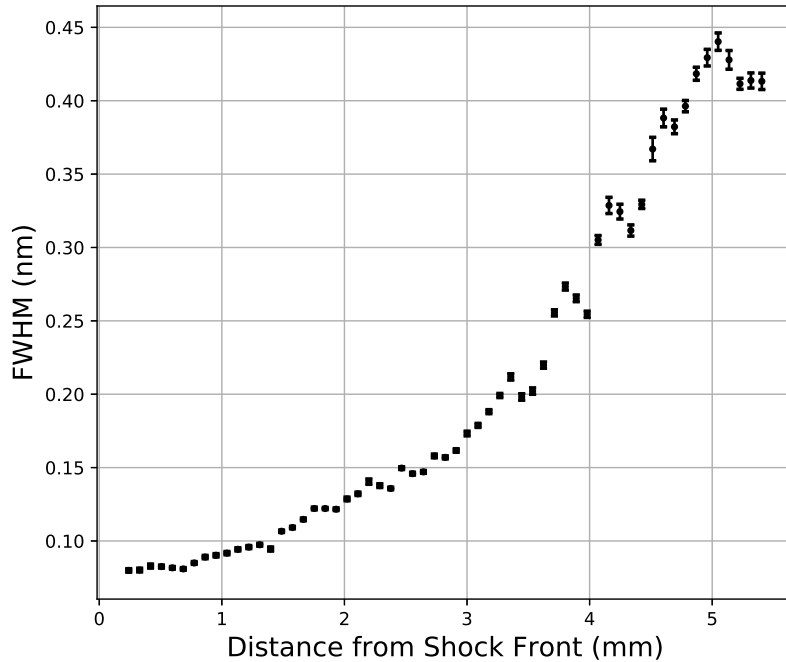


Figure 5.9: Lorentzian fitted FWHM profile along the stagnation streamline.

Before deconvolution, the FWHM contributions of natural broadening, VdW broadening, Doppler broadening, and Stark broadening are compared and shown in Fig. 5.10. Natural broadening and the instrument function are independent of  $N_e$  and the flow condition and their FWHMs are shown as a constant in this figure. The FWHM of VdW broadening is a function of pressure and temperature, while the FWHM of Doppler broadening is a function of temperature. As the shock layer is highly non-equilibrium [1, 2] and the post-shock pressure can be treated as a constant along the stagnation

streamline. The FWHM of VdW broadening and Doppler broadening were calculated using the post-shock frozen pressure and the mean value of frozen state temperature ( $T_f$ ) and equilibrium state temperature ( $T_{eq}$ ). The FWHMs calculated using  $T_f$  and  $T_{eq}$  are shown as the uncertainty. It can be seen in Fig. 5.10 that, for the measured FWHM range in this paper, the dominant broadening features are Stark broadening, Doppler broadening, and instrument function.

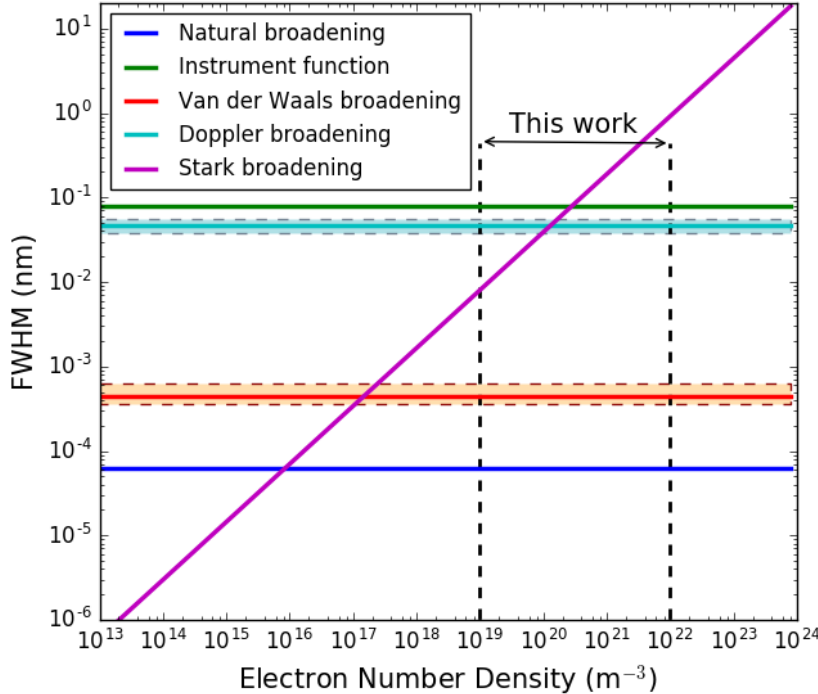


Figure 5.10: Comparison among various broadening effects for H- $\beta$  line broadening.

The measured spectral line profile can be treated as the convolution of the three main broadening mechanisms, and its FWHM can be calculated using the equation [107]:

$$f_V \approx 0.5346 f_L + \sqrt{0.2166 f_L^2 + f_G^2}. \quad (5.6)$$

In this case, the overall Lorentzian FWHM  $f_L$  is composed of Lorentzian feature of instrument function and Stark broadening, while the overall Gaussian FWHM  $f_G$  is composed of Gaussian feature of instrument function and Doppler broadening. As only FWHM due to Stark broadening is unknown, it can be calculated by the Equation 5.6. The convolution of two Lorentzian profiles is also a Lorentzian profile, with the FWHM being the sum of the two original FWHMs. Similarly, the convolution of two Gaussian profiles remains a Gaussian profile, with the FWHM to be the root sum squared value of the two original FWHMs. To calculate  $f_{Stark}$ , the overall Gaussian FWHM  $f_G$  was calculated as the first step by convolving Doppler broadening and the Gaussian feature of instrument function. Then as  $f_V$  is known from the experimental data, the overall Lorentzian FWHM  $f_L$  can be obtained using the Equation 5.6. Finally,  $f_{Stark}$  can be calculated by deconvolving the overall  $f_L$  with the Lorentzian feature of instrument function. The obtained  $f_{Stark}$  can be used to obtain  $N_e$  using Equation 5.5.

## Uncertainty Analysis

The uncertainty of  $N_e$  calculation can be derived from the FWHMs of instrument function, Doppler broadening, and the fitting process. The overall uncertainty analysis was conducted using the method discussed in the work of Moffat [108]. The deviation resulted from the uncertainty for each factor  $f_i$  is calculated as  $\frac{\partial N_e}{\partial f_i} \Delta f_i$ , then the total uncertainty is obtained using:

$$\Delta N_e = \sqrt{\sum_{i=1}^N \left( \frac{\partial N_e}{\partial f_i} \Delta f_i \right)^2} \quad (5.7)$$

## Broadening Analysis Results

After deconvolving the FWHMs of instrument function and Doppler broadening from the measured FWHM, the FWHM of Stark broadening was obtained, and  $N_e$  was then calculated using Equation 5.5. The calculated  $N_e$  profile along the stagnation streamline is shown in Fig. 5.11. It takes about 2.2 mm before the electron number density can be reliably calculated. This is because when  $N_e \leq 10^{20}$ , Stark broadening is not the dominant broadening feature (see Fig. 5.10), also the FWHM approximation for Stark broadening (see Equation 5.5) is not valid.

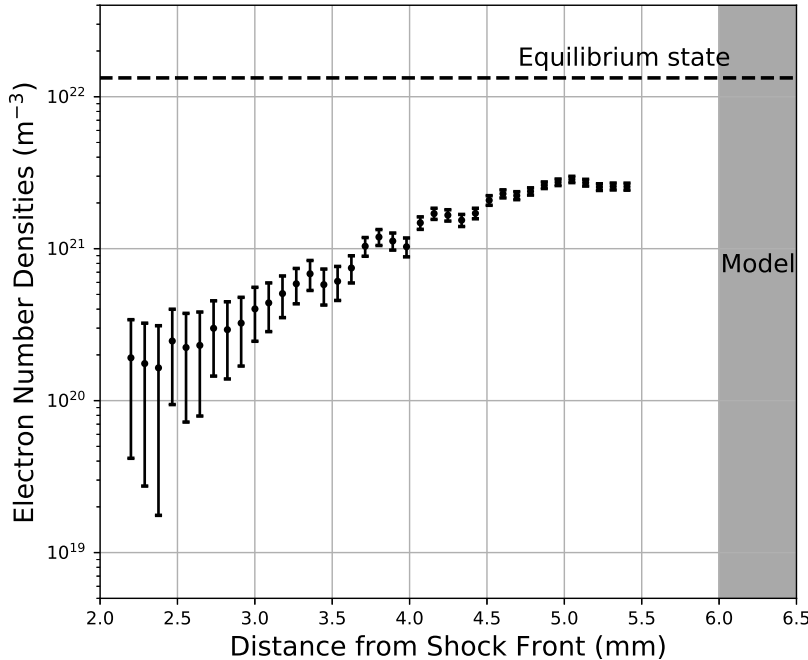


Figure 5.11: Electron number density profile along the stagnation streamline.

For comparison, an equilibrium computation for  $N_e$  at this condition using NASA's CEA program [91, 92] is also shown in Fig. 5.11. At the equilibrium state,  $N_e$  is calculated to be around  $1.3 \times 10^{22} \text{ m}^{-3}$ . The measured electron number density has not reached the equilibrium limit along the stagnation streamline, indicating the flow remains in non-equilibrium or it equilibrates at a lower temperature near the wall.

### 5.3 Computational Fluid Dynamics Modeling and Comparison

The experimental results for  $N_e$  were also compared with numerical predictions using the CFD code Eilmer4 [80, 81]. The numerical predictions were performed to identify which existing chemical reaction model would predict the post-shock chemistry in this condition most accurately. Two sets of forward reaction rates from the literature for hydrogen dissociation and ionization [21, 39] were implemented in Eilmer4 and will be referred to as 'L&K's rates' and 'Boyd's rates'. Backward reaction rates were obtained as the ratio between the forward rates and the equilibrium constants. It needs to be noted that, in L&K's H-e<sup>-</sup> and He-e<sup>-</sup> ionization rates [21], two separate rates exist for one-step and two-step ionizing mechanisms. However, using either one-step or two-step ionization rates was found to result in less than 1.7 times difference in the predicted  $N_e$ . Hence, in this study, only the one-step ionization rates were implemented as 'L&K's rates'.

A recent numerical study on the shock layer generated by the same test condition [109] has shown that there were only slight differences in the simulated species densities and radiation by using one-temperature or two-temperature model. Therefore, A single-temperature model was used in this study. Viscosity was considered to capture the steep gradients in the boundary layer and the shock front.

Two-dimensional viscous simulations were performed to obtain the electron number density profile along the stagnation streamline using the two sets of reaction rates in the literature. The freestream properties in Table 5.2 were used as a uniform inflow in the simulations. For simulations using each set of rates, temporal and spatial convergence was checked based on the electron number density  $N_e$  along the stagnation streamline. It took around 70  $\mu$ s in simulation flow time for each simulation to converge. For each set of rates, spatial convergence was checked by using coarse ( $60 \times 75$ ), medium ( $80 \times 100$ ), and fine ( $100 \times 125$ ) structured grids, which were clustered toward the estimated shock front. An example grid convergence study of the simulations that used L&K's rates [21] is shown in Fig. 5.12. It can be seen that the effect that the grid size has on the calculated electron number density is negligible when using  $80 \times 100$  cells.

The simulated electron number density profiles using the two sets of rates, and the experimental results are shown in Fig. 5.13. Large discrepancies are observed in the electron number density calculated using different reaction rates. The  $N_e$  calculated using Boyd's rates jumps rapidly behind the shock and reaches equilibrium level at around 2.5 mm, while L&K's rates underestimated the measured  $N_e$  profiles. It was found that none of these rate sets can predict the measured  $N_e$  profile well, whereas the results using L&K's rates [21] gave qualitative agreement with the experimental results. This leads to further investigations of the reaction rates. In this work, the original dissociation rates from L&K [21] were maintained, and the ionization rate coefficients were adjusted. Details of the adjusted reaction rates were shown in Table 5.3, and the reaction rates represented using the Arrhenius equation of the form:

$$K_{fd} = AT^n \exp(-E_a/kT) \quad (5.8)$$

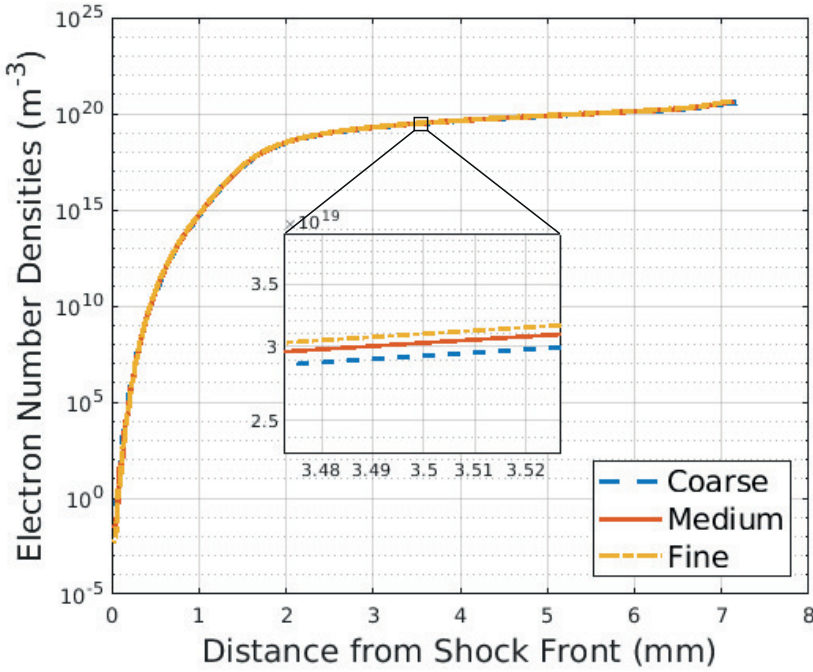


Figure 5.12: An example of a grid convergence study.

Quantitative agreement can be found, as shown in Fig. 5.13, with the L&K's ionization rate coefficients [21] multiplied by 25. This indicates that the kinetic model proposed by Leiwowitz and Kuo [15] can be used to describe this post-shock chemistry, and the electron number density profile can be well modeled by the adjusted chemical reaction model.

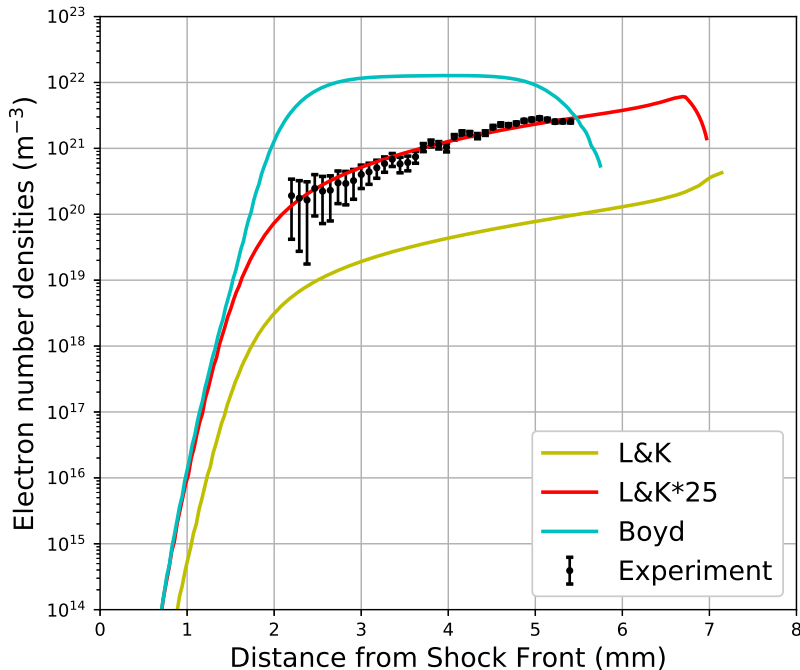


Figure 5.13: Electron number density comparison among experimental results and CFD predictions using two sets of rates.

Table 5.3: Adjusted forward reaction rates for H<sub>2</sub>/He mixtures.

Reaction	A (cm <sup>3</sup> ·mol <sup>-1</sup> ·s <sup>-1</sup> )	n	E <sub>a</sub> /k (K)	Source
H <sub>2</sub> + He $\leftrightarrow$ H + H + He	$4.16963 \times 10^{18}$	-1.0	51958.0465	L&K [15]
H <sub>2</sub> + H <sub>2</sub> $\leftrightarrow$ H + H + H <sub>2</sub>	$1.04000 \times 10^{19}$	-1.0	51958.0465	L&K [15]
H <sub>2</sub> + H $\leftrightarrow$ H + H + H	$8.34649 \times 10^{19}$	-1.0	51958.0465	L&K [15]
H <sub>2</sub> + H <sup>+</sup> $\leftrightarrow$ H + H + H <sup>+</sup>	$8.34649 \times 10^{19}$	-1.0	51958.0465	L&K [15]
H <sub>2</sub> + e <sup>-</sup> $\leftrightarrow$ H + H + e <sup>-</sup>	$8.34649 \times 10^{19}$	-1.0	51958.0465	L&K [15]
H <sub>2</sub> + He <sup>+</sup> $\leftrightarrow$ H + H + He <sup>+</sup>	$4.16963 \times 10^{18}$	-1.0	51958.0465	L&K [15]
H + e <sup>-</sup> $\leftrightarrow$ H <sup>+</sup> + e <sup>-</sup> + e <sup>-</sup>	$5.70585 \times 10^{14}$	0.5	157799.7563	This work
H + H $\leftrightarrow$ H <sup>+</sup> + e <sup>-</sup> + H	$1.54163 \times 10^{12}$	0.5	116099.7877	This work
H + He $\leftrightarrow$ H <sup>+</sup> + e <sup>-</sup> + He	$1.21991 \times 10^{12}$	0.5	116099.7877	This work
He + e <sup>-</sup> $\leftrightarrow$ He <sup>+</sup> + e <sup>-</sup> + e <sup>-</sup>	$3.32715 \times 10^{14}$	0.5	285299.9835	This work

Mole fractions of H<sub>2</sub>, H, and e<sup>-</sup> predicted by using L&K's rates and the adjusted rates are shown in Fig. 5.14. It can be seen that using both rate sets, the dissociation process fully completes at around 3.2 mm behind the shock, while the ionization of H is not fully initiated when the dissociation occurs. In the prediction using L&K's rates, H ionization is negligible and less than 1% H atoms ionizes; whereas using the adjusted rate sets, there are around 10% H atoms ionizing. Also, in the case using the adjusted rate sets, due to the ionization rates are higher than in the other case, the deionization rates are also higher, thus there is a notable electron mole fraction drop near the wall.

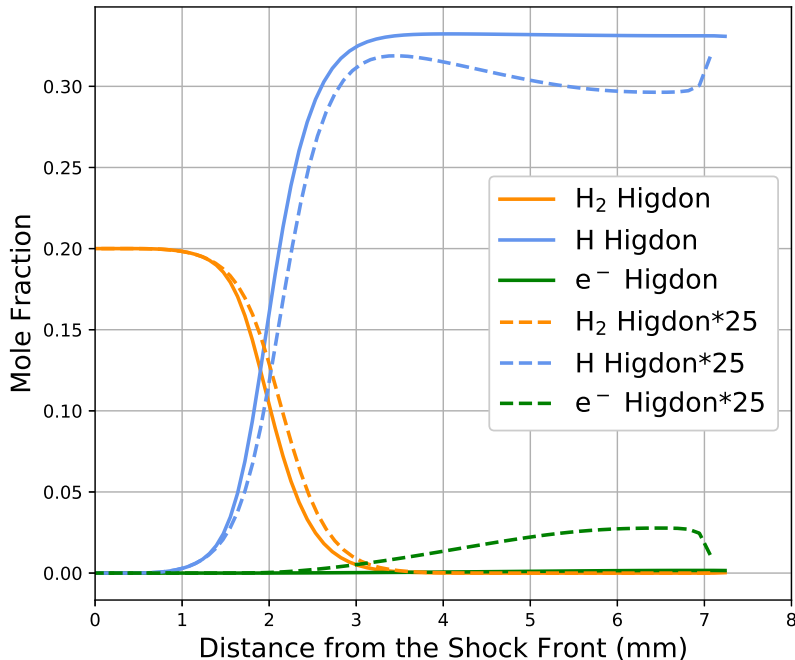


Figure 5.14: Species mole fractions predicted by using L&amp;K's rates and the adjusted rates.

The updated reaction model was also used to simulate the electron number density results from EAST tests for Saturn entry as a cross-validation [20]. In EAST tests, conditions with varying freestream velocities and pressures of 0.1 torr (13.3 Pa), 0.2 torr (26.6 Pa), and 0.5 torr (66.7 Pa) were

tested to obtain the spectroscopic data. Then, at the optically thin cases, Balmer transitions were used to calculate the electron number density based on Stark broadening. The results from 0.1 torr, 0.2 torr, and 0.5 torr conditions were shown in Fig. 5.15, Fig. 5.16, and Fig. 5.17, respectively. It should be noted that the freestream velocities and pressures in some EAST conditions were very similar, and uncertainty of some electron number density results can be relatively high due to the spectral line profiles being close to the instrument function, or optical thickness being observed. Therefore, representative electron number density data were selected and shown here.

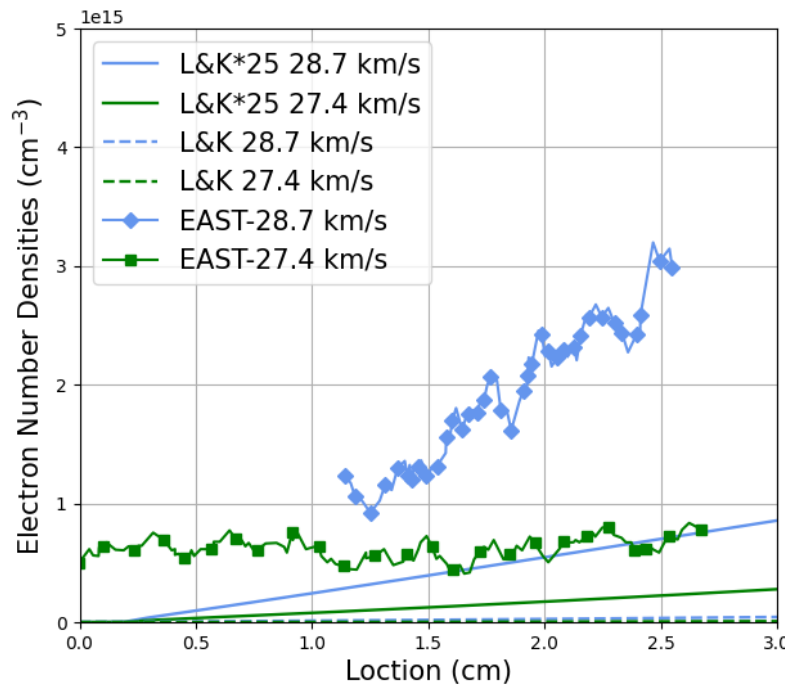


Figure 5.15: Comparison between EAST data and Eilmer simulation results in 0.1 torr conditions.

These experimental results were also compared with the electron number density results calculated by Eilmer4 [80, 81] using the updated reaction model and the original L&K's rate [21]. Eilmer4 simulations were performed on a 0.5 m radius cylindrical body to generate a shock standoff of around 10 cm, which is sufficiently large to neglect the effect by the presence of the body, and the stagnation line can be representative of the region of relaxation. Eilmer4 results of the  $N_e$  profiles in these chosen EAST conditions are also shown in Fig. 5.15, Fig. 5.16, and Fig. 5.17. Some of the EAST data early in time were omitted from the plot where they are at the detection limit of the diagnostic. It can be seen that the simulated  $N_e$  using updated rate set had generally better agreement with the EAST data compared to the original L&K's rate set. For the 0.1 torr conditions, the updated rate set underestimated the measured  $N_e$  and did not predict the  $N_e$  increase after 1.5 cm in the 28.7 km/s condition. For the 0.2 torr conditions, the measured  $N_e$  at 27.8 km/s and 26.3 km/s were very close after 2.4 cm; whereas the predicted  $N_e$  profiles using the updated rate set had around two times discrepancies. Again the  $N_e$  increases after 3 cm were not successfully rebuild by the updated reaction model. However, it was also shown in Fig. 5.16 that the measured  $N_e$  profiles fitted between

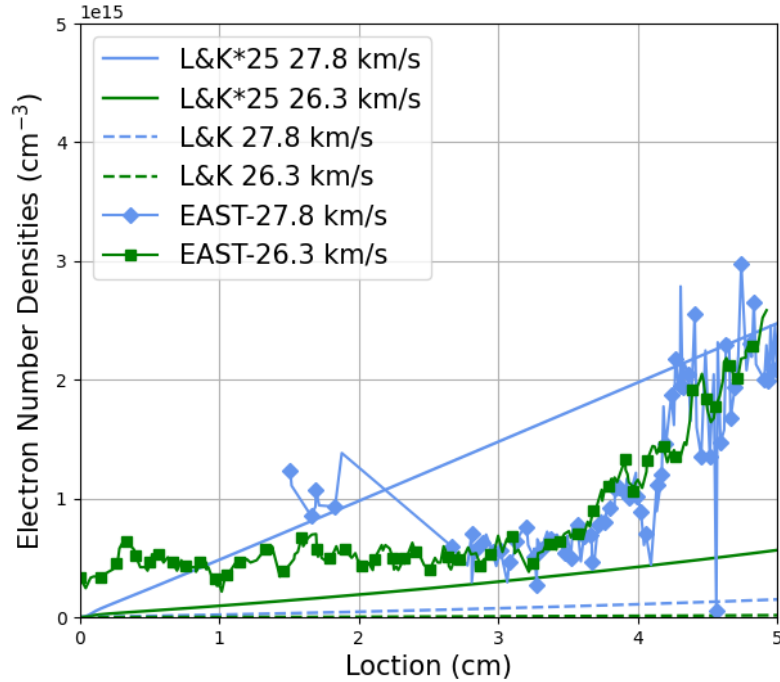


Figure 5.16: Comparison between EAST data and Eilmer simulation results in 0.2 torr conditions.

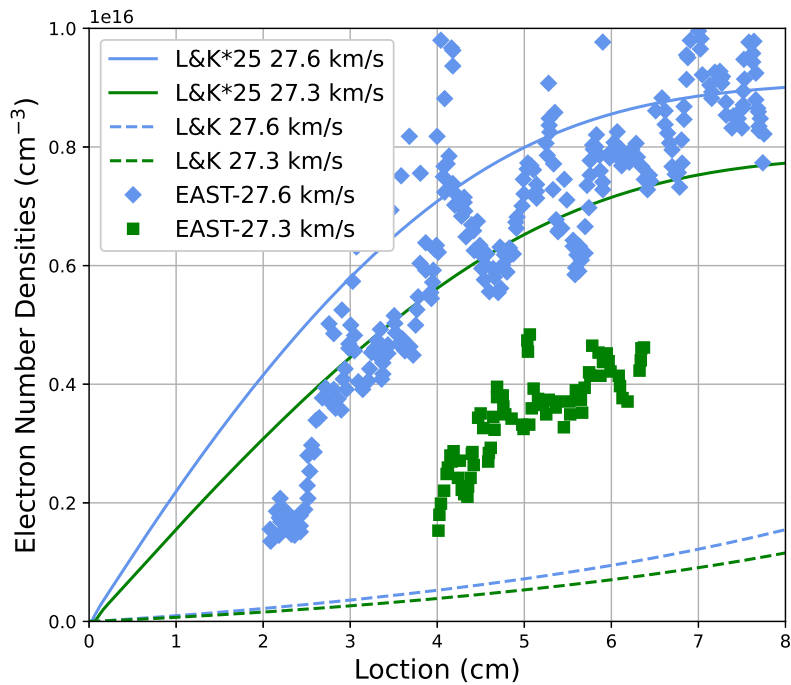


Figure 5.17: Comparison between EAST data and Eilmer simulation results in 0.5 torr conditions.

the predicted  $N_e$  profiles for these two conditions. Fig. 5.17 shows that using the updated rate set, qualitative agreement can be found in these 0.5 torr conditions and quantitative agreement can be found in the 27.6 km/s condition. In the EAST data, it was found that electronic temperature was a main driver for ionization/ $N_e$  increase, and there were delays in electronic temperature increase in EAST

data. This could be one reason for the disagreement between EAST data and numerical predictions, as a single-temperature model was used in Eilmer4. In Eilmer4, electronic temperature was assumed to be equal to frozen post-shock temperature immediately after the shock, so that the ionization delay due to the thermal non-equilibrium was not captured in 0.1 torr and 0.2 torr conditions. For 0.5 torr conditions, as the post-shock density is higher than others, the delay time is relatively shorter, so that the impact from thermal non-equilibrium will be less important. In general, the updated reaction model can simulate the EAST data with less than an order of magnitude error. Considering the error bar in a similar  $N_e$  study in EAST for lunar return [110], the numerical rebuild using the updated model is still satisfying.

## 5.4 Conclusion

Measurements of electron number density in a representative Saturn entry shock layer are reported. Electron number density was calculated using the measured Stark broadening FWHM after deconvolving the measured FWHMs from the FWHMs of the instrument function and Doppler broadening. The calculated  $N_e$  profile along the stagnation streamline was below the equilibrium limit, indicating that the shock layer did not reach an equilibrium state through the stagnation streamline. Comparing experimental results with CFD simulations using two existing reaction rates in the literature, it was found that although none of the existing reaction rates can quantitatively rebuild the ionizing shock layer, while L&K rates [15] gave a qualitative agreement on the  $N_e$  predictions. Further investigations on these rates also found that, by maintaining the L&K's dissociation rates and increasing the ionization rate coefficients by a factor of 25, quantitative agreement with experimental data was found. This updated rate set was also used to numerically simulate the  $N_e$  measurements for Saturn entry in EAST [20]. It was found that the EAST data can be simulated with less than an order of magnitude error, and quantitative agreement can be found in relatively higher density conditions. The results confirm that the kinetic model proposed by Leibowitz and Kuo [15] can be useful to describe the chemical relaxation processes. It also provides an updated and verified set of ionization rates for relevant non-equilibrium shock layer simulations.

This study has produced a unique dataset including electron number density and radiation measurements in a representative blunt body Saturn entry condition. It provides a new test case for further numerical model validation. Conducting experimental work with a broader range of giant planet entry conditions is required to provide more datasets to verify this set of updated reaction rates.



# Chapter 6

---

## Conclusion and Recommendations

---

### 6.1 Major Findings

The overall aim of this thesis was to validate a test gas substitution in the X2 expansion tube to simulate the radiating and ionizing shock layers seen during giant planet entries to gain new insights into the non-equilibrium processes involved. By using the substitution method, high molecular weight collision partners (neon or an increased fraction of helium as the diluent of hydrogen) were used in the test gas, to simulate the non-equilibrium shock layer within the performance envelope of X2. In this thesis, a series of experimental and numerical studies were presented to address the goal, with four specific objectives that were proposed in Chapter 1.

1. Generate shock layer radiation data representative of Saturn entry by using an enhanced fraction of helium in the test gas in X2.
2. Investigate the controlling factors for the chemical reaction rates in the hydrogen/inert gas mixtures.
3. Experimentally validate the test gas substitution by using H<sub>2</sub>/Ne instead of H<sub>2</sub>/He to simulate the non-equilibrium processes.
4. Obtain quantitative shock layer relaxation data to assess the suitability of the existing chemical reaction models.

These objectives were achieved and presented in this thesis. In Chapter 3, an existing test condition in X2 that could recreate the post-shock temperature in the proposed Saturn entry with an enhanced fraction of helium test gas compared to Saturn's atmosphere was tested. Radiation measurements along and perpendicular to the stagnation streamline showed that the non-equilibrium shock layer with a delayed ionization, which was also observed in Saturn entry ground testing data in EAST [20], was successfully generated. This work qualitatively validated the helium enhancement substitution method for simulation of non-equilibrium radiating flows. It was also proved that representative Saturn entry shock layers can be simulated within X2's facility performance envelope.

The existing X2 condition was used as a reference to design a condition with a H<sub>2</sub>/Ne test gas to explore whether using neon to substitute helium can recreate the non-equilibrium processes. This validation work including analysis of reaction kinetics, condition design, and experimental testing was presented in Chapter 4. Analytical analysis on dissociation and ionization was used to evaluate the similarity of the relaxation rates generated by different H<sub>2</sub>/inert gas mixtures. Factors that control the relaxation rate in these mixtures were identified as hydrogen mole fraction, post-shock temperature, and the ratio between pressure and velocity. Then, a binary scaled version of the existing H<sub>2</sub>/He condition was designed using a H<sub>2</sub>/Ne test gas with a lower velocity and a higher density. It was designed by recreating the post-shock temperature and hydrogen mole fraction, and a lower facility performance was required by using a weaker facility driver condition.

The helium-neon substitution method was validated for simulating non-equilibrium radiative shock layer by a direct comparison between spectroscopic data measured using the target H<sub>2</sub>/He condition and the designed H<sub>2</sub>/Ne condition. As the designed condition is a scaled condition with a higher density and a lower velocity compared to the target condition, a binary scaled variable  $(1-r)\frac{P_f}{V_f}$  was used for data interpretation. Using this binary scaled variable, a quantitative agreement was seen between the spatially resolved shock layer atomic hydrogen emission generated by the two conditions. In this work, the substitution theory has been validated and used in the context of radiation measurements. It also provides a data interpretation method to compensate for the scaling effect that the substitution method may create. The similarity between the proposed binary scaling variable in the various gases was also proven.

A final series of experiments were performed to obtain highly spectrally resolved H- $\beta$  spectra for broadening analysis. In Chapter 5, electron number density along the stagnation streamline in a representative Saturn entry shock layer was calculated via Stark broadening. The derived electron number density profile showed qualitative agreement with numerical predictions using L&K's reaction rate sets [21], confirming that this existing kinetic model can describe the chemical relaxation well. By maintaining the dissociation rates of L&K's rate set [21] and scaling the ionization rate coefficients by a factor of 25, a quantitative agreement was found between experimental data and numerical predictions. These adjusted rates still sit well within the variation quoted between various researchers in the literature. This work will provide a unique dataset and an updated reaction scheme for numerical study in H<sub>2</sub>/He mixtures.

## 6.2 Future Work

The work presented in this thesis successfully validated the test gas substitution method by a direct comparison of radiation measurement data in a region where the facility simulation capabilities in using H<sub>2</sub>/He and H<sub>2</sub>/Ne overlap. By using the substitution with neon, only around 8 km/s freestream velocity is required to simulate the Saturn entry shock layer. Thus, there is still large facility performance left to simulate higher speed giant planet entry conditions by using a more powerful driver condition to push the facility harder. Therefore, entry conditions such as for Neptune and Jupiter can be simulated

using this test gas substitution method in the future.

A new dataset including spectroscopic measurements, high speed imaging, and electron number density measurements was also produced, which can be used as a new test case for numerical modeling. In particular, as significant discrepancies still exist when using the current radiation modeling tool to predict H<sub>2</sub>/He radiation [21], a comparison between the radiation measurements from this thesis and numerical predictions using the latest radiation modeling code is recommended. Also, radiation measurements through the surface of the model are recommended as they can provide experimental results for the validation of computational codes used to predict incident radiative heat flux.

Although a good agreement was observed between experimental data and numerical predictions on electron number density, the agreement near the shock is still unknown. As delayed ionization is one of the important features for non-equilibrium giant planet entries, electron number density measurements in the immediate post-shock region would assist further validation of this updated reaction model. Multiple conditions with varying post-shock temperature, pressure, and gas composition are also recommended to cross-validate the updated reaction scheme provided in this thesis.

This study has validated the use of expansion tubes for the study of shock layers attached to scaled entry capsules, with particular emphasis on gas phase non-equilibrium and radiation. This is an essential step for understanding the shock layer phenomena, and the state of the gas from which the boundary layer grows. However, the eventual engineering challenge occurs when the non-equilibrium gas arrives at the surface of the heat shields, where the catalytic effects occur. With different catalytic walls, the surface may or may not promote recombination of the dissociated hydrogen when it reaches the surface. This is a large unknown for planetary entry flows and catalycity can have a large effect on heat flux as recombination is exothermic.

It was shown in Fig. 5.14 that for the shock layer generated using the H<sub>2</sub>/He condition, the level of dissociation of the gas entering the boundary layer was nearly complete, and only around 10% H atoms ionizes if the adjusted rate set was accurate. This will provide sufficient H atom for catalytic recombination. Therefore, the H<sub>2</sub>/He condition presented in this thesis would be very suitable for catalytic study.

Thermography is recommended to measure the surface heat flux in varying catalytic walls to study the catalytic effects on the heat transfer. Therefore, to have a good signal to noise ratio, the radiation from the heated wall should be sufficiently larger than shock layer radiation for more accurate surface heat flux measurements. This presents a very challenging experimental situation, with the associate ablative surface of 3000 K and the surrounding radiative shock layer.

The raw radiation data measured in this thesis were the integration along the line-of-sights parallel to the cylindrical model axis, as is shown in Fig. 5.6. The data indicate that there are significant dark optical windows in the shock layer where the shock layer radiation is very weak and its intensity can be regarded as a constant. This is due to relatively simple radiation mechanism based on the H atoms and elemental charged particles, and the low radiation from the noble gas third bodies. Some facility contamination is evident, but there can be well categorized and filtered out.

In thermography measurements, camera will measure along a line-of-sight normal to the shock

to measure the model surface radiation instead of looking from the side. To estimate the radiation in thermography measurements, the measured radiation data in Fig. 5.6 were normalized by model length and then integrated along the shock standoff. The estimated radiation is shown in Fig. 6.1. The spectrum shown in Fig. 6.1 is derived from experiments so that the impact from the tunnel impurities has already been included. However, carbon products in the heated experiments, which are not included here, can also affect the shock layer chemistry and lead to higher radiation. It was found that at around 600 nm, the shock layer radiation is less than one percent of blackbody radiation when the model surface is heated to around 2500 K. This opens the possibility of measuring surface heat flux to study catalytic effects for these flows, by use of IR thermography through carefully filtered windows in the spectra. In general, at longer wavelengths the signal (surface radiation) to noise (shock layer radiation) ratio of thermography would be even better as the blackbody radiation would be stronger. Combined with electrically preheated models with carbon based ablators, it will enable laboratory simulation of a more complete processes from bow shock to surface heat transfer, and provide very valuable dataset for numerical validation too.

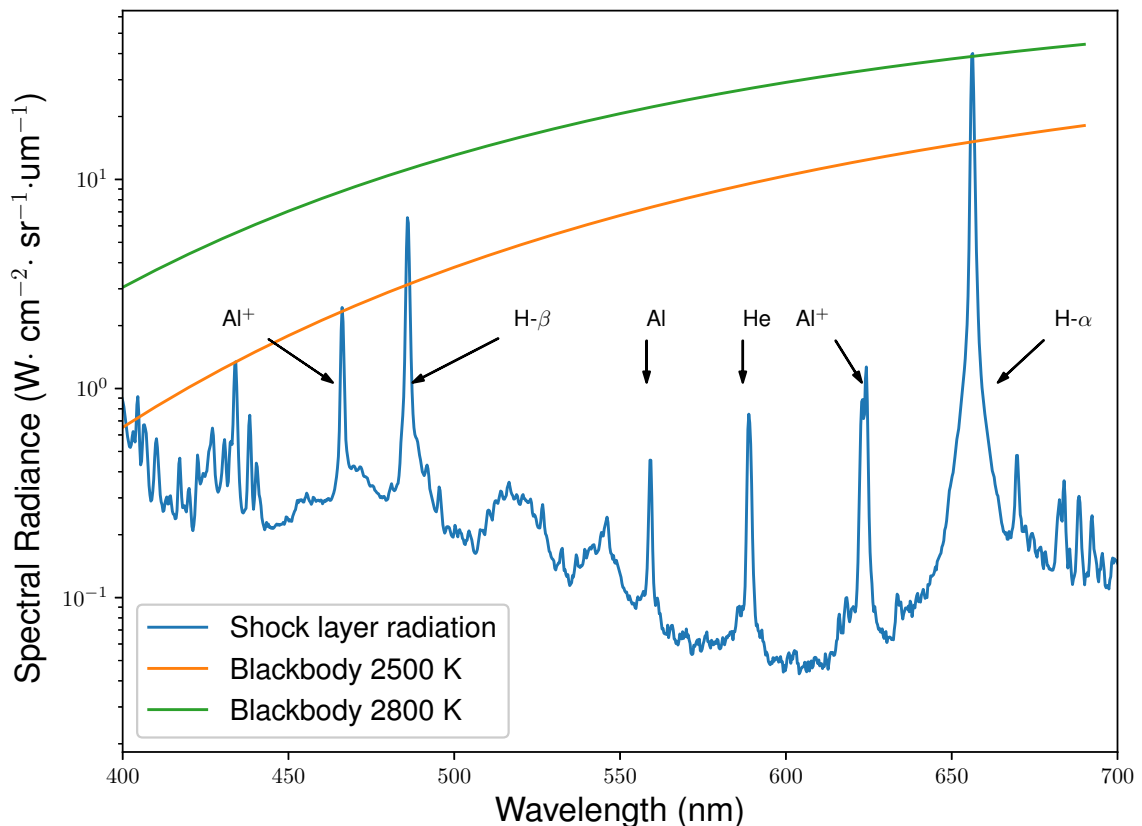


Figure 6.1: Comparison between estimated shock layer radiation viewing normal to the shock and blackbody radiation at 2500 K and 2800 K.

---

# Bibliography

---

- [1] Y. Liu, C. M. James, R. G. Morgan, and T. J. McIntyre. Using aerothermodynamic similarity to experimentally study nonequilibrium giant planet entry. *Journal of Spacecraft and Rockets*, 57(5):1008–1020, 2020.
- [2] Y. Liu, C. M. James, R. G. Morgan, and T. J. McIntyre. Experimental validation of a test gas substitution for simulating non-equilibrium giant planet entry conditions in impulse facilities. *Experiments in Fluids*, 61(9):198, 2020.
- [3] D. R. Smith, D. E. Gildfind, P. A. Jacobs, T. G. Cullen, C. M. James, Y. Liu, R. Gollan, and T. J. McIntyre. Magnetohydrodynamic drag measurements in an expansion tunnel with argon test gas. *AIAA Journal*, 0(0):1–10, 0. Article in advance.
- [4] C. M. James, S. W. Lewis, R. G. Morgan, Y. Liu, and A. Lefevre. Generating high-speed earth reentry test conditions in an expansion tube. *Journal of Spacecraft and Rockets*, 0(0):1–18, 0. Article in Advance.
- [5] Y. Liu, C. M. James, R. G. Morgan, P. A. Jacobs, R. Gollan, and T. J. McIntyre. Electron number density measurements in a saturn entry condition. In *AIAA Scitech 2021 Forum*, Virtual Event, January 2021.
- [6] Y. Liu, P. Toniato, C. James, R. Morgan, and T. J. McIntyre. Multidimensional effects and self-absorption on spectroscopic observations of saturn entry radiation. In *Asia Pacific International Symposium on Aerospace Technology*, Gold Coast, Queensland, 2019.
- [7] Y. Liu, C. M. James, R. G. Morgan, and T. J. McIntyre. Theoretical and experimental study of helium-neon substitution for Saturn entry radiation. In *AIAA Aviation 2019 Forum*, number AIAA 2019-3134, Dallas, Texas, June 2019.
- [8] Y. Liu, C. James, R. Morgan, and J. Timothy. Experimental study of saturn entry radiation with higher amount of diluent in an expansion tube. In *2018 Joint Thermophysics and Heat Transfer Conference, AIAA AVIATION Forum*, number AIAA 2018-4070, Atlanta, Georgia, June 2018.
- [9] C. M. James, Y. Liu, and R. Morgan. Simulating Uranus entry in an expansion tube. In *AIAA Aviation 2020 Forum*, number AIAA 2020-3110, VIRTUAL EVENT, June 2020.

- [10] C. M. Jamesa, S. W. Lewis, D. E. Gildfind, R. G. Morgan, T. J. McIntyre, and Y. Liu. Generating high speed earth re-entry test conditions in an expansion tube for interplanetary return missions. In *32nd International Symposium on Shock Waves*, Singapore, 1419 July 2019.
- [11] C. M. James, B. Birch, D. R. Smith, T. G. Cullen, T. Millard, S. Vella, Y. Liu, R. G. Morgan, N. Stern, and D. Buttsworth. Testing of ultra fast response, durable co-axial thermocouples for high enthalpy impulse facilities. In *AIAA Aviation 2019 Forum*, number AIAA 2019-3007, Dallas, Texas, 2019.
- [12] C. Jacobs. *Radiation in low density hypervelocity flows*. PhD thesis, the University of Queensland, Brisabane, Australia, 2011.
- [13] J. Anderson, John D. *Modern Compressible Flow: with Historical Perspective*. McGraw-Hill, New York, 3d edition, 2003.
- [14] L. P. Leibowitz. Measurements of the structure of an ionizing shock wave in a hydrogen-helium mixture. *The Physics of Fluids*, 16(1):59–68, 1973.
- [15] L. P. Leibowitz and T. J. Kuo. Ionizational nonequilibrium heating during outer planetary entries. *AIAA JOURNAL*, 14(9):1324–1329, 1976.
- [16] R. J. Stalker. Shock tunnel measurement of ionization rates in hydrogen. *AIAA Journal*, 18(4):478–480, 1980.
- [17] F. S. Milos, Y.-K. Chen, T. H. Squire, and R. A. Brewer. Analysis of Galileo probe heatshield ablation and temperature data. *Journal of Spacecraft and Rockets*, 36(3):298–306, 1999.
- [18] F. Milos. Galileo probe heat shield ablation experiment. *Journal of Spacecraft and Rockets*, 34:705–713, 1997.
- [19] S. Matsuyama, N. Ohnishi, A. Sasoh, and K. Sawada. Numerical simulation of Galileo probe entry flowfield with radiation and ablation. *Journal of Thermophysics and Heat Transfer*, 19(1):28–35, 2005.
- [20] B. A. Cruden and D. W. Bogdanoff. Shock radiation tests for Saturn and Uranus entry probes. *Journal of Spacecraft and Rockets*, 54(6 (2017)):1246–1257, 2017.
- [21] K. J. Higdon, B. A. Cruden, A. M. Brandis, D. S. Liechty, D. B. Goldstein, and P. L. Varghese. Direct simulation Monte Carlo shock simulation of Saturn entry probe conditions. *Journal of Thermophysics and Heat Transfer*, 32(3):680–690, 2018.
- [22] R. Stalker and B. Edwards. Hypersonic blunt-body flows in hydrogen-neon mixtures. *Journal of Spacecraft and Rockets*, 35:729–735, 1998.

- [23] C. M. James, D. E. Gildfind, R. G. Morgan, S. W. Lewis, and T. J. McIntyre. Simulating gas giant atmospheric entry using helium and neon test gas substitutions. *Journal of Spacecraft and Rockets*, 56(3):725–743, 2019.
- [24] C. James, D. Gildfind, S. Lewis, R. Morgan, and F. Zander. Implementation of a state-to-state analytical framework for the calculation of expansion tube flow properties. *Shock Waves*, 28(2):349–377, 2018.
- [25] G. Palmer, D. Prabhu, and B. Cruden. Aeroheating uncertainties in Uranus and Saturn entries by the Monte Carlo method. *Journal of Spacecraft and Rockets*, 51:801–814, 2014.
- [26] National Research Council. *Vision and Voyages for Planetary Science in the Decade 2013-2022*. The National Academies Press, Washington, D. C., 2012.
- [27] W. J. Borucki, D. G. Koch, G. Basri, N. Batalha, A. Boss, T. M. Brown, D. Caldwell, J. Christensen-Dalsgaard, W. D. Cochran, E. DeVore, and et al. Characteristics of kepler-planetary candidates based on the first data set. *The Astrophysical Journal*, 728(2):117, Jan 2011.
- [28] T. Sumi, D. P. Bennett, I. A. Bond, A. Udalski, V. Batista, M. Dominik, P. Fouqu, D. Kubas, A. Gould, B. Macintosh, and et al. A cold Neptune-mass planet OGLE-2007-BLG-368Lb: Cold Neptunes are common. *The Astrophysical Journal*, 710(2):16411653, Feb 2010.
- [29] N. Aeronautics and S. Administration. Juno. [https://www.nasa.gov/mission\\_pages/juno/main/index.html](https://www.nasa.gov/mission_pages/juno/main/index.html), December 2020. Accessed December 23, 2020.
- [30] K. M. Sayanagi, R. A. Dillman, D. H. Atkinson, J. Li, A. A. Saikia, S. and Simon, M. H. Spilker, T. R. and Wong, W. C. Edwards, D. Hope, A. Arora, S. C. Bowen, A. Bowes, J. S. Brady, T. O. Clark, R. E. Fairbairn, D. G. Goggin, T. A. Grondin, S. J. Horan, S. I. Infeld, J. P. Leckey, J. M. Longuski, T. E. Marvel, R. M. McCabe, A. M. Parikh, D. J. Peterson, S. J. Primeaux, A. D. Scammell, K. M. Somervill, L. W. Taylor, C. Thames, H. P. Tosoc, and L. D. Tran. Small next-generation atmospheric probe (snap) concept to enable future multi-probe missions: A case study for uranus. *Space Science Reviews*, 216(72):1–47, 2020.
- [31] H. U. The Center for Atmospheric Sciences. NASA selects Professor Sayanagi to lead Uranus probe mission concept study. <http://cas.hamptonu.edu/news/nasa-selects-professor-sayanagi-to-lead-uranus-probe-mission-concept-study/>. Accessed on Spetember 30, 2019.
- [32] R. Jits, M. Wright, and Y.-K. Chen. Closed-loop trajectory simulation for thermal protection system design for Neptune aerocapture. *Journal of Spacecraft and Rockets*, 42:1025–1034, 2005.
- [33] P. Gnoffo. Planetary-entry gas dynamics. *Annual Review of Fluid Mechanics*, 31:459–494, 1999.

- [34] J. MOSS and A. SIMMONDS. Galileo probe forebody flowfield predictions during Jupiter entry. In *3rd Joint Thermophysics, Fluids, Plasma and Heat Transfer Conference*, St. Louis, MO, U.S.A., June 1982.
- [35] C. Park. Injection-induced turbulence in stagnation-point boundary layers. *AIAA Journal*, 22(2):219–225, 1984.
- [36] C. Park. Stagnation-region heating environment of the Galileo probe. *Journal of Thermophysics and Heat Transfer*, 23(3):417–424, 2009.
- [37] L. Santos Fernandes, B. Lopez, and M. Lino da Silva. Computational fluid radiative dynamics of the Galileo Jupiter entry. *Physics of Fluids*, 31(10):106104, 2019.
- [38] A. J. Erb, T. K. West, and C. O. Johnston. Investigation of galileo probe entry heating with coupled radiation and ablation. *Journal of Spacecraft and Rockets*, 57(4):692–706, 2020.
- [39] I. D. Boyd. Monte Carlo simulation of nonequilibrium flow in a low-power hydrogen arcjet. *Physics of Fluids*, 9(10):3086–3095, 1997.
- [40] C. Park. Nonequilibrium ionization and radiation in hydrogen-helium mixtures. *Journal of Thermophysics and Heat Transfer*, 26:231–243, 2012.
- [41] G. Colonna, L. D. Pietanza, and A. Laricchiuta. Ionization kinetic model for hydrogen-helium atmospheres in hypersonic shock tubes. *International Journal of Heat and Mass Transfer*, 156:119916, 2020.
- [42] D. Gildfind, R. G. Morgan, and P. Jacobs. Expansion tubes in australia. In O. Igra and F. Seiler, editors, *Experimental Methods of Shock Wave Research*, pages 399–431. Springer, Cham, 2016.
- [43] G. R. Inger, C. Higgins, and R. Morgan. Shock standoff on hypersonic blunt bodies in nonequilibrium gas flows. *Journal of Thermophysics and Heat Transfer*, 16(2):245–250, 2002.
- [44] G. R. Inger, C. Higgins, and R. Morgan. Generalized nonequilibrium binary scaling for shock standoff on hypersonic blunt bodies. *Journal of Thermophysics and Heat Transfer*, 17(1):126–128, 2003.
- [45] C. Higgins. *Aerothermodynamics of the Gas Giants*. PhD thesis, The University of Queensland, Brisbane, Australia, 2004.
- [46] C. O. Laux. *Optical Diagnostics and Radiative Emission of Air Plasmas*. PhD thesis, STANFORD UNIVERSITY., Jan. 1993.
- [47] M. N. S. D.Sc. Liii. ionization in the solar chromosphere. *The London, Edinburgh, and Dublin Philosophical Magazine and Journal of Science*, 40(238):472–488, 1920.
- [48] S. M. N. On a physical theory of stellar spectra. *Proc. R. Soc.*, 99(697):135–153, May 1921.

- [49] B. A. Cruden and D. W. Bogdanoff. Shock radiation tests for saturn and uranus entry probes. In *45th AIAA Thermophysics Conference*, Dallas, TX, USA, June 2015.
- [50] M. J. Lighthill. Dynamics of a dissociating gas part i equilibrium flow. *Journal of Fluid Mechanics*, 2(1):132, 1957.
- [51] M. J. Lighthill. Dynamics of a dissociating gas part 2. quasi-equilibrium transfer theory. *Journal of Fluid Mechanics*, 8(2):161182, 1960.
- [52] N. C. Freeman. Non-equilibrium flow of an ideal dissociating gas. *Journal of Fluid Mechanics*, 4(4):407425, 1958.
- [53] I. I. Glass and W. S. Liu. Effects of hydrogen impurities on shock structure and stability in ionizing monatomic gases. part 1. Argon. *Journal of Fluid Mechanics*, 84(1):5577, 1978.
- [54] M. I. Hoffert and H. Lien. Quasidimensional, nonequilibrium gas dynamics of partially ionized twotemperature argon. *The Physics of Fluids*, 10(8):1769–1777, 1967.
- [55] D. Bogdanoff and C. Park. Radiative interaction between driver and driven gases in an arc-driven shock tube. *Shock Waves*, 12:205–214, 2002.
- [56] F. R. Livingston and P. T. Y. Poon. Relaxation distance and equilibrium electron density measurements in hydrogen-helium plasmas. *AIAA Journal*, 14(9):1335–1337, 1976.
- [57] S. N. Tiwari and K. Y. Szema. *Effects of Precursor Heating on Chemical and Radiative Nonequilibrium Viscous Flow around a Jovian Entry Body*. Contractor Report 3186, 1979.
- [58] S. N. Tiwari and K. Y. Szema. *Influence of Nonequilibrium Radiation and Shape Change on Aerothermal Environment of a Jovian Entry Body*. Contractor Report 3432, 1981.
- [59] R. N. Talley. *Galileo Probe Deceleration Module Final Report*. Re-Entry Systems Operations. General Electric Co., Rept. 84SDS2020, Jan 1984.
- [60] A. Kumar and R. A. Graeves. *User's guide for the computer code COLTS for calculating the coupled laminar and turbulent flow over a Jovian entry probe*. NASA STI/Recon Technical Report N, June 1980.
- [61] R. BREWER, D. BRANT, and R. FOGAROLI. Development of a steady-state shape change ablation code for the design of outer planet probes. In *15th Aerospace Sciences Meeting*, Los Angeles, CA, U.S.A., January 1977.
- [62] M. Furudate, I.-S. Jeung, and S. Matsuyama. *Nonequilibrium Calculation of Flowfield over Galileo Probe*.
- [63] C. Park and M. Tauber. Heatshielding problems of planetary entry - a review. In *30th Fluid Dynamics Conference*, 1999.

- [64] U. v. Zahn and D. M. Hunten. The helium mass fraction in Jupiter's atmosphere. *Science*, 272(5263):849–851, 1996.
- [65] H. B. Niemann, S. K. Atreya, G. R. Carignan, T. M. Donahue, J. A. Haberman, D. N. Harpold, R. E. Hartle, D. M. Hunten, W. T. Kasprzak, P. R. Mahaffy, T. C. Owen, N. W. Spencer, and S. H. Way. The Galileo probe mass spectrometer: Composition of Jupiter's atmosphere. *Science*, 272(5263):846–849, 1996.
- [66] B. BALDWIN and H. LOMAX. *Thin-layer approximation and algebraic model for separated turbulent flows*.
- [67] C. Park. Effect of lyman radiation on nonequilibrium ionization of atomic hydrogen. In *37th AIAA Thermophysics Conference*, number AIAA 2004-2277, Portland, Oregon, 2004.
- [68] M. Furudate. Nonequilibrium calculation of high-temperature radiating h<sub>2</sub>-he flowfield. *Journal of Thermophysics and Heat Transfer*, 23(4):651–659, 2009.
- [69] D. Bogdanoff and C. Park. Radiative interaction between driver and driven gases in an arc-driven shock tube. *Shock Waves*, 12:205214, 2002.
- [70] B. A. Cruden and A. M. Brandis. Updates to the NEQAIR radiation solver. In *6th International Workshop on Radiation of High Temperature Gases in Atmospheric Entry*, St Andrews, Scotland, United Kingdom, 2014.
- [71] S. R.J. Similarity transformation for blunt body flows. In *AIAA 24th Aerospace Sciences Meeting.*, 0146-3705, Reno, NV, USA, 1986.
- [72] P. Subrahmanyam. High-fidelity aerothermal engineering analysis for planetary probes using DOTNET framework and OLAP cubes database. *International Journal of Aerospace Engineering*, 2009(326102):21–41, 2009.
- [73] S. W. Lewis, C. James, R. G. Morgan, T. J. McIntyre, C. R. Alba, and R. G. Greendyke. Carbon ablative shock-layer radiation with high surface temperatures. *Journal of Thermophysics and Heat Transfer*, 31(1):193–204, 2017.
- [74] R. Ravichandran, D. R. Buttsworth, S. W. Lewis, R. G. Morgan, and T. J. McIntyre. Filtered image thermography for high temperatures in hypersonic preheated ablation experiments. *Journal of Thermophysics and Heat Transfer*, 33(4):1074–1084, 2019.
- [75] B. R. Capra and R. G. Morgan. Total heat transfer measurements on a flight investigation of reentry environment model. *Journal of Spacecraft and Rockets*, 50(3):494–503, 2013.
- [76] D. Gildfind, C. James, P. Toniato, and R. Morgan. Performance considerations for expansion tube operation with a shock-heated secondary driver. *Journal of Fluid Mechanics*, 777:364–407, 2015.

- [77] D. Gildfind, R. Morgan, M. McGilvray, P. Jacobs, R. Stalker, and T. Eichmann. Free-piston driver optimisation for simulation of high mach number scramjet flow conditions. *Shock Waves*, 21(6):559–572, 2011.
- [78] J. Canny. A computational approach to edge detection. *IEEE Transactions on pattern analysis and machine intelligence*, PAMI-8(6):679–698, Nov 1986.
- [79] C. James, T. Cullen, H. Wei, S. Lewis, S. Gu, R. Morgan, and T. McIntyre. Improved test time evaluation in an expansion tube. *Experiments in Fluids*, 59(87), 2018.
- [80] P. Jacobs and R. Gollan. Implementation of a compressible-flow simulation code in the D programming language. In *Advances of Computational Mechanics in Australia*, volume 846 of *Applied Mechanics and Materials*, pages 54–60. Trans Tech Publications Ltd, 9 2016.
- [81] R. Gollan and P. Jacobs. About the formulation, verification and validation of the hypersonic flow solver Eilmer. *International Journal for Numerical Methods in Fluids*, 73(1):19–57, 2013.
- [82] G. de Crombrugghe, R. Morgan, and O. Chazot. Theoretical approach and experimental verification of the role of diffusive transport under binary scaling conditions. *International Journal of Heat and Mass Transfer*, 97:675 – 682, 2016.
- [83] C. M. James, D. R. Smith, C. McLean, R. G. Morgan, S. W. Lewis, and P. Toniato. Improving high enthalpy expansion tube condition characterisation using high speed imagery. In *2018 Aerodynamic Measurement Technology and Ground Testing Conference*, Atlanta, Georgia, June 2018.
- [84] S. W. Lewis, R. G. Morgan, T. J. McIntyre, C. R. Alba, and R. G. Greendyke. Expansion tunnel experiments of Earth reentry flow with surface ablation. *Journal of Thermophysics and Heat Transfer*, 31(1):193–204, 2017.
- [85] Y. Takama and K. Suzuki. Spectroscopic observation of translational-rotational nonequilibrium in low-density hydrogen plasma flow. *Journal of Thermophysics and Heat Transfer*, 23:454–462, 2009.
- [86] R. M. Kelly. *Spectral Analysis of Atomic Argon Radiation in an Expanding Hypersonic Flow*. PhD thesis, the University of Queensland, Brisabane, Australia, 2020.
- [87] J. S. Jewell, N. J. Parziale, I. A. Leyva, and J. E. Shepherd. Effects of shock-tube cleanliness on hypersonic boundary layer transition at high enthalpy. *AIAA Journal*, 55(1):332–338, 2017.
- [88] P. Georg. A new method for numerical Abel-inversion. *Zeitschrift fr Naturforschung A*, 1991.
- [89] E. S. Agency. Cassini-Huygens. <http://sci.esa.int/cassini-huygens/33006-engineering/?fbbodylongid=1151>, October 2005. Accessed May 11, 2019.

- [90] C. James. *Radiation from Simulated Atmospheric Entry into the Gas Giants*. PhD thesis, the University of Queensland, Brisabane, Australia, 2017.
- [91] B. McBride and G. Gordon. *Computer Program for Calculation of Complex Chemical Equilibrium Compositions and Applications II. Users Manual and Program Description*. NASA Lewis Research Center, Cleveland, OH, U.S.A., 1996.
- [92] G. Gordon and B. McBride. *Computer Program for Calculation of Complex Chemical Equilibrium Compositions and Applications I. Analysis*. NASA Lewis Research Center, Cleveland, OH, U.S.A., 1994.
- [93] F. Zander, R. J. Gollan, and R. G. Morgan. Hypervelocity shock standoff on spheres in air. *Shock Waves*, 24:171178, 2014.
- [94] P. Reynier, G. D'Ammando, and D. Bruno. Review: Modelling chemical kinetics and convective heating in giant planet entries. *Progress in Aerospace Sciences*, 96:1 – 22, 2018.
- [95] J. A. Manion, R. E. Huie, R. D. Levin, D. R. B. Jr., V. L. Orkin, W. Tsang, W. S. McGivern, J. W. Hudgens, V. D. Knyazev, D. B. Atkinson, E. Chai, A. M. Tereza, C.-Y. Lin, T. C. Allison, W. G. Mallard, F. Westley, J. T. Herron, R. F. Hampson, and D. H. Frizzell. Nist chemical kinetics database, nist standard reference database 17, version 7.0 (web version), release 1.6.8, 2015.09. 20899-8320.
- [96] T. D. McCay and C. E. Dexter. Chemical kinetic performance losses for a hydrogen laser thermal thruster. *Journal of Spacecraft and Rockets*, 24(4):372–376, 1987.
- [97] C. Park, R. L. Jaffe, and H. Partridge. Chemical-kinetic parameters of hyperbolic earth entry. *Journal of Thermophysics and Heat Transfer*, 15(1):76–90, 2001.
- [98] J. G. Kim, O. J. Kwon, and C. Park. Master equation study and nonequilibrium chemical reactions for h + h<sub>2</sub> and he + h<sub>2</sub>. *Journal of Thermophysics and Heat Transfer*, 23(3):443–453, 2009.
- [99] J. G. Kim, O. J. Kwon, and C. Park. Master equation study and nonequilibrium chemical reactions for hydrogen molecule. *Journal of Thermophysics and Heat Transfer*, 24(2):281–290, 2010.
- [100] J. McBride, S. Heimel, J. G. Ehlert, and S. Gordon. *Thermodynamic Properties to 6000 K for 210 Substances Involving the First 18 Elements*. NASA SP-3001, Washington, 1963.
- [101] T. N. Eichmann, T. J. McIntyre, A. I. Bishop, S. Vakata, and H. Rubinsztein-Dunlop. Three-dimensional effects on line-of-sight visualization measurements of supersonic and hypersonic flow over cylinders. *Shock Waves*, 16(4):299–307, 2007.
- [102] U. A. Sheikh, R. G. Morgan, and T. J. McIntyre. Optical thickness measurements of vacuum ultraviolet radiation in the X2 expansion tube. *AIAA Journal*, 54(8):11. 2407–2417, 2016.

- [103] A. P. Thorne. *Spectrophysics*. Springer Netherlands, Dordrecht, 2.. edition, 1988.
- [104] H. Griem. *Plasma spectroscopy*. 1964.
- [105] N. Konjevi, M. Ivkovi, and N. Sakan. Hydrogen balmer lines for low electron number density plasma diagnostics. *Spectrochimica Acta Part B: Atomic Spectroscopy*, 76:16 – 26, 2012. Honoring Issue: A Collection of Papers on Plasma and Laser Spectrochemistry. Dedicated to Gary M. Hieftje on the occasion of his 70th birthday.
- [106] J. Touma, E. Oks, S. Alexiou, and A. Derevianko. Review of the advanced generalized theory for stark broadening of hydrogen lines in plasmas with tables. *Journal of Quantitative Spectroscopy and Radiative Transfer*, 65(1):543 – 571, 2000.
- [107] J. Olivero and R. Longbothum. Empirical fits to the voigt line width: A brief review. *Journal of Quantitative Spectroscopy and Radiative Transfer*, 17(2):233 – 236, 1977.
- [108] R. J. Moffat. Describing the uncertainties in experimental results. *Experimental Thermal and Fluid Science*, 1(1):3 – 17, 1988.
- [109] K. Hansson, A. T. Carroll, S. J. Poovathingal, and I. D. Boyd. Analysis of chemical kinetic parameters for hydrogen atmospheres. In *AIAA Scitech 2021 Forum*, VIRTUAL EVENT, January 2021.
- [110] B. A. Cruden. Electron density measurement in reentry shocks for lunar return. *Journal of Thermophysics and Heat Transfer*, 26(2):222–230, 2012.



# Appendix A

---

## Modifications to Reproduced Publications

---

### A.1 Chapter3: Using Aerothermodynamic Similarity to Experimentally Study Non-equilibrium Gas Giant Entry

*Changes made for formatting consistency with main thesis document:*

- General formatting such as fonts, font sizes, and changing to single column.
- Chapter number added to table, figure, and equation numbering.
- Nomenclature and symbols from journal paper has been merged with that of the main document.

*Minor corrections to as-published content during inclusion into thesis:*

- Appendix of the original paper has been merged into this chapter as Section 3.5.1.
- Reference of the driver condition was added in Table 3.1.
- The sentence “The PITOT prediction was performed in a fully theoretical mode where shock speeds are found from fill pressures.” has been added.
- The sentence “Detailed information of this scaling method will be published in the further work.” has been changed as “Detailed information of this scaling method will be discussed in Chapter 4.”
- The sentence “Spectroscopic results from five experiments with the test model are presented in this section and the appendix.” has been changes as “Spectroscopic results from five experiments with the test model are presented in this section and the appendix.”
- Figure 3.6 has been changed to the version with path lengths.
- Figure 3.7 has been revised as suggested to show the physical scale.

- Comments on the flow exiting the nozzle has been added: “It can be seen that the nozzle exit pressure (freestream flow pressure) is around 100 times higher than the ambient pressure (acceleration tube fill pressure), so that the nozzle flow was under-expanded.”
- The discussion of Al<sup>+</sup> line analysis has been revised. The Al<sup>+</sup> line chosen for analysis has an excitation energy of 15 eV, so is higher than the Hydrogen ionization energy. Thus the assumed relationship between the appearance of the Al+ line and hydrogen in the published paper may not be valid. The ionization energy of Al is lower than the excitation energy of H- $\alpha$ , such that its ionization will begin before any radiation is observed.
- The estimation of the concentration of Aluminium has been added in Chapter 3.4.3.
- The discussion of self-absorption has been added in Chapter 3.5
- The definition of shock front has been added in Chapter 4.4.3

## A.2 Chapter4: Experimental Validation of a Test Gas Substitution for Simulating Scaled Giant Planet Entry Conditions in Impulse Facilities

*Changes made for formatting consistency with main thesis document:*

- General formatting such as fonts, font sizes, and changing to single column.
- Chapter number added to table, figure, and equation numbering.
- Nomenclature and symbols from journal paper has been merged with that of the main document.

*Minor corrections to as-published content during inclusion into thesis:*

- The sentence “PITOT prediction was run in a partially theoretical mode where experimentally measured shock tube shock speed and fill pressures were used to predict the freestream flow properties.” has been added.
- The sentence “The post-shock state for a frozen normal shock, as well as the fully dissociated state and equilibrium state flow properties calculated by NASA’s CEA (Chemical Equilibrium with Applications) program [91,92] are listed in Table 4.1.” has been revised as “The post-shock frozen state was obtained from the numerical prediction using the in-house code Poshax3 [80,81], which predicts the post-shock flow properties in inviscid and one-dimensional flow assuming no body. The fully dissociated state and equilibrium state flow properties were calculated by NASA’s Chemical Equilibrium with Applications (CEA) program [91,92]. These results are listed in Table 4.1.”

- The sentence “The post-shock flow relaxation generated by the helium condition, neon condition, and the trajectory point  $t = 206$  s [25] were numerically calculated by the in-house code Poshax3 [80,81], which predicts the post-shock flow properties in inviscid and one-dimensional flow assuming no body.” has been revised as “The post-shock flow relaxation generated by the helium condition, neon condition, and the trajectory point  $t = 206$  s [25] were numerically calculated by Poshax3.”
- The sentence “It should be noted that as the PITOT prediction of the freestream properties prediction for this target condition in the previous chapter was using the fully theoretical mode, there is a slight difference for the calculated flow properties between Table 3.2 and Table 4.1.” has been added.
- the sentence “The reverse reaction rate is negligible as the density is generally low, and little recombination is seen.” has been revised as “The reverse reaction rate is negligible in the highly non-equilibrium region especially in the immediate post-shock region. This is because the density of the giant planet entry conditions is generally low, and little recombination is seen.”
- The discussion of the binary scaling limitation has been added in Chapter 4.2



## Appendix B

---

# Characterisation Experiments for the H<sub>2</sub>/Ne Condition

---

In Chapter 4, the designed condition with H<sub>2</sub>/Ne test gas is shown to be able to recreate the non-equilibrium process generated by the target H<sub>2</sub>/He condition. The results of the condition characterisation experiments for the H<sub>2</sub>/He condition has been presented in Section 3.3. In this Appendix, the details of the H<sub>2</sub>/Ne condition design procedure will be demonstrated.

## B.1 Condition Design Requirements

As has been discussed in Section 4.2, to recreate the relaxation rate along the binary scaling variable  $\chi$ , hydrogen mole fraction  $r$  and post-shock frozen temperature  $T_f$  of the target H<sub>2</sub>/He condition are required to be duplicated in the designed H<sub>2</sub>/Ne condition. Hence, the test gas for the H<sub>2</sub>/Ne condition is set to be 20%H<sub>2</sub>/80%Ne to satisfy the hydrogen mole fraction requirement. The main requirement for the H<sub>2</sub>/Ne condition is to recreate the  $T_f$  in the H<sub>2</sub>/He condition, which can be found in Table 3.2 to be around 25600 K.

X2 expansion tube performance can be controlled by the driver condition, fill pressure of shock tube and acceleration tube, and the test gas. The facility modelling can be performed using PITOT, which is a UQ's in-house expansion tube and shock tunnel simulation code based on isentropic and compressible flow state-to-state gas processes. PITOT can predict the freestream flow properties and post-shock flow properties based on the chosen driver condition, fill pressure, and test gas using the fully theoretical mode. However, it is very difficult to predict all the complex flow processes during expansion tube operation, such as the heat and pressure loss in the driver compression, wall friction and heat lose when the flow travels through the acceleration tube, the boundary layer growth in the nozzle etc. To reduce the error for the PITOT prediction, experimental calibration is required before using PITOT to predict the generated flow condition. Adjustable variables such as loss factor and area ratio are introduced and used in the experimental calibration to obtain a better prediction of the facility performance.

The detail of how PITOT works and how to perform experimental calibration can be found in the work of James et al. [24]. The condition design procedure was demonstrated using a flowchart shown in Fig. B.1. In the H<sub>2</sub>/Ne condition design, fully theoretical PITOT calculation was performed to find an appropriate condition that can recreate the target T<sub>f</sub>. Then, experimental calibration was conducted based on experimentally measured shock tube shock speed (V<sub>s1</sub>), acceleration tube shock speed (V<sub>s2</sub>), and pitot pressure. If the calibrated T<sub>f</sub> does not match the target value, fill pressure of acceleration tube would be adjusted and the generated flow condition would be simulated using the calibrated PITOT setting until the T<sub>f</sub> can be theoretically recreated. Experimental tests with the updated fill pressure would then be performed and the experimental calibration would be conducted again until the calibrated T<sub>f</sub> matched the target value.

## B.2 Experimental Set-up

Before conducting spectral measurements for the shock layer generated with a test model. The characteristics of the generated freestream condition, such as how big the core flow is and when the test gas established on the test model after the data acquisition system is triggered by the arrival of the acceleration tube gas, need to be understood. This is because the design of the test model requires the model to fit within the core flow where the viscous effect can be neglected and the flow properties can be treated as evenly distributed. Additionally, the optical system needs to be set to expose within the test time when the flow has established.

To obtain these information, a rake mounted with nine pitot probes was set-up in the test section, as is shown in Fig. B.2. Also, Fig. B.3 shows the scale of the rake with the nozzle and its axial location. The interval of each two adjacent probes was 17.5 mm. In the experiments, each probe will record time-resolved pressure which represents the pressure development at its radial location.

In addition, a high speed camera filtered by a bandpass filter with a centre wavelength of 656.3 nm and a bandwidth of 10 nm was set-up on one side of the test section. The filtered camera was to capture the time-resolved H- $\alpha$  emission around the probes. The intensity of the recorded emission around each probe was then integrated within a chosen box as shown in Fig. B.4.

## B.3 Results

### B.3.1 Time-resolved Pressure and Emission Measurements

The results of the time-resolved pressure measured by pitot probes and the filtered integrated intensity around each probe measured by high speed camera are shown in Fig. B.5. It can be seen that after the pressure and intensity increase due to the acceleration tube flow arrival, it took around 50  $\mu$ s for the steady shock layer to establish, which led to the pressure and intensity drop until they reached relatively steady levels. Then, the pressure profiles kept approximately constant till 160  $\mu$ s when the unsteady expansion arrived and caused the pressure to rise. The integrated intensity profiles showed a

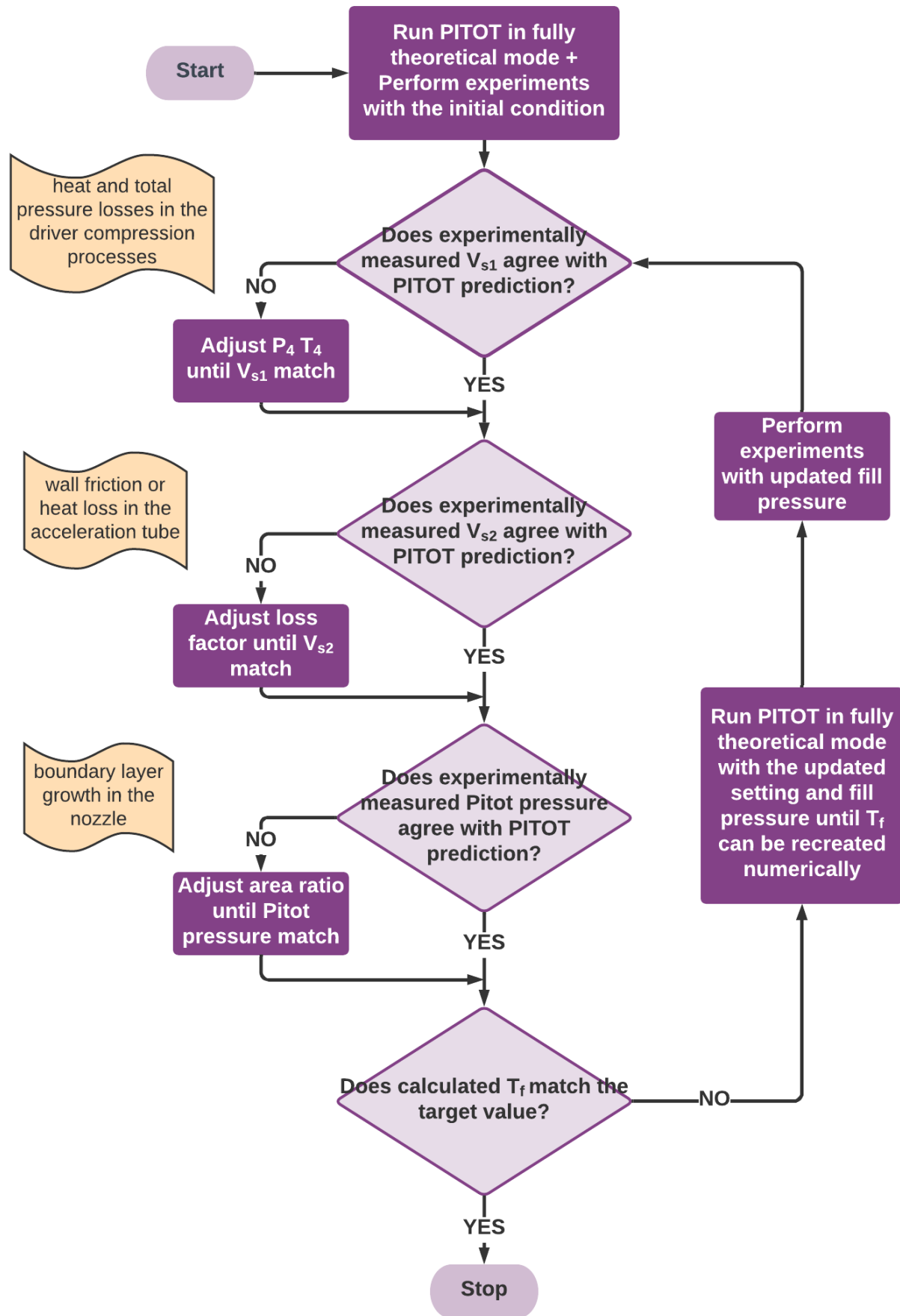


Figure B.1: Flowchart of the neon condition design procedure.

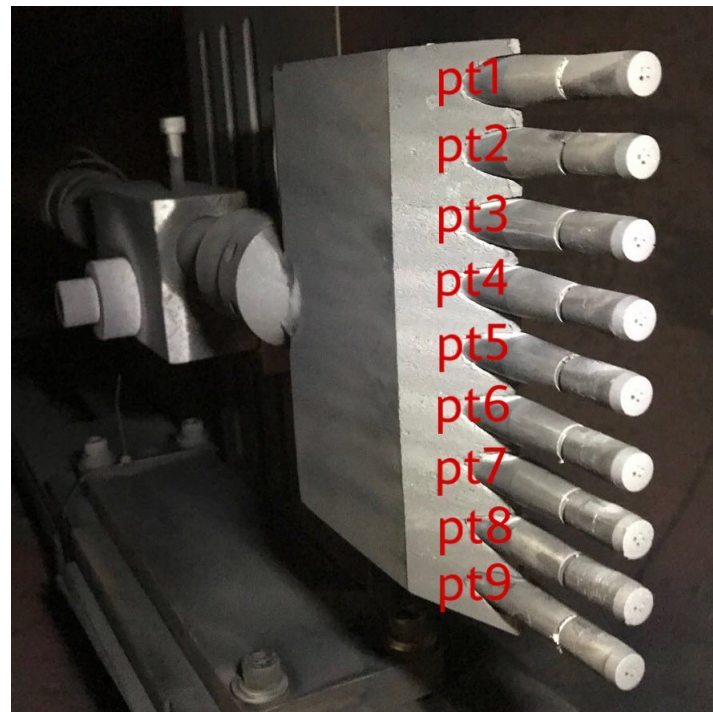


Figure B.2: Set-up of pitot probes on the rake

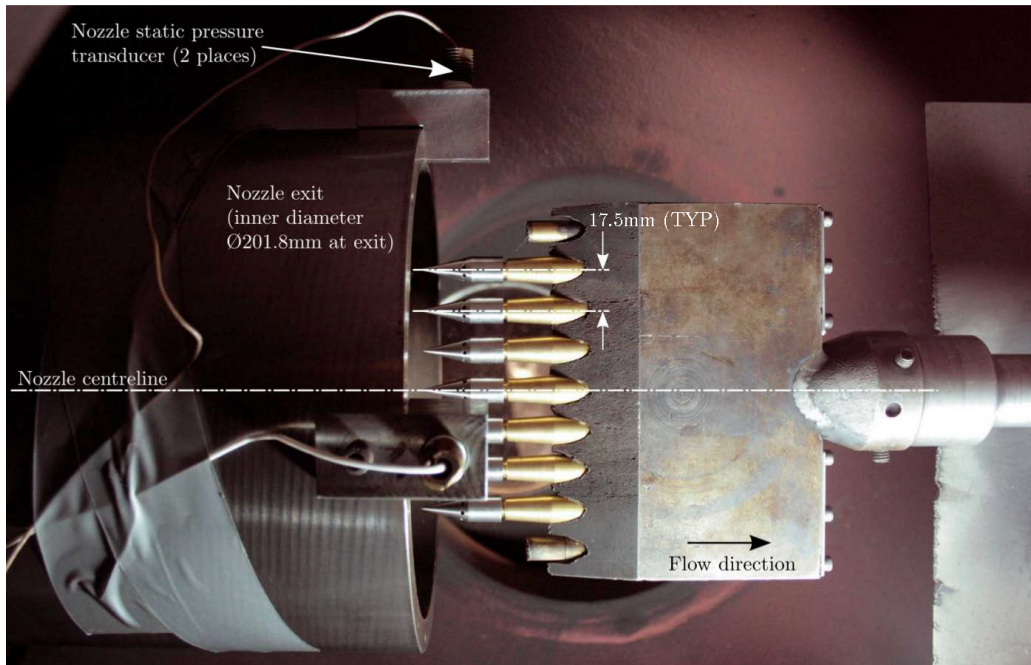


Figure B.3: Scale of the rake with the nozzle and its axial location.

steady time period from 50  $\mu$ s to 90  $\mu$ s. Combining the pressure and intensity results, the estimated test time for this condition was from 50  $\mu$ s to 90  $\mu$ s. In the experiments with a test model, as the model size is usually larger than a pitot probe, it can take more time for the steady flow to establish. Therefore, in the experiments with a test model, the spectroscopic system was set to be exposed between 70  $\mu$ s and 90  $\mu$ s .

It can also been found that while the pressure measured by all nine probes agreed well within the test time, the integrated intensity profiles around the four probe on the edge (pt1, pt2, pt8, and pt9) had

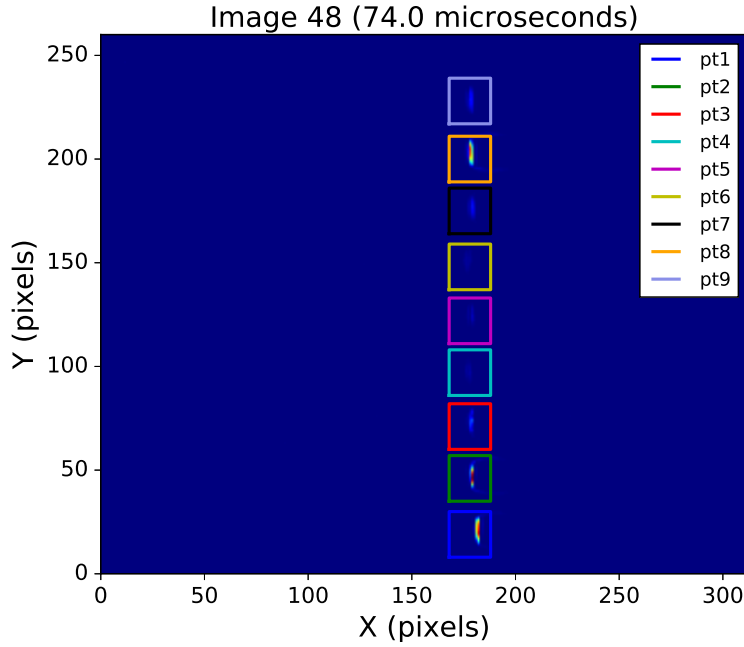


Figure B.4: H- $\alpha$  filtered radiation from shock layer over pitot probes and the area for intensity integration, with pt5 aligned with the nozzle centreline.

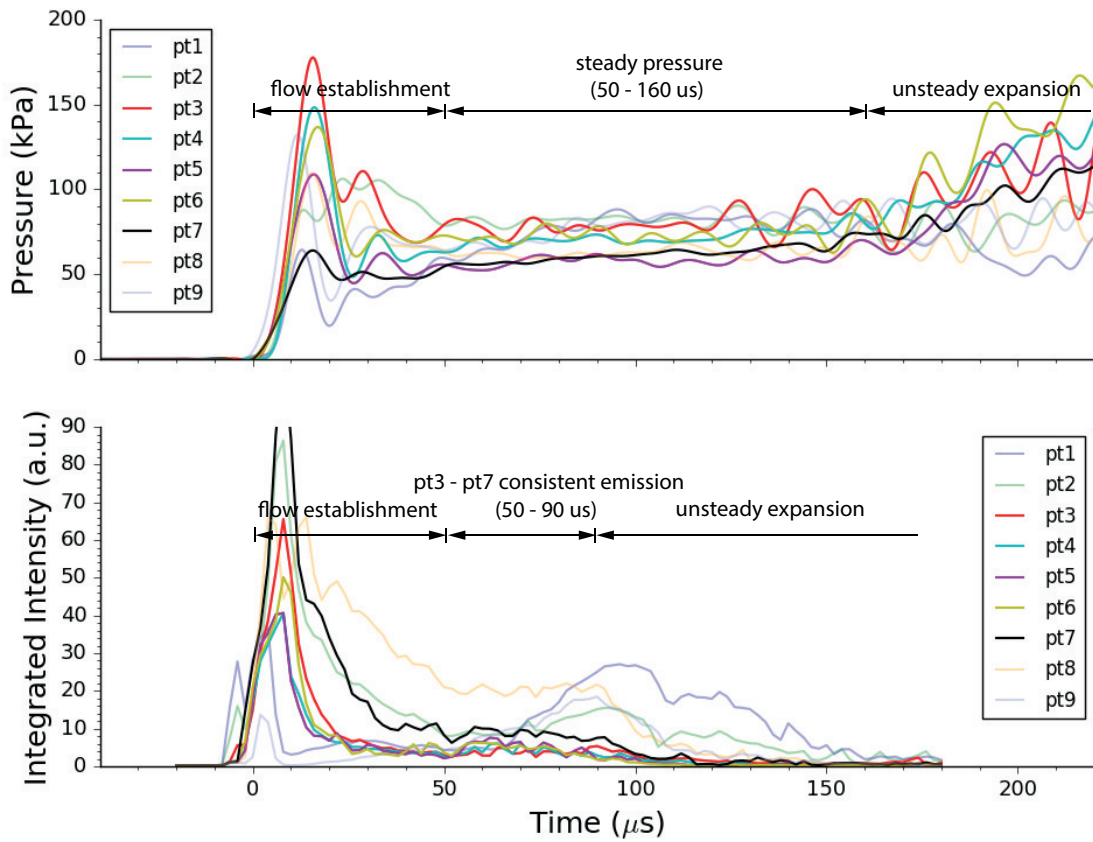


Figure B.5: Time-resolved pitot pressure and integrated emission over each pitot probe.

significant discrepancy with others. This indicated these four probes were not within the core flow. Hence, the core flow was identified as the circular region within pt3 and pt7 within the diameter of

87.5 mm.

### B.3.2 Condition Detail

After looping the procedure shown in Fig. B.1, the ultimate condition, after being experimentally calibrated, was able to approximately recreate the target  $T_f$ . The detail of the designed condition is shown in Table B.1. Readers are encouraged to read work of Gildfind et al. [77] for more detail of the driver condition.

Table B.1: Details of the designed H<sub>2</sub>/Ne condition.

Driver condition designation	X2-LWP-1.2 mm-0 [77]
Primary driver fill condition	110.3 kPa 100% helium
Primary diaphragm	1 x 1.2 mm thick cold rolled steel, scored diaphragm
Rupture pressure	15.5 MPa
Shock tube fill condition	2.0 kPa 80%/20% (by volume) hydrogen/neon
Secondary diaphragm	1 x $\approx$ 14 $\mu$ m thick aluminum foil diaphragm
Acceleration tube fill condition	13.5 Pa air

During the experimental calibration of this condition, primary driver burst pressure ( $P_4$ ) and temperature ( $T_4$ ) were set as 14 MPa and 1100 K respectively to obtain a good prediction of  $V_{s1}$ . Also, the loss factor was adjusted as 0.83 to account for the friction and heat lose in the acceleration tube and match the  $V_{s2}$ , while area ratio was adjusted as 4.5 to compensate for the boundary growth in the nozzle and correctly predict the Pitot pressure. The PITOT predictions of  $V_{s1}$ ,  $V_{s2}$ , and Pitot pressure are compared with the experimental measurements are shown in Table B.2.

Table B.2: Comparison between PITOT prediction and experimental measurements.

-	PITOT	Experimental measurements
Shock tube shock speed, m/s	4980	$4970 \pm 40$ (measured among sd1-sd3)
Acceleration tube shock speed, m/s	8270	$8320 \pm 50$ (measured among at4-at8)
Pitot pressure, kPa	68	$70 \pm 6$ (averaged among st3-st7)

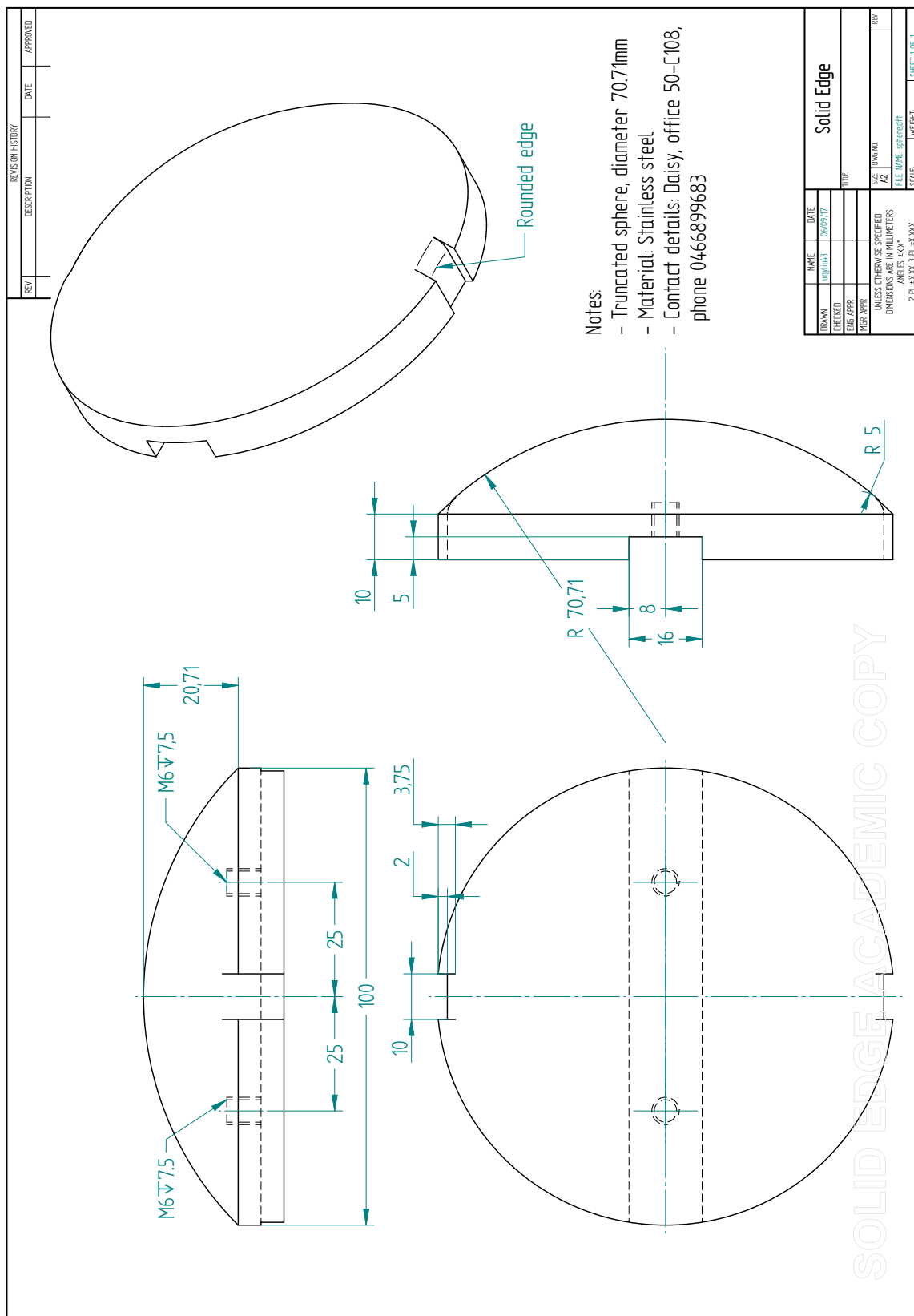
## **Appendix C**

---

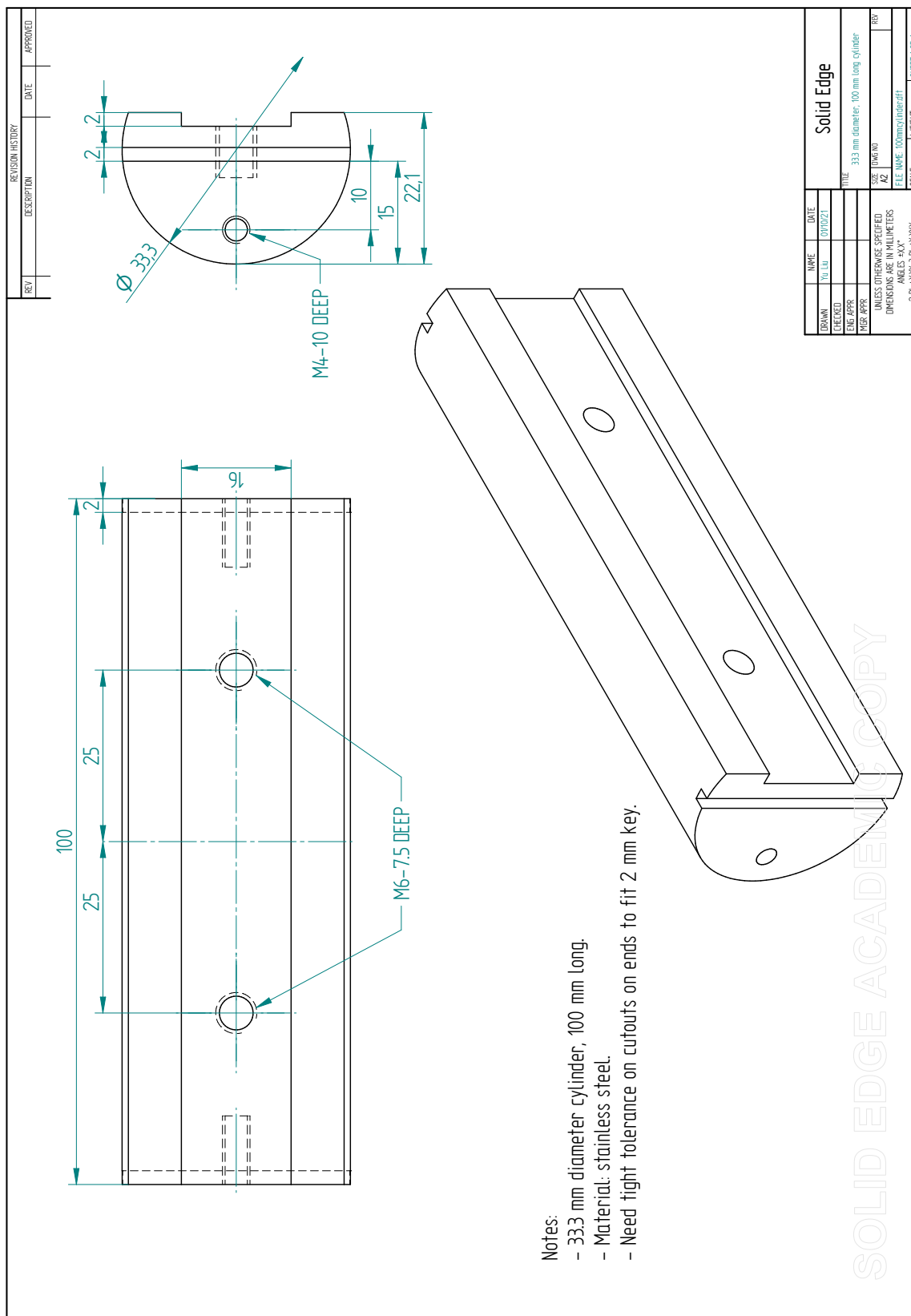
### **Technical Drawings for Test Models and Alignment Tools**

---

## C.1 Spherical Test Model



## C.2 Cylindrical Test Model: 33.3 diameter, 100 mm long



### C.3 Alignment Tool for Cylindrical Test Models

